THÈSE

En vue de l'obtention du

DOCTORAT DE L'UNIVERSITÉ DE TOULOUSE

Délivré par : *Université Toulouse 3 Paul Sabatier (UT3 Paul Sabatier)*
Cotutelle internationale avec : *Universidad Autónoma de Nuevo León*

Présentée et soutenue le *31/10/2018* **par :**

Ana María HERNÁNDEZ LÓPEZ

Propriétés structurales, microstucturales et électriques du titanate de baryum dopé à l'yttrium pour l'élaboration des condensateurs multicouches

JURY

Jacques NOUDEM, Professeur à l'Université de Caen Normandie, Rapporteur
Félix SÁNCHEZ DE JÉSUS, Professeur à l'Universidad Autónoma del Estado de Hidalgo, Rapporteur
Ana María BOLARÍN MIRÓ, Professeur à l'Universidad Autónoma del Estado de Hidalgo, Examinatrice
Roman Jabir NAVA QUINTERO, Ingénieur de Recherche, KEMET México, Examinateur
Bernard DURAND, Professeur à l'Université Paul Sabatier, Encadrant
Zarel VALDEZ NAVA, Chargé de Recherche au CNRS, Encadrant
Sophie GUILLEMET-FRITSCH, Directrice de Recherche au CNRS, Directrice
Juan Antonio AGUILAR GARIB, Professeur à l'Universidad Autónoma de Nuevo León, Directeur

École doctorale et spécialité :
SDM : Sciences et génie des matériaux - CO034
Unité de Recherche :
CIRIMAT - Centre Interuniversitaire de Recherche et d'Ingénerie des Matériaux UMR CNRS 5085

ACKNOWLEDGMENTS

This thesis work was developed thanks to the support of the Postgraduate Cooperation Program (PCP-RU2I) Mexico-France, Project 229286, between the National Council of Science and Technology (CONACyT) and the Ministries of Foreign Affairs of Higher Education for the French Republic, with the participation of Kemet de México and Marion Technologies (France). I thank to the CONACyT for having awarded me the doctoral grant (number 516106) and thus promote my postgraduate studies.

I feel really fortunate for having the chance of taking the best of Mexico and France to grow at a personal and professional level. I thank to the Universidad Autónoma de Nuevo León and to the Université Toulouse III – Paul Sabatier for the honor of being PhD student in them, as well as for the support for the progress of this cotutelle.

My deepest and more sincere gratitude goes to my supervisors, Sophie GUILLEMET-FRITSCH, Juan Antonio AGUILAR GARIB, Zarel VALDEZ NAVA y Bernard DURAND; all of you have left in me a mark. Thanks for having opened me the doors and for trust in me to face this important challenge, guiding me with such patience and caring all these years. Thank you very much for giving so much of you to my education, for your time and availability and, most of all, for supporting and encouraging me to keep growing and giving the best of me always. I'll keep the best memories of the long discussions and the advantage of listen and having different points of view, being able to go farther.

To Christophe TENAILLEAU and Pascal DUFOUR, thank you so much for your support, for share your experience and knowledge with me in such valuable discussions giving me the opportunity to learn a lot from you. Thanks for your advices and guidance during this period. To Edgar REYES MELO, thanks for your availability to participate in academic discussions and contributing with interesting ideas.

To Félix SÁNCHEZ DE JESÚS, Ana María BOLARÍN MIRÓ and Jacques NOUDEM for having evaluated my thesis and grant me the honor of being part of the jury.

A big thanks to the company Kemet de México, starting with the Director of Manufacturing Operations of Cards Ariel GOVEA FLORES and the team formed by Román NAVA QUINTERO, Víctor HERNÁNDEZ and Julio PÉREZ, who since the beginning offered me their support and also in a technical way and through interesting discussions contributed greatly to this research. Special thanks to Román NAVA QUINTERO for agreeing to be part of the jury, for his availability and for sharing his experience with me.

To Joseph SARRIAS, thank you for your kindness and willingness so that through Marion Technologies it would be possible to obtain crucial results for the discussions presented in this thesis.

To Arturo CASTILLO GUZMÁN, thanks for having considered me as the right person for this great opportunity, I will always remember with great appreciation your way of believing in me and procuring my

success and wellness. Thanks also for the constant effort so that this cotutelle had the bases to be built and finished.

To Jorge Luis MENCHACA ARREDONDO my most sincere and immense gratitude, five years ago I found a great teacher and friend on my way. Thank you for believing in me, for opening doors to huge opportunities and encouraging me to be always braver. Thank you so much for having ventured to support me in this life project.

I was fortunate to work in CIRIMAT and LAPLACE laboratories at the University of Toulouse III - Paul Sabatier. In them I could experiment, learn, advance and share with people whose experience contributed to my training. My thanks to all those who work in them, as well as to my fellow doctoral students and post-doctoral students who made my stays in this university more enjoyable and with whom I was able to discuss and share ideas on multiple occasions. Special thanks to Jean-Jacques DEMAI, Marie-Claire BARTHELEMY, Benjamin DUPLOYER and Sorin DINCULESCU for their technical support in carrying out my experiments. With great appreciation I also thank Ly, Nahum, Abdé, Romain, Precious, Simo, Guillaume, Cédric, Cyril, Mateusz and Trong for their company, for the shared coffees with such interesting talks, for their support in difficult times and for the laughs.

Thanks also to my teachers at the CICFIM for contributing with their knowledge to my training.

A deep gratitude to those who gave me their friendship and support during these years in Monterrey: Monica, Roberto, Liz, Juan, Maricela, Armando, Jeane, Marco, Fernando, Oswaldo, David and Abraham, I am fortunate to have so much love from your part, thank you for so many beautiful moments, for your hugs and smiles.

Amanda, thank you for having entered with such joy in my life and allowing yourself to be part of yours, thanks for so much love and that energy that illuminates more than you imagine. I'll always remember your words accompanied by a great and warm smile.

Codorniz, thank you for welcoming me into your home and sharing that special family with me, for the hugs and comforting words, for so many laughs, for being unconditional and not leave me alone.

To all those who despite the distance have always been with me, Papitas, Pardito, Diani, Flaquito, Cesitar, Carlitos, Lau, David, Felix, Karencita, Jenn, thank you for this great friendship that has seen us grow and make our dreams become a reality, all of you are always in my heart. Thanks also to Carlitos Franco, Wilmer, Ale, Daniel and John for accompanying me in different ways with their friendship and support on this path.

I will always thank the life that during these years has given me the great gift of enlarging my family. For their immense and unconditional support, the strength they give me, so much love and joy, to help me make my dreams come true and allow me to be part of their lives: *Gaby, Jime, Santi, Roberto, Pepe, Guille and*

MariaJo, deserve my infinite thanks for allowing me to write these words today, I owe you a great part of this achievement.

In my beloved Colombia you will always find an immense part of who I am, of my heart: my beautiful family. How to thank for so much love? *To my grandmother, my aunts and uncles, my cousins, my nephews, Yaneth and Yas*: it is you who appear daily in my thoughts, thank you for enlightening my life with your existence, thank you for supporting me and always believing in my. Thank you for giving so much of you for my happiness, for encouraging me to always dream big and to receive me with open arms every time and no matter what. I love you immensely.

To the love of my life, who does not allow a single day to pass without me having a reason to fall in love more and being even happier. My life with you is the light in my eyes, my dreams at your side only become bigger and the world for me is better since you and I are walking hand in hand. It is for you *Rho* and for everything that awaits us, always together.

To those who have given their all to make my wings bigger and bigger: *my parents*. Thank you for supporting my decisions and giving me strength when I doubt them. Thank you for always being by my side and believing enough in me to make sense of all these years away from you. Thank you for showing me your love in so many ways, for taking care of me and taking care of my *little dog angels* that I miss so much. I always carry them with me, every step I have taken and I will give, has your legacy.

Contents

Figure Index

Table Index

General Introduction

Nowadays, the electronic devices are part of our lives: computers, telephones, electrical appliances are some examples. Currently the presence of electronic components is increasing more and more in industries such as the automobile and aeronautics, as well as in in the devices or processes that require automation. One of the principal components of these devices is the capacitor, which main function is the energy storage. There are multiple types of capacitors, one of the most used are the multilayer ceramic capacitors (MLCCs). The MLCCs offer essential advantages due to their low cost, one of the reasons of its predominance in the electronics market. According to the application there are different kinds of MLCCs to choose, regarding principally the capacitance they offer but also the dielectric material and its performance under different conditions, such as the temperature. The characteristics of the MLCCs are going to be determined by extrinsic and intrinsic parameters; i.e., the nature, characteristics, synthesis and treatment of the dielectric material and the production process of the capacitors. These factors can influence on the final reliability of the capacitors and hence of the devices. For this reason, it is highly important to develop ceramic materials suitable for the different markets. One of the principal strategies to obtain reliable capacitors is to focus in the tailoring of the dielectric ceramic by modifying the material composition.

Barium titanate ($BaTiO_3$) has been the most used material as the base for the dielectric of the MLCCs due to properties such as its large permittivity. To enhance its electrical properties, it needs to be modified through the inclusion of several additives and dopants in the base formulation for the dielectric. The perovskite structure of the $BaTiO_3$ has the ability to host these dopants, which according to different conditions will occupy the A or B sites in the lattice. The occupation of the dopants within the cell structure will determine the initial electrical properties, and it is assumed

that it will also determine the reliability (lifetime) of the final product. The formulation of barium titanate powders includes as dopants rare-earth elements (REE). Among them, the Y_2O_3 is the most common for the fabrication of multilayer ceramic capacitors with base-metal electrodes (BME-MLCCs) because it has a lower cost than Ho_2O_3, Er_2O_3 and Dy_2O_3 and provides similar properties. Also, cations such as Mn^{2+}, Mg^{2+} and Ca^{2+}, that can contribute to the global distribution of the electronic defects generated when the doping ions are introduced into the lattice and during the capacitors fabrication process. In addition to these dopants, additives are added aiming to modify the production conditions, like the SiO_2 used to lower sintering temperatures. The final properties will result from the interactions that barium titanate, dopants and additives can have among each other under the specific sintering conditions. The complexity of the system is increased when given some conditions, secondary phases are formed. In previous works, these secondary phases, particularly those related to Y_2O_3 doping, are believed to be responsible for the long-term failure mechanisms of MLCC's under nominal operation.

This thesis work has the objective to analyze the role of Y_2O_3 as $BaTiO_3$ dopant and its possible contribution to the formation of secondary phases. The achievement of this objective involves two experimental blocks. First, the electrical characterization of MLCCs with Y_2O_3-doped $BaTiO_3$ as dielectric by the performance of high accelerated life tests (HALT) that lead to obtain life indicators. Secondly, the development of a doping study that includes the preparation of powders and ceramics under different sintering conditions using Y_2O_3 as dopant and two kinds of $BaTiO_3$ powders (one pure and two formulated for industrial applications).

This thesis manuscript is divided in four chapters.

The first chapter is a bibliographic introduction in order to situate this work in the current context. It presents the general properties of the $BaTiO_3$, and how they can be enhanced by the use of dopants such as the Y_2O_3 in formulations that are used for its application as the dielectric material of multilayer ceramic capacitors.

The Chapter 2 describes the different experimental methods as well as the characterization techniques used in this work.

In the Chapter 3 is presented the electrical characterization of multilayer ceramic capacitors (MLCCs) using accelerated life tests (HALT) to determine the mean time to failure (MTTF) of each group of samples and perform Weibull statistical analyses that can be used in conjunction with the Arrhenius model to obtain the activation energy (E_a) value related to the failure of the capacitors under determined conditions.

In the Chapter 4 is presented the Y_2O_3-doping of two types of $BaTiO_3$ powders (one reagent grade and the other two commercially formulated) and the preparation of ceramics issued from those powders under different sintering conditions. The influence of the dopant and the presence of secondary phases over the structural and microstructural $BaTiO_3$ properties are described in this chapter.

Chapter 1

Introduction

Barium titanate ($BaTiO_3$) has attracted the attention for decades both, in the fundamental research field as in industry for device applications. This is a noteworthy ferroelectric material because it has a high ferroelectric activity, dielectric constant and spontaneous polarization (Li, Xu, Chu, Fu, & Hao, 2009) and presents a high resistivity (10^{10}–10^{12} Ω cm) (Belous, V'yunov, Glinchuk, Laguta, & Makovez, 2008). For the above mentioned, barium titanate has a great potential for technological applications in the electronics industry. In fact, due to its high dielectric constant, low dielectric loss and superior performance at high frequency, one of its most common applications is as the dielectric material for ceramic capacitors (Wang, Chen, Gui, & Li, 2016). Among these BT-based ceramic capacitors, the multilayer ceramic capacitors (MLCCs) are widely used in military, automotive and telecommunication applications in which the devices are subjected to meaningful changes in temperature, voltages and frequencies (Wang et al, 2001). Nonetheless, when the $BaTiO_3$ is pure exhibits a great change in dielectric constant near the Curie temperature (Tc) which renders the ceramic material unsuitable for capacitor applications. For this reason, the capacitor BT-based formulations must be chemically modified to meet the required capacitance-temperature characteristics (X. H. Wang et al, 2001; J. Wang et al, 2016; T. Wang, 2009).

1.1. Ceramics

Ceramics are the first material that the humanity has produced by transformation of raw materials. The word is derived from Greek *keramikos*, which means *argil*, "especially potter's clay". Ceramics

own their distinctive qualities due to the composition of the raw materials as well as the way they are processed. They are divided in two types of materials: traditional and technical ceramics. The first group (alumino-silicate) is generally produced from natural raw materials (clay, feldspar, kaolin, quartz) and they are generally implemented by casting (slip). The latter (metal-metalloid associations) are obtained by sintering or by electrofusion (the oxides are poured directly into a mold) (Fantozzi, Niepce, & Bonnefont, 2013). Actually, the second group has inspired the definition of the term "ceramics", as expressed by M. Barsoum & M. W. Barsoum (2002): "solid compounds that are formed by the application of heat, and sometimes heat plus pressure, comprising at least two elements provided one of them is a non-metal or a nonmetallic element solid. The other element(s) may be a metal(s) or another nonmetallic elemental solid(s)".

This thesis work is focused on $BaTiO_3$ ceramics. These ceramics belong to the technical ceramics classification of the electronics that are semiconductors (thermistors, resistors).

1.2. $BaTiO_3$ – Structural characteristics

Barium titanate ($BaTiO_3$) is a ceramic material that has been widely studied due to its excellent dielectric, ferroelectric and piezoelectric properties (Nikulin, 1988; He et al., 2013). It presents a stoichiometric cubic perovskite of ABO_3-type (A = alkaline-earth element and B = transition metal) containing sties with cubic environments of oxygen while B-sites are in an octahedral environment with corner-linked octahedral, as shown in Fig. 1.1. Below the Curie temperature (Tc) the $BaTiO_3$ is non-centrosymmetric, and can present a crystal distortion (Valdez-Nava et al, 2010).

Barium titanate has five crystalline forms: hexagonal, cubic, tetragonal, orthorhombic and rhombohedral, occurring at various phase transition temperatures: 1432 °C, 130 °C, 5 °C and -90 °C, respectively. The most stable phase at room temperature is the tetragonal phase; this is the most used form because of its excellent ferroelectric, piezoelectric and thermoelectric properties (Li et al, 2009).

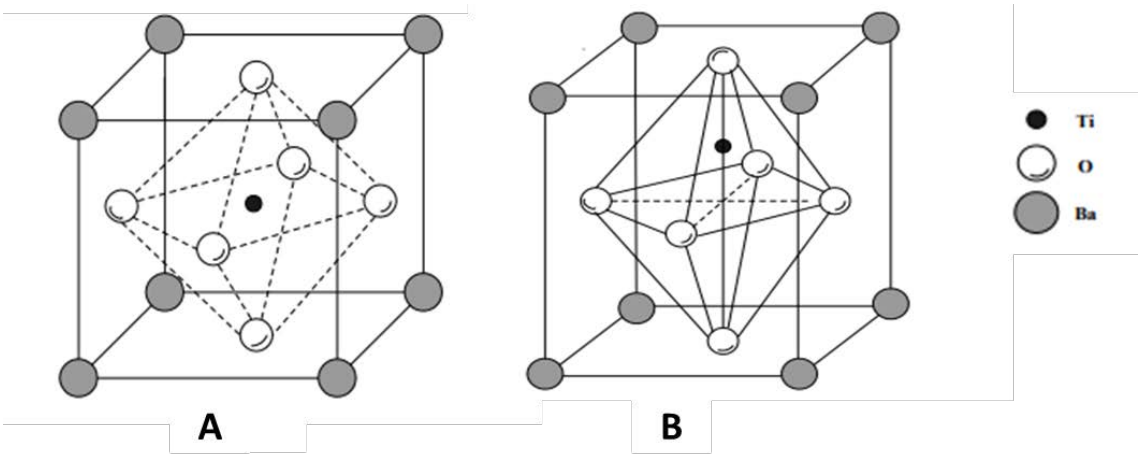

Figure 1.1. *Scheme of the $BaTiO_3$ perovskite structure. A) Cubic lattice (above Curie temperature, 120°C). B) Tetragonal lattice (below Curie temperature, 120°C). (Richerson,2005).*

1.3. Role of the dopants on the electrical properties of $BaTiO_3$

The crystal structure of this oxide belongs to the perovskite type, as shown in Fig. 1.1. This structure allows it to present a high dielectric constant. Pure BT exhibits a great change in dielectric constant near Curie temperature (Tc) 120°C (X. H. Wang et al, 2001). As a ferroelectric material, BT has a temperature point known as the Curie temperature (Tc), above which it becomes substantially non-electric, i.e. dielectric (Nikulin, 1988). If the material is above Tc (and up to 1400°C) it is centrosymmetric and paraelectric. Although barium titanate presents great electrical properties, it cannot be used in its pure form as a dielectric material.

Many efforts have been done in order to enhance barium titanate electrical properties for its different applications. One of the most common and effective methods has been to design the formulation including several additives and dopants. The difference between additives and dopants is not defined with exactitude for this field of study. However, it is usually considered that the additives contribute to the improvement of the production process while the dopants are supposed to have a direct impact over the final properties of the material, i.e. the dielectric properties. In this work this is the considered differentiation.

Cations such as Mn^{2+}, Ca^{2+} and Mg^{2+} are added as dopants that can partially compensate the electrons and holes that the system might have due to the presence of oxygen vacancies (Yoon et al., 2007; Yoon, Kang, Kwon, & Hur, 2010).

Manganese can perform a double role; it can compensate the oxygen vacancies as an acceptor being incorporated at the Ti^{4+} sites, but it can act as well as an additive inhibiting an excessive grain growth. It can take different valences (Mn^{2+}, Mn^{3+} or even Mn^{4+}) during the post-sintering process, being considered as an unstable acceptor-type dopant (Paunovic, Mitic, Marjanovic, & Kocic, 2016) but helps the material to keep a high insulation resistance while accepting electrons to form a lower oxidation state (Lee, Tseng, & Hennings, 2001).

Calcium is added to contribute as well to limit the oxygen vacancies concentration which improves the reliability, and can dissolve in the BT lattice participating in the core-shell formation (Yoon et al., 2010). The mechanism by which calcium exerts these effects has been argued along decades, which is related to things like the final application of the Ca-doped BT materials and the different ways that Ca^{2+} can be added. However, it has been reported that the occupation site of Ca^{2+} is critical for it can exert the effect of increase the resistance degradation (Fang, & Shuei, 1999; Han, Appleby, & Smyth, 1987; Völtzke, Abicht, Pippel, & Woltersdorf, 2000; Zhu, Zhang, & Chen, 2013).

The introduction of dopants that can be donors or acceptors also modifies the structure of barium titanate and can contribute to the creation of chemical inhomogeneity like core-shell structure (T. Wang, X.H. Wang, Wen, & Li, 2009; Kim et al, 2008; Armstrong, & Buchanan, 1990). Magnesium has been reported as a key cation in the formation of the core-shell structure and the inhibition of grain grown since it remains at the grain boundaries while the RE ions dissolve in the BT lattice (Huang et al., 2015; Kim et al., 2008).

The core-shell structure consists of pure ferroelectric BT (tetragonal structure) in a core that is surrounded by a shell of BT containing dopants and additives (mixture of tetragonal and cubic phases) with paraelectric behavior, as shown in the Fig. 1.2. (Kim et al, 2008). Hennings and Rosenstein (1984) reported the formation mechanism of this structure. They were able to show that the cores are the same phases as the shells, since the paraelectric shells grew epitaxially on the ferroelectric cores. Considering the core-shell structures are not thermodynamically stable, its formation will be affected both by the sintering temperature and the donor-acceptor ratio (T. Wang et al, 2009).

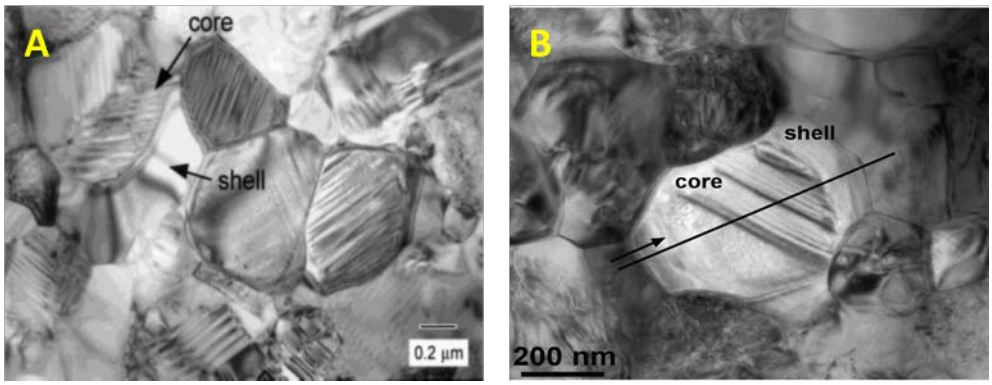

Figure 1.2. *Transmission electron micrographs of core-shell structures in doped BT ceramics. (A) TEM bright field image of a X7R-type $BaTiO_3$ ceramics by Grogger, Hofer, Warbichler, Feltz, & Ottlinger, (1998). (B) TEM of a typical core-shell grain in a BT specimen doped with yttrium and magnesium by Kim et al. (2008).*

The microstructure of the ceramics resulting from the elaboration process will have an influence on the dielectric properties. For instance, the milling process can cause defects on the particles' surface and activate the diffusion of the additives into the grains. It has been reported that as the milling time increases, the shell region gets thicker and the core region gets smaller, leading to a high chemical homogeneity at the core-shell interface increases (Wang et al., 2009).

The formulation of barium titanate for its use in ceramic capacitors also includes sintering aids like SiO_2. It is one of the most common because it has been reported to participate in the formation of a liquid phase that helps to reduce the sintering temperature and to a more uniform dispersion of the

dopants. SiO_2 has the ability to form a liquid phase from the ternary system BaO-TiO_2-SiO_2, diminishing the eutectic point from 1320°C to near 1260°C (Felgner, Müller, Langhammer, & Abicht, 2001; Liu & Roseman, 1999; Ösküz, Torman, S. Sen, & U. Sen, 2016). This ternary eutectic point is well known and corresponds to the $BaTiO_3$ – $Ba_6Ti_{17}O_{40}$ system at approximately 1330 °C (Felgner et al., 2001). When SiO_2 is present, this temperature decreases to about 1280 °C - 1260 °C. This is the reason why SiO_2 is considered as a suitable additive to produce ceramics with high density while lowering the sintering temperature, and it may even induce an improvement in the dielectric properties of BT (Öskus et al., 2016; Wu et al., 2007). Cheng (1989) also reported that the presence of SiO_2 and TiO_2, leaded to the formation of a liquid-phase former that enhanced the ionic diffusion, resulting in a uniform microstructure. This liquid phase also purified the grain interior, increasing the grain conductivity. He also evidenced that the SiO_2 and TiO_2 are located at the grain boundaries influencing only the microstructure, not the electrical properties. The liquid phase has been evidenced in studies such as the one conducted by Wu et al. (2007) through TEM analyses as shown in Fig. 1.3.

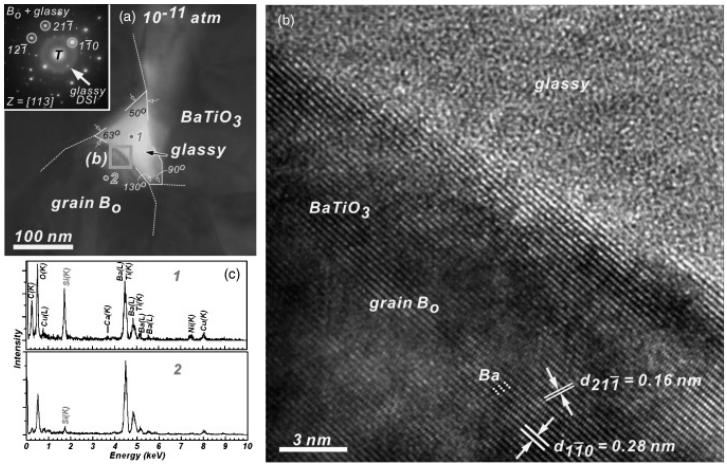

Figure 1.3. *(a) Glassy second phase at triple-grain junction with selected area diffraction patterns of $BaTiO_3$ grain inset (BF image), (b) high-resolution image of $BaTiO_3$-glass interface showing an amorphous nature, and (c) energy-dispersive X-ray spectroscopy spectra for triple junction and $BaTiO_3$ grain (Bo) (TEM) (Wu et al., 2007).*

Despite the advantages of using sintering additives, the interactions that can take place between them and the BT matrix, can turn the structural and electrical nature modifications of the doped material into undesired ways. Chemical defects and even secondary phases, such as $Ba_2TiSi_2O_8$ and $Ca_2Y_8Si_6O_{26}$ have been reported in formulated BT-based X7R MLCCs (Wu et al., 2007). Those phases could lead to the deterioration of the electrical properties that are supposed to be enhanced by the additives and dopants presence (Liu & Roseman, 1999; Öskus et al., 2016). Yan et al. (2016) reported that when adding 0.5 wt% of SiO_2 to $BaTiO_3$, no second phase was detected and it showed homogeneous microstructure with small grains. However, with further increase of SiO_2 addition to 1 and 2 wt%, $Ba_2TiSi_2O_8$ secondary phase was detected and the dielectric constant of those ceramics at the *Tc* decreased gradually.

Finally, rare-earth oxides are added as well as dopants and they can interact, due to their donor or acceptor ionic behavior, creating chemical defects and activating compensation mechanisms. The doping of BT with rare-earth ions (e.g. Y^{3+}, Dy^{3+}, Ho^{3+}) improves its dielectric performance. For this reason, the researches in materials science and electronics engineering to improve the dielectric properties of the $BaTiO_3$ as a dielectric base material and modify it directing the objectives towards the market necessities, has highly increased the last decades. Gong, Wang, Zhang, & Li (2016) reported an increase of the reliability of co-doped $BaTiO_3$-based MLCCs when using Ho^{3+} and Dy^{3+}. These dopants present a synergistic effect exhibiting a better insulation degradation behavior compared with the doped samples containing just one of the two. Similar results have been reported for donor- and acceptor-cosubstituted BT, which have shown a better insulation resistance and life stability. The most common of these systems is $BaTiO_3$-MgO-R_2O_3, with R = La^{3+}, Gd^{3+}, Dy^{3+}, Ho^{3+}, Er^{3+}, Y^{3+}, Yb^{3+} (Kuo, Wang & Tsai, 2006). The doping behaviors of R = Ho^{3+}, Dy^{3+} and Y^{3+} have been reported by authors like Makovek, Samardžija, & Drofenik, (2004). They observed that these ions have similar solubility in $BaTiO_3$ lattice and their incorporation into it is mainly dependent of the starting composition of the powders. The Ba- or Ti-richness of the powder affects

the measure in which the RE ions are going to be incorporated in each site. Park et al, (2009) compared the doping behaviors of these RE ions in $BaTiO_3$-MgO-R_2O_3 systems, obtaining the densest ceramics with the Dy^{3+} ions, which exhibited the better shell formation as well due to a higher solubility compared to the Y^{3+} and Ho^{3+} ions. However, Y- and Ho-doped ceramics showed a most stable microstructure at high temperature. The similarities in the doping behavior of these particular three ions can be due to its similar ionic radius. Some of the BT dopants with their respective ionic radii according the coordination site they can occupy are shown in the Table 1.1. The ionic radius determines the occupation site in the BT lattice of the RE dopants. Larger RE ions such as La^{3+} and Sm^{3+} are predominantly donor dopants, occupying the A-site. Smaller ions like the Yb^{3+} are acceptor dopants; they occupy the B-site. The ions with intermediate ionic size (Dy^{3+}, Ho^{3+}, Er^{3+}, Y^{3+}) can be placed both in A- and B-sites, presenting both donor and acceptor dopant behavior (Kuo et al, 2006; Park et al, 2009; Tsur, Hitomi, Scrymgeour, & Randall, 2001a).

Table 1.1. *Effective ionic radii of various elements (Park et al, 2009; Tsur et al, 2001a).*

Ion	**Ionic radius (Å)**	
	B-site (6 coordination)	**A-site (12 coordination)**
Ba^{2+}		1.610
Ti^{4+}	0.605	
Mg^{2+}	0.720	
Dy^{3+}	0.912	1.255
Ho^{3+}	0.901	1.234
Y^{3+}	0.900	1.234

One of the most common observations with the RE-doped BT systems is the change of the crystalline structure due to the insertion of RE ions into the BT lattice, either in A- or B-sites. The

presence of dopants can lead to a transformation from a well-defined tetragonal phase to a mixture of tetragonal phases or even a new structural phase. In the literature this change of phase is usually described as a mixture of tetragonal and cubic phases and denominated as a “pseudo-cubic” phase. As previously mentioned, the additives and sintering conditions affect the microstructure as well. For instance, the diffusion of oxygen atoms through the grain boundaries into the grains, to annihilate oxygen vacancies, can be faster during the cooling step. As a result, barium vacancies remain at the grain boundaries and form high-resistance regions. This increases the ceramics resistivity (Cheng, 1989). Besides the dielectric properties, the ferroelectric characteristics can also be modified. Shifts in transition temperatures or the broadening of the ε-T curve (diffuseness of the ferroelectric transition) can be some of the effects of dopants. Depending on the nature of the incorporated dopant in the BT lattice, it can go from classical ferroelectric to diffuse ferroelectric or even relaxor (Petrović, Bobić, Ramoška, Banys, & Stojanović, 2011). Also, the electrical behavior can be altered by the dopant concentration, which can lead to a dielectric or semi-conductivity behavior (Urek, Drofenik, & Makovec, 2000).

Two of the most principal applications for barium titanate are the positive temperature coefficient resistors (PTCRs) and the multilayer ceramic capacitors (MLCCs). The formulation for both of them is tailored with the incorporation RE cations to control conductivity and electrical degradation, respectively (Tsur, Dunbar & Randall, 2001b). The trivalent RE cations are of particular interest thanks to its amphoteric behavior. These substitutions cause a charge imbalance in the system that can be compensated either ionically under oxidizing conditions or electronically under reducing conditions (Fu, Mi, Wessel, & Tietz 2008; Makovek et al., 2004). Compensation mechanisms have been proposed (J. Zhi, Chen, Y. Zhi, Vilarinho, & Baptista, 1999; Jeong, Lee, & Han, 2005; Paredes-Olguín, Lira-Hernández, Gómez-Yañez, & Espino-Cortés, 2013) as illustrated below using the Kröger-Vink notation, when the dopant is Y_2O_3:

- When Ba^{2+} is substituted:

$$Y_2O_3\ (in\ BaTiO_3) \rightarrow 2Y_{\dot{B}a} + 2e' \qquad (1)$$

$$3Y_2O_3\ (in\ BaTiO_3) \rightarrow 6Y_{Ba}^{\cdot} + V_{Ti}^{''''} + V_{Ba}^{''} \qquad (2)$$

- When Ti^{4+} is substituted:

$$Y_2O_3\ (in\ BaTiO_3) \rightarrow 2Y_{Ti}' + 2h^{\cdot} \qquad (3)$$

$$Y_2O_3\ (in\ BaTiO_3) \rightarrow 2Y_{Ti}' + V_O^{\cdot\cdot} \qquad (4)$$

All mechanisms (1) to (4) might be active at the same time. However, the sintering parameters (temperature and P_{O_2}) will lead to the predominance of one of them. The dominant mechanism will determine the electrical properties of the doped sample, such as its resistivity. A decrease in the resistivity can be due to the presence of charge carriers, as in mechanisms (1) and (3). If (1) is the prevailing mechanism, ceramic will behave as an *n*-type semiconductor. Mechanism (3) will lead to a *p*-type behavior. On the other hand, if mechanism (4) is leading, the ceramic can be an oxygen conductor. On the basis of thermodynamic analyses, the mechanisms (3) and (4) are more probable to occur (Zhi et al., 1999; Paredes-Olguín et al., 2013). However, in Y-doping cases, it has been observed that if the concentration is less than 1 %, mechanism (1) is prevalent (Paredes-Olguín et al., 2013). The behavior as donor or acceptor of these RE cations will be also affected by the A/B ratio. An excess of BaO or TiO_2 will influence the probability of A- or B-site occupation. In the presence of an BaO excess, Y^{3+} acts as an acceptor, while it behaves like a donor if there is an TiO_2 excess (Makovek et al., 2004). Y_2O_3 is a common BT-dopant and the most suitable rare-earth oxide for the MLCCs production because it offers the electrical properties enhancement advantages as the Ho_2O_3, Er_2O_3 and Dy_2O_3 at lower costs (Zhang et al., 2016).

Known as the “magic ions”, Dy^{3+}, Ho^{3+} and Y^{3+}, are categorized as helpful for the lifetime of the MLCCs (Tsur et al., 2001a,b) for this reason, the amphoteric RE cations have been the most used for this type of applications. Since the optimization of industrial processes is crucial it is a determining factor as well at the moment to set the sintering parameters. Indeed, low sintering temperatures are preferred by industries for economic reasons.

In this work the Y_2O_3 was chosen as dopant because of its wide use in the dielectric formulations for ceramic capacitors. The thermodynamic and kinetic factors that might influence its occupation site as well as the electrical properties of the ceramics will be discussed below.

1.4. Role of Y_2O_3

The formulation of $BaTiO_3$ (BT) materials, used in the manufacturing of the MLCCs, must be tailored to control the electrical properties, especially at high temperature and under high electric field (Ashburn & Skamser, 2008; Yoon, Park, Hong & Sinn, 2007). For this purpose, several additives and dopants are added to $BaTiO_3$. One of the most used dopants is the Y_2O_3, which is added with the aim to generate compensation mechanisms that contribute to improving the reliability of the capacitors.

The Y^{3+} has an ionic radius of 0.107 nm, it is intermediate between that of the Ba^{2+} ion (0.161 nm) and the Ti^{4+} ion (0.06 nm). Therefore Y^{3+} can occupy either Ba^{2+} or Ti^{4+} cation site in the BT lattice (Wang et al., 2014; Tsur et al., 2001a). This allows Y^{3+} to behave as acceptor or donor according to the position in the lattice. The inclusion of the Y^{3+} ion in the BT structure depends on kinetic and thermodynamic factors (Makovec et al., 2004). It is reported that the formation energy of $Y_{Ba}^{\cdot} + V_{Ba}^{''}$ is 7.23 eV whereas it is only 4.35 eV to form a $Y_{Ba}^{\cdot} + V_{Ti}^{''''}$ defect (Belous, V’yunov, Kovalenko, & Makovec, 2005). The partial pressure of oxygen and sintering temperature will also induce the formation of Ba^{2+} or Ti^{4+} vacancies, leading Y^{3+} to occupy either both or one of the sites (Belous et al., 2005; Paredes-Olguín et al., 2013). This will be influenced also by the Ba/Ti ratio,

the dopant concentration and its solubility. Yttrium cations have different solubility in Ba- and in Ti-sites. Zhi et al. (1999) indicated a solubility of Y^{3+} at the Ba-site of about 1.5 at% when sintered in air at 1440 – 1470°C, while it reaches 4 at% when sintered under reducing conditions (V'yunov, Kovalenko, Belous, & Belyakov, 2005). For the Ti-sites instead, the solubility is higher, approximately 12.2 at% at 1515°C when sintering in air. Wang et al. (2014) reported that the introduction of Y^{3+} in the BT lattice, can lead to structural changes, as the phase transformation from tetragonal to cubic.

The amount of yttrium ions can be spent in different processes occurring in the system during the processing of the ceramic materials. Belous et al. (2008) studied yttrium-doped BT, identifying in which processes is expended the dopant. It is known that the raw materials may contain impurities. In this case paramagnetic impurities were identified as able to occupy Ti-sites. Thus, some part of the Y^{3+} can participate in an exchange of them. Yttrium also influences the charge compensation mechanisms. And as a collateral effect, it has been found it can participate in the formation of precipitates such as $Ba_6Ti_{17}O_{40}$ and $Y_2Ti_2O_7$. These secondary phases have been usually found when the solid solubility of the dopant in the BT is surpassed.

With the appropriate amount of dopants, the structural, optical and electrical properties of a BT-doped system can be improved (Hernández Lara et al., 2017). On the other hand, there are numerous reports where the formation of secondary phases has been observed when doping BT with rare-earth elements (REE) (Belous et al., 2008; Yoon et al., 2007; Zhang et al., 2016). The formation of these precipitates depends on different factors, i.e. the sintering conditions and the dopant concentration (M. T. Buscaglia, Viviani, M. Buscaglia, Bottino, & Nanni, 2002). These secondary phases are usually formed when the amount of dopant is above of its solubility limit in the BT-lattice. This excess of dopant can lead to its interaction with other free ions present in the system, like Ti^{4+}. Then, if the conditions are appropriate, a precipitate will be formed. Some of the secondary phases that have been observed are $Ba_2TiSi_2O_8$ (Wu, Wang, McCauley, Chu, & Lu,

2007), $Ba_6Ti_{17}O_{40}$ (Belous et al., 2008), Y_2TiO_5 (Yoon et al., 2007), and one of the most common when doping with RE oxides (Dy_2O_3, Er_2O_3, Y_2O_3 and Ho_2O_3), is the pyrochlore-type phase, $R_2Ti_2O_7$ (Jeong et al., 2005). Among the pyrochlores, $Er_2Ti_2O_7$ (Buscaglia et al., 2002), $Gd_2Ti_2O_7$ (Hernández Lara et al., 2017), $Ho_2Ti_2O_7$ (Makovec et al., 2004) and $Y_2Ti_2O_7$ (Yoon et al., 2007; Zhang et al., 2016) have been reported. $Y_2Ti_2O_7$ is suspected to be detrimental to the reliability of BT-based MLCCs (Yoon et al., 2007; Zhang et al., 2016).

The effect of the presence of these secondary phases over the $BaTiO_3$ structural and dielectric properties is of high interest for industrial applications. Several authors have reported a detrimental effect of $Y_2Ti_2O_7$ on BT dielectric performance (Wu et al., 2007; Yoon et al., 2007; Zhang et al., 2016). The yttrium pyrochlore ($Y_2Ti_2O_7$) has a highly conductive nature and is suspected to be related with the resistance degradation of the material through the acceleration of oxygen vacancies electromigration (Zhang et al., 2016). The investigation of the formation parameters and possible effects of this phase is of high interest in the academic and industrial field since Y_2O_3 is a one of the most frequent dopants used in the MLCCs production.

1.5. Sintering atmosphere influence over dopant occupancy in BT-doped ceramics

One of the most important parameters to obtain a BT material with the appropriate properties for its application as ceramic dielectric is the oxygen partial pressure (P_{O_2}) during sintering treatment. P_{O_2} affects the incorporation of dopants into the BT-lattice (Buscaglia et al., 2002; Tsur et al., 2001b). The site occupancy of dopants in BT-lattice is restrained by the valence of the ion, its size, the A/B ratio (i.e. the activity of Ti in the system) and by the oxygen vacancies concentration. It has been observed that the P_{O_2} influences the charge compensation mechanisms (ionically or electronically) dictating a change in the A/B ratio in the perovskite lattice, which can lead to the

formation of precipitates. Furthermore, the changes induced by the P_{O_2} significantly affects the electrical behavior (Fu et al., 2008).

Either a reducing or an oxidizing sintering atmosphere can be used for the production of BT-doped ceramics. However, taking into account the cost reduction at industry level due to the use of nickel for the inner electrodes instead of the expensive noble metals previously employed, (palladium or silver palladium alloys), one of the factors that forces the use of reducing atmospheres is to protect Ni-electrodes from oxidation. Thus, the process must to be carried out in reducing atmospheres, such as CO/CO_2 or N_2/H_2, being the latter the most used (Albertsen, Hennings, & Steigelmann, 1998; Hagenbeck & Waser, 1998; Okino et al., 1994). Meanwhile, in the research field, either reducing or oxidizing atmospheres have been utilized.

The control of P_{O_2} employed during the sintering of BT-doped ceramics can even contribute to the formation of Ti^{3+} ions, assuming the substitution of Y^{3+} for Ba^{2+} in the BT-lattice. Tien & Carlson (1963) performed some experiments to determine the relation between the degree of oxidation and the resistivity-temperature characteristics of Y-doped polycrystalline BT. They found that the oxygen partial pressure increases the slope of temperature-resistivity curves above *Tc* and the resistivity at room temperature. This behavior is related to the amount of Ti^{3+} present in the system. Under equilibrium conditions, the relation between P_{O_2} and Ti^{3+} concentration is described by: $2Ti^{4+} + O^{2-} \rightleftharpoons 2Ti^{3+} + ½\ O_2$. Previous reaction is overlapped by the Y^{3+} dopant, its level and the prevailing equilibrium conditions will then determine the concentration of Ti^{3+}. Following the expression for the equilibrium constant $\left(K = \frac{(Ti^{3+})^2 {P_{O_2}}^{1/2}}{(Ti^{4+})^2(O^{2-})}\right)$, $[Ti^{3+}]$ is constant at a given temperature and equilibrium conditions as determined by dopant amount and the prevailing P_{O_2}. If the P_{O_2} is constant as the temperature is decreasing, then the equilibrium constant will be decreasing which as well will dictate an increase of Ti^{3+} concentration, and this will influence the electrical behavior of the material (Tien & Carlson, 1963).

Tsur et al. (2001a, 2001b) investigated the site occupancy of rare earth ions in the BT-lattice according to the atmosphere conditions. They found that when BT is fired at low P_{O_2} and high temperatures, dopants such as Er, Y, Ho and Dy are amphoteric (Tsur et al., 2001a). They also observed that samples fired in air present larger cell volumes than the ones sintered in reduced atmospheres. The latter is due to the lower presence of oxygen vacancies in air sintered samples, thus site occupancy is directed towards more B-site occupancy (Tsur et al., 2001b).

1.6. Multilayer ceramic capacitors (MLCCs)

In the past decades, the electronic devices design has gone toward the miniaturization and reduction of power consumption. This trend requires high reliability for the electronic components (Shimada, Utsumi, Yonezawa, & Takamizawa, 1981). Among the most important electronic items are the Multilayer Ceramic Capacitors (MLCCs) (Fig. 1.4). MLCCs were developed in the 1960s and its use increased in the 1980s (Pan & Randall, 2010). These pieces are used in strongly growing markets (Acosta, Zang, Jo & Rödel, 2012), making up approximately 30% of the total components in a typical hybrid circuit module (Futureelectronics.com. (n.d.)). They present an economical volumetric efficiency for capacitance and high reliability. MLCCs are characterized by a high dielectric constant (*K*) and thinner dielectric layers (Jain, Fung, Hsiao, & Chan, 2010). MLCCs can be broadly divided, depending on the application, into two types: for temperature compensation and for high-dielectric constant. MLCCs for high-dielectric constant use barium titanate as the dielectric component. Among this type of capacitors, the X7R is the most stable, covering a broad spectrum of applications. X7R formulations are called “temperature stable” ceramics, which allows apply them widely in miniaturization of electronic components (Li, Zhang, Zhou, Chen, & Wang, 2007).

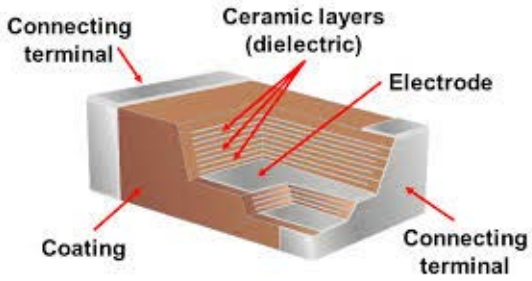

Figure 1.4. *Basic structure of a multilayer ceramic capacitor.*

Multilayer ceramic capacitors are classified in three classes according the Electronic Industry Alliance (EIA). Class I are Temperature Compensating capacitors, they are known as COG (a.k.a. NPO). Class II is known as Stable capacitors, the most common among them are X7R, X5R and Y5V. Finally, class III: Z5U, known as the General Purpose capacitors (Ashburn, & Skamser, 2008; Pan & Randall, 2010; Standard, E.I.A., 2002). The specifications of classes I and II are shown in Table 1.2. They can be classified by its rated voltage, tolerance, type of dielectric, capacitance, packaging type and case size. The most common values for capacitance are 10 nF, 100 nF and 1 µF. The rated voltage (RV) can be between 4 V and 10 kV, and the most common capacitors have a RV of 16, 25, 50 or 100 V (Futureelectronics.com. (n.d.)). The EIA specification for X7R MLCCs is a temperature variation of capacitance (ΔC/C) within ± 15 % from -55 °C to 125 °C. (Li et al., 2007; Park et al., 2009).

Table 1.2. *Types of MLCCs and specifications (Kahn, 1981; Kishi Mizuno, & Chazono, 2003).*

EIA Designation	**Class**	**Temperature range (°C)**	**ΔC/C (%)**	***K* value up to**	**BT content (%)**	**Other dopants**	**Grain size (µm)**
C0G (NPO)	I	-55 to 125	± 30	100	10-50	TiO_2, $CaTiO_3$, $Nd_2Ti_2O_7$	1
X7R	II	-55 to 125	± 15	4000	90-98	MgO, MnO, Nb_2O_5, CoO, Rare-earth elements	<1.5
Z5U	II	10 to 85	+ 22, -56	14000	80-90	$CaZrO_3$, $BaZrO_3$	3-10
Y5V	II	-30 to 85	+22, -82	18000	80-90	$CaZrO_3$, $BaZrO_3$	3-10

Multilayer ceramic capacitors of Classes II and III exhibit aging characteristics. The capacitance of Class II devices typically falls 10 % with applied voltages of 50 to 70 % of the device's maximum working voltage. Class III devices lose capacitance starting at 10 % of the maximum working voltage and exhibit as little as 30% of their nameplate value at 90 % of their voltage range (Pan & Randall, 2010).

The capacitor technology has changed according to the industrial and commercial demands. Since many of MLCCs applications are manipulated at extreme operational conditions, like high temperatures (beyond 200 °C), the capacitors must be processed out under high degree requirements to ensure a high-yield, large-scale, low-cost production process (Kahn, 1981). MLCCs with X7R-formulation based on $BaTiO_3$ dielectric material, are usually produced under a sintering process with a temperature between 1200 °C and 1300 °C and low P_{O_2} of about 10^{-9} – 10^{-11} atm. This is followed by a re-oxidation step at 800° - 1000°C in P_{O_2} between 10^{-6} – 10^{-8} atm. (Wu et al., 2007). This last step contributes as well to the attempt to diminish the contribution of oxygen vacancies (Pan & Randall, 2010). A whole general view of the industrial production process of these capacitors is shown in the Fig. 1.5.

The characteristics of each MLCC type challenge a highest quality for its production. Each step during this process must be carefully supervised, taking care of some key factors that will critically influence the lifetime and resistance degradation of the capacitors. Some of the considerations to take into account, as it has been explained, are the characteristics of the starting BT powder and the features of the final formulation to be applied, i.e. optimization of additives and dopants. There are as well some aspects related particularly to the process, as the coating of the dielectric material and the control of atmospheric conditions during thermal processing. As long as the production steps are under control, the process will be robust ensuring a high-quality product (Ashburn & Skamser, 2008).

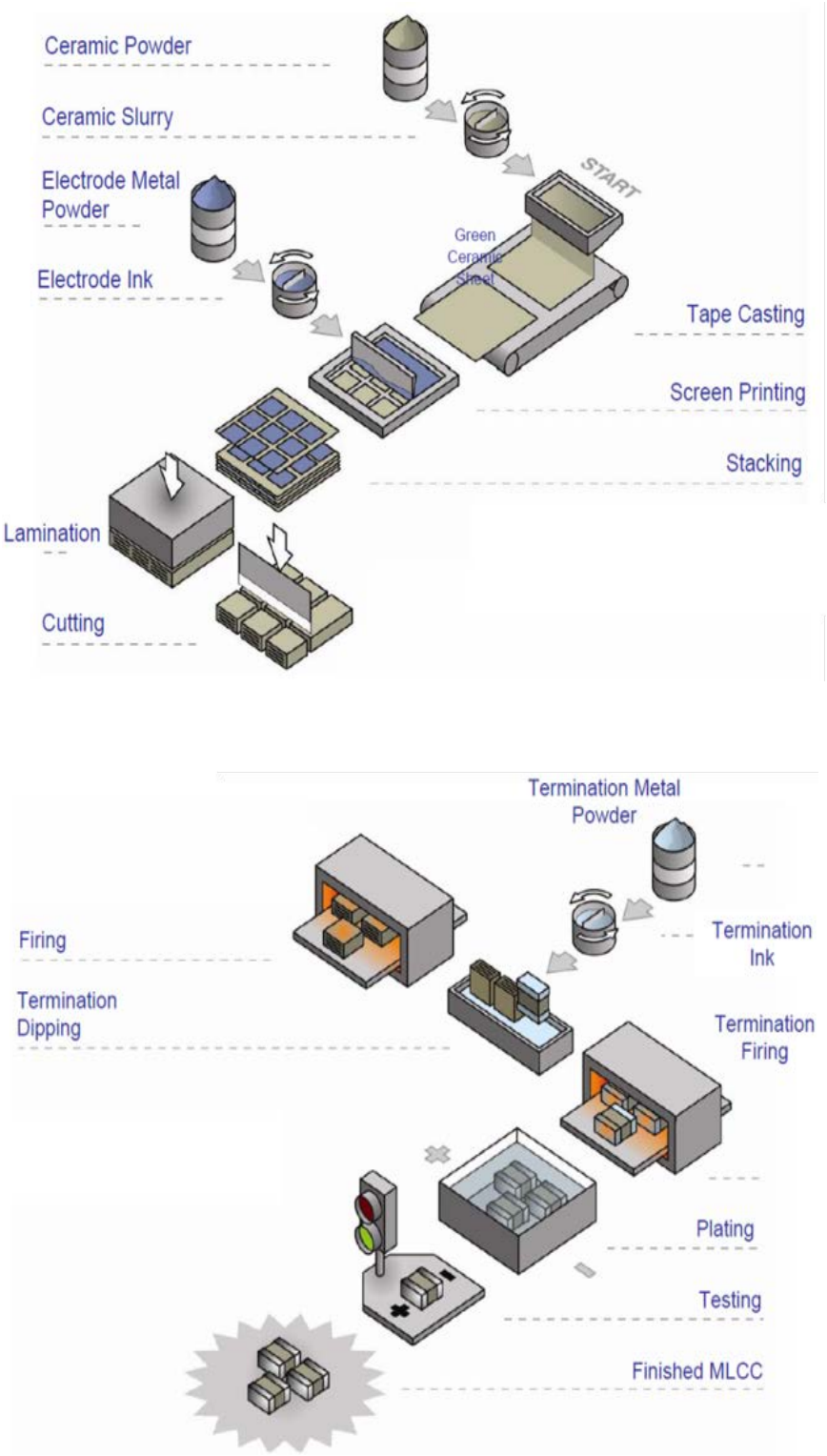

Figure 1.5. *MLCCs production process. Adapted from Basics of Ceramic Chip Capacitors by Johanson Dielectrics. 2008.*

Nevertheless, even though research in the last decades has allowed to the industries the optimization of the production process, exhibiting a great improvement in the technology of the electronic field, some failures are still observed in some cases.

Two failure modes have been identified in Base-Metal-Electrode (BME) Multilayer Ceramic Capacitors (MLCCs): catastrophic and slow degradation. Catastrophic failures are mainly due to present processing defects (extrinsic defects), such as voids, cracks and delaminations. These are characterized by a time-accelerating increase in leakage current. On the other hand, the slow degradation failures are related with the electromigration of oxygen vacancies, which are considered intrinsic defects, and are characterized by a near-linear increase in leakage current against stress time (Liu, 2015).

These failure modes can be distinguished using a 2-parameter Weibull plot. The early (catastrophic) failures can be distinguished by a slope parameter of $\beta > 1$. This β value indicates that these are not infant mortalities (Liu & Sampson, 2012).

Early failures have been related to the decrease of the dielectric thickness, being triggered by external electrical overstress. This has represented a problem to control a high reliability with the miniaturization of MLCCs. The breakdown leakage current that characterize an early failure is an avalanche-like type (Liu & Sampson, 2012). Since, as mentioned before, these failures are related to extrinsic defects, i.e. minor construction defects introduced during fabrication of the capacitors, the production control and quality requirements are a crucial factor to obtain a reliable final product.

It has been reported that insulation resistance (IR) degradation of BT-based BME-MLCCs might be related with three probable aspects: the dielectric layer, the BT grain boundaries, and the internal electrode interfaces between Ni-$BaTiO_3$ (Liu, 2015).

References

Acosta, M., Zang, J., Jo, W., & Rödel, J. (2012). High-temperature dielectrics in $CaZrO_3$-modified $Bi_{1/2}Na_{1/2}TiO_3$-based lead-free ceramics. *Journal of the European Ceramic Society*, *32*(16), 4327-4334.

Albertsen, K., Hennings, D., & Steigelmann, O. (1998). Donor-acceptor charge complex formation in barium titanate ceramics: Role of firing atmosphere. *Journal of electroceramics*, *2*(3), 193-198.

Ashburn, T., & Skamser, D. (2008, January). Highly accelerated testing of capacitors for medical applications. In *Proceedings of the 5th SMTA Medical Electronics Symposium*. California, USA.

Armstrong, T. R., & Buchanan, R. C. (1990). Influence of Core-Shell Grains on the Internal Stress State and Permittivity Response of Zirconia-Modified Barium Titanate. *Journal of the American Ceramic Society*, *73*(5), 1268-1273.

Barsoum, M., & Barsoum, M. W. (2002). Fundamentals of ceramics. CRC press.

Belous, A., V'yunov, O., Kovalenko, L., & Makovec, D. (2005). Redox processes in highly yttrium-doped barium titanate. *Journal of Solid State Chemistry*, 178(5), 1367-1375.

Belous, A., V'yunov, O., Glinchuk, M., Laguta, V., & Makovez, D. (2008). Redox processes at grain boundaries in barium titanate-based polycrystalline ferroelectrics semiconductors. *Journal of materials science*, *43*(9), 3320-3326.

Buscaglia, M. T., Viviani, M., Buscaglia, V., Bottino, C., & Nanni, P. (2002). Incorporation of Er^{3+} into $BaTiO_3$. *Journal of the American Ceramic Society*, 85(6), 1569-1575.

Cheng, H. F. (1989). Effect of sintering aids on the electrical properties of positive temperature coefficient of resistivity BaTiO3 ceramics. *Journal of Applied Physics*, 66(3), 1382-1387.

Fang, T. T., & Shuei, J. T. (1999). Experimental assessment of the inhibition of reduction of Ca^{2+}-doped barium titanate in a reducing atmosphere. *Journal of materials research, 14*(5), 1910-1915.

Fantozzi, G., Niepce, J. C., & Bonnefont, G. (2013). *Les céramiques industrielles: Propriétés, mise en forme et applications*. Dunod.

Felgner, K. H., Müller, T., Langhammer, H. T., & Abicht, H. P. (2001). Investigations on the liquid phase in barium titanate ceramics with silica additives. *Journal of the European Ceramic Society, 21*(10), 1657-1660.

Fu, Q. X., Mi, S. B., Wessel, E., & Tietz, F. (2008). Influence of sintering conditions on microstructure and electrical conductivity of yttrium-substituted $SrTiO_3$. *Journal of the European Ceramic Society, 28*(4), 811-820.

Grogger, W., Hofer, F., Warbichler, P., Feltz, A., & Ottlinger, M. (1998). Imaging of the core–shell structure of doped $BaTiO_3$ ceramics by energy filtering TEM. *Physica status solidi (a), 166*(1), 315-325.

Gong, H., Wang, X., Zhang, S., & Li, L. (2016). Synergistic effect of rare-earth elements on the dielectric properties and reliability of $BaTiO_3$-based ceramics for multilayer ceramic capacitors. *Materials Research Bulletin, 73*, 233-239.

Guha, J. P. and Kolar, D., Phase equilibria, sintering characteristics and dielectric properties in the BaTiO3-rich portion of the system $BaO–TiO_2–SiO_2$. In *5th Conference on Ceramics for Electronics*, Liblice, 1974, pp. 1–9.

Hagenbeck, R., & Waser, R. (1998). Influence of temperature and interface charge on the grain-boundary conductivity in acceptor-doped $SrTiO_3$ ceramics. *Journal of applied physics, 83*(4), 2083-2092.

Han, Y. H., Appleby, J. B., & Smyth, D. M. (1987). Calcium as an acceptor impurity in $BaTiO_3$. *Journal of the American Ceramic Society, 70*(2), 96-100.

He, F., Ren, W., Liang, G., Shi, P., Wu, X., & Chen, X. (2013). Structure and dielectric properties of barium titanate thin films for capacitor applications. *Ceramics International, 39*, S481-S485.

Hennings, D., & Rosenstein, G. (1984). Temperature-Stable Dielectrics Based on Chemically Inhomogeneous $BaTiO_3$. *Journal of the American Ceramic Society, 67*(4), 249-254.

Hernández Lara, J. P., Pérez Labra, M., Barrientos Hernández, F. R., Romero Serrano, J. A., Ávila Dávila, E. O., Thangarasu, P., & Hernández Ramirez, A. (2017). Structural Evolution and Electrical Properties of $BaTiO_3$ Doped with Gd^{3+}. *Materials Research, 20*(2), 538-542.

Huang, X., Liu, H., Hao, H., Zhang, S., Sun, Y., Zhang, W., ... & Cao, M. (2015). Microstructure effect on dielectric properties of MgO-doped $BaTiO_3$–$BiYO_3$ ceramics. *Ceramics International, 41*(6), 7489-7495.

Jain, T. A., Fung, K. Z., Hsiao, S., & Chan, J. (2010). Effects of BaO–SiO_2 glass particle size on the microstructures and dielectric properties of Mn-doped Ba(Ti, Zr)O_3 ceramics. *Journal of the European Ceramic Society*, 30(6), 1469-1476.

Jeong, J., Lee, E. J., & Han, Y. H. (2005). Electrical properties of holmium-doped $BaTiO_3$. *Japanese journal of applied physics*, 44(6R), 4047.

Kahn, M. (1981). Multilayer Ceramic Capacitors-Materials and Manufacture. *AVX Technical Information Series*.

Kim, C. H., Park, K. J., Yoon, Y. J., Hong, M. H., Hong, J. O., & Hur, K. H. (2008). Role of yttrium and magnesium in the formation of core-shell structure of $BaTiO_3$ grains in MLCC. *Journal of the European Ceramic Society, 28*(6), 1213-1219.

Kishi, H., Mizuno, Y., & Chazono, H. (2003). Base-metal electrode-multilayer ceramic capacitors: past, present and future perspectives. *Japanese Journal of Applied Physics, 42*(1R), 1.

Kuo, D. H., Wang, C. H., & Tsai, W. P. (2006). Donor-and acceptor-cosubstituted $BaTiO_3$ for nonreducible multilayer ceramic capacitors. *Ceramics international, 32*(1), 1-5.

Lee, W. H., Tseng, T. Y., & Hennings, D. (2001). Effects of ceramic processing parameters on the microstructure and dielectric properties of $(Ba_{1-x}Ca_x)(Ti_{0.99-y'}Zr_yMn_{0.01})O_3$ sintered in a reducing atmosphere. *Journal of Materials Science: Materials in Electronics, 12*(2), 123-130.

Li, B., Zhang, S., Zhou, X., Chen, Z., & Wang, S. (2007). Microstructures and dielectric properties of Y/Zn codoped BaTiO3 ceramics. *Journal of materials science*, 42(13), 5223-5228.

Li, W., Xu, Z., Chu, R., Fu, P., & Hao, J. (2009). Structure and electrical properties of $BaTiO_3$ prepared by sol–gel process. *Journal of Alloys and Compounds, 482*(1), 137-140.

Liu, G., & Roseman, R. D. (1999). Effect of BaO and SiO_2 addition on PTCR $BaTiO_3$ ceramics. *Journal of Materials science, 34*(18), 4439-4445.

Liu, D. D., & Sampson, M. J. (2012). Some aspects of the failure mechanisms in $BaTiO_3$-Based multilayer ceramic capacitors.

Liu, D. D. (2015). Insulation resistance degradation in Ni–$BaTiO_3$ multilayer ceramic capacitors. IEEE Transactions on Components, *Packaging and Manufacturing Technology*, 5(1), 40-48.

Luo, Y., Pu, Y., Zhang, P., Zhao, J., Wu, Y., & Liu, Y. (2016). Study on Dielectric Properties of SiO_2-doped $BaTiO_3$ Ceramics. *Ferroelectrics, 492*(1), 10-16.

Makovec, D., Samardžija, Z., & Drofenik, M. (2004). Solid solubility of holmium, yttrium, and dysprosium in $BaTiO_3$. *Journal of the American Ceramic Society, 87*(7), 1324-1329.

Futureelectronics.com. (n.d.). Multilayer ceramic capacitor, high voltage ceramic capacitors - Future Electronics. [online] Retrieved from: http://www.futureelectronics.com/en/capacitors/multilayer-ceramic-capacitor.aspx [Accessed 8 Nov. 2017].

N. Nikulin, Fundamentals of electrical materials, Mir Publishers, Moscow, (1988).

Nicker, D. A. (1974). High voltage ceramic capacitors. *Active and Passive Electronic Components*, *1*(2), 113-120.

Okino, Y., Shizuno, H., Kusumi, S., & Kishi, H. (1994). Dielectric properties of rare-earth-oxide-doped $BaTiO_3$ ceramics fired in reducing atmosphere. *Japanese journal of applied physics*, *33*(9S), 5393.

Ösküz, K. E., Torman, M., Sen, S., & Sen, U. (2016). Effect of sintering temperature on dielectric properties of SiO_2 Doped $BaTiO_3$ ceramics. *Materials, Methods & Technologies, 10*, 361-366.

Pan, M. J., & Randall, C. A. (2010). A brief introduction to ceramic capacitors. *IEEE electrical insulation magazine, 26*(3).

Paredes-Olguín, M., Lira-Hernández, I. A., Gomez-Yañez, C., & Espino-Cortes, F. P. (2013). Compensation mechanisms at high temperature in Y-doped $BaTiO_3$. *Physica B: Condensed Matter*, 410, 157-161.

Park, K. J., Kim, C. H., Yoon, Y. J., Song, S. M., Kim, Y. T., & Hur, K. H. (2009). Doping behaviors of dysprosium, yttrium and holmium in $BaTiO_3$ ceramics. *Journal of the European Ceramic Society, 29*(9), 1735-1741.

Paunovic, V., Mitic, V., Marjanovic, M., & Kocic, L. (2016). Dielectric properties of La/Mn codoped barium titanate ceramics. *Facta Universitatis, Series: Electronics and Energetics, 29*(2), 285-296.

Petrović, M. V., Bobić, J. D., Ramoška, T., Banys, J., & Stojanović, B. D. (2011). Electrical properties of lanthanum doped barium titanate ceramics. *Materials characterization*, *62*(10), 1000-1006.

Richerson, D. W. (2005). Modern ceramic engineering: properties, processing, and use in design. CRC press.

Shimada, Y., Utsumi, K., Yonezawa, M., & Takamizawa, H. (1981). Properties of the large-capacitance multilayer ceramic capacitor. *Japanese Journal of Applied Physics*, 20(S4), 143.

Standard, E.I.A. (2002). Ceramic dielectric capacitors classes I, II, III and IV–part I: characteristics and requirements. EIA-198-1-F, November.

Tien, T. Y., & Carlson, W. G. (1963). Influence of oxygen partial pressure on properties of semiconducting barium titanate. *Journal of the American Ceramic Society*, *46*(6), 297-298.

Tsur, Y., Hitomi, A., Scrymgeour, I., & Randall, C. A. (2001a). Site occupancy of rare-earth cations in $BaTiO_3$. *Japanese Journal of Applied Physics*, *40*(1R), 255.

Tsur, Y., Dunbar, T. D., & Randall, C. A. (2001b). Crystal and defect chemistry of rare earth cations in $BaTiO_3$. *Journal of Electroceramics*, *7*(1), 25-34.

Urek, S., Drofenik, M., & Makovec, D. (2000). Sintering and properties of highly donor-doped barium titanate ceramics. *Journal of materials science*, *35*(4), 895-901.

Valdez-Nava, Z., Tenailleau, C., Guillemet-Fritsch, S., El Horr, N., Lebey, T., Dufour, P., ... & Chane-Ching, J. Y. (2011). Structural characterization of dense reduced $BaTiO_3$ and $Ba_{0.95}La_{0.05}TiO_3$ nanoceramics showing colossal dielectric values. *Journal of Physics and Chemistry of solids*, *72*(1), 17-23.

Völtzke, D., Abicht, H. P., Pippel, E., & Woltersdorf, J. (2000). Ca-containing additives in PTC-BaTiO3 ceramics: effects on the microstructural evolution. *Journal of the European Ceramic Society*, *20*(11), 1663-1669.

V'yunov, O. I., Kovalenko, L. L., Belous, A. G., & Belyakov, V. N. (2005). Oxidation of reduced Y-doped semiconducting barium titanate ceramics. *Inorganic materials*, 41(1), 87-93.

Wang, J., Rong, G., Hao, L., Gao, L., Cheng, H., Li, J., & Duan, R. (2016). Dielectric properties of $Ba_{0.97}Bi_{0.02}TiO_3$–$Ba_{1-x}Mg_xSn_{0.02}Ti_{0.98}O_3$ composite ceramics. *Modern Physics Letters B*, *30*(29), 1650363.

Wang, M. J., Yang, H., Zhang, Q. L., Hu, L., Yu, D., Lin, Z. S., & Zhang, Z. S. (2014). Doping behaviors of yttrium, zinc and gallium in $BaTiO_3$ ceramics for AC capacitor application. *Journal of Materials Science: Materials in Electronics*, *25*(7), 2905-2912.

Wang, T., Wang, X. H., Wen, H., & Li, L. T. (2009). Effect of milling process on the core-shell structures and dielectric properties of fine-grained $BaTiO_3$-based X7R ceramic materials. *International Journal of Minerals, Metallurgy and Materials*, *16*(3), 345-348.

Wang, X. H., Chen, R., Gui, Z., & Li, L. (2001). Synthesis and properties of barium titanate based X7R ceramics by chemical method. *Ferroelectrics*, *262*(1), 251-256.

Wu, Y. C., Wang, S. F., McCauley, D. E., Chu, M. S., & Lu, H. Y. (2007). Dielectric Behavior and Second Phases in X7R-Formulated $BaTiO_3$ Sintered in Low-Oxygen Partial Pressures. *Journal of the American Ceramic Society*, *90*(9), 2926-2934.

Yan, Y., Liu, L., Ning, C., Yang, Y., Xia, C., Zou, Y., ... & Liu, G. (2016). Improved electrical properties of SiO_2-added $BaTiO_3$ ceramics by microwave sintering. *Materials Letters*, *165*, 135-138.

Yoon, S. H., Park, Y. S., Hong, J. O., & Sinn, D. S. (2007). Effect of the pyrochlore ($Y_2Ti_2O_7$) phase on the resistance degradation in yttrium-doped $BaTiO_3$ ceramic capacitors. *Journal of Materials Research*, *22*(9), 2539-2543.

Yoon, S. H., Kang, S. H., Kwon, S. H., & Hur, K. H. (2010). Resistance degradation behavior of Ca-doped $BaTiO_3$. *Journal of Materials Research*, *25*(11), 2135-2142.

Zhang, J., Hou, Y., Zheng, M., Jia, W., Zhu, M., & Yan, H. (2016). The occupation behavior of Y_2O_3 and its effect on the microstructure and electric properties in X7R dielectrics. *Journal of the American Ceramic Society*, 99(4), 1375-1382.

Zhi, J., Chen, A., Zhi, Y., Vilarinho, P. M., & Baptista, J. L. (1999). Incorporation of yttrium in barium titanate ceramics. *Journal of the American Ceramic Society*, 82(5), 1345-1348.

Zhu, X. N., Zhang, W., & Chen, X. M. (2013). Enhanced dielectric and ferroelectric characteristics in Ca-modified $BaTiO_3$ ceramics. *Aip Advances*, *3*(8), 082125.

Chapter 2

Introduction

In this chapter we present the different analytic techniques used for the characterization of samples as well as the experimental set-up performed throughout this work. To start the characterization of multilayer ceramic capacitors will be presented and then the preparation and characterization of the Y_2O_3-doped $BaTiO_3$ powders and ceramics.

2.1. Electrical characterization of multilayer ceramic capacitors

2.1.1. Multilayer ceramic capacitors (MLCCs) samples description

Multilayer ceramic capacitors (MLCCs) of the X7R type (Fig. 2.1) were provided by KEMET de México. In this work we counted with three different groups of samples, denominated: A, B, and C. The differences of these groups of MLCCs lie in the composition of the formulated barium titanate powder used as dielectric ceramic material of each one.

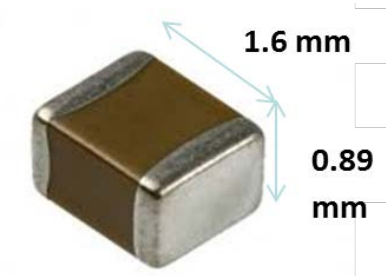

Figure 2.1. *X7R MLCC*

2.1.2. Electrical characterization tests

Multilayer ceramic capacitor samples were subjected to life tests to accomplish their characterization with the determination of life parameters.

2.3.2.1. High Accelerated Life Test (HALT) protocol for individual I-V measurements

To set up the right conditions to perform adequately a HALT in house, it was necessary to know the behavior of the three groups of capacitors. In this way, measurements of resistance degradation during time, under a fixed high voltage value and different temperatures to cover a broad range that could provide the information required, were performed.

First, an individual sample was tested on probe station (Signatone model S-1060R QuieTemp DC) thermally regulated (hot chuck system 1 °C resolution and can operate at temperatures up to 300 °C). In this case, the contacts with the sample are ensured with needle micromanipulators. A source meter unit (SMU 2410, Keithley, Cleveland, OH, USA) (source voltage from 5 μV to 1100 V; measure voltage from 1 μV to 1100 V) was used to apply the voltage and measure the current and time during the test. This experimental set up is shown in Fig. 2.2.

First, a HALT was performed under industrial standard conditions: 400 V and 140 °C for 24 h. A fast rise in the current, which means a decrease in the resistivity to be near zero, indicated the moment when the dielectric breakdown of the capacitor occurred. In this work, the test was stopped when 24 h had passed without failure or at the moment that a breakdown was observed. Additionally, HALT were conducted under the same voltage value but using different temperatures to observe the behavior at higher and lower than 140 °C values.

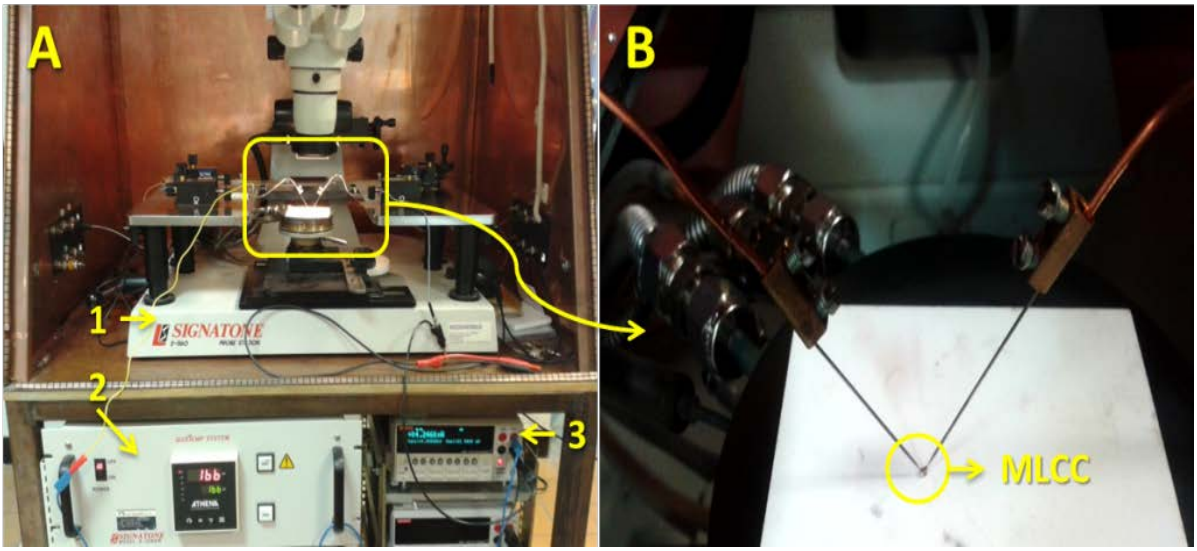

Figure 2.2. *(A) Experimental set-up: (1) probe station Signatone S-1160; (2) heating chuck, Signatone model S-1060R; (3) sourcemeter unit Keithley 2410. (B) Enlarged view of the MLCC under test.*

2.3.2.2. High Accelerated Life Test (HALT) protocol

Three groups of MLCCs of the X7R type were tested under a high accelerated life test (HALT). Measurements of time-to-failure (TTF) of each group of samples were performed under a given set of stress conditions (Table 2.1). The HALT protocol combined two values of voltages and for each one a broad range of temperatures. In this way, it was possible to determine an activation energy linked to the failures for each group of stresses.

For each test, at least 12 pieces of capacitors were subjected to electrical and thermal stress; both parameters (voltage and temperature) were kept constant during the experiment. When it was observed that the ensemble or majority of samples had failed, the test was stopped and data of the evolution of the current with the time were taken to determine the time-to-failure (TTF) of the samples for each combined stress conditions.

Table 2.1. *HALT parameters for the three groups of MLCCs.*

MLCCs group	Voltage (V)	Range of temperature (°C)
A	400	140 – 250
	600	120 – 220
B	400	110 – 225
	600	90 – 200
C	400	20 – 90
	600	20 - 80

2.3.2.4. In-house device for HALT measurements with multiple samples

With the purpose of testing multiple samples while controlling the experimental conditions, a second setup was developed and built in-house (Fig. 2.3). A voltage source (1 kV–10 mA) (MPS1P10/24, Spellman, Hauppauge, NY, USA) (Fig. 2.3A) was connected to a parallel array (Fig. 2.3B) of capacitors placed inside a thermally stabilized hotplate (Fig. 2.3C), and the temperature was measured with a thermocouple and kept at a uniform value (Fig. 2.3D).

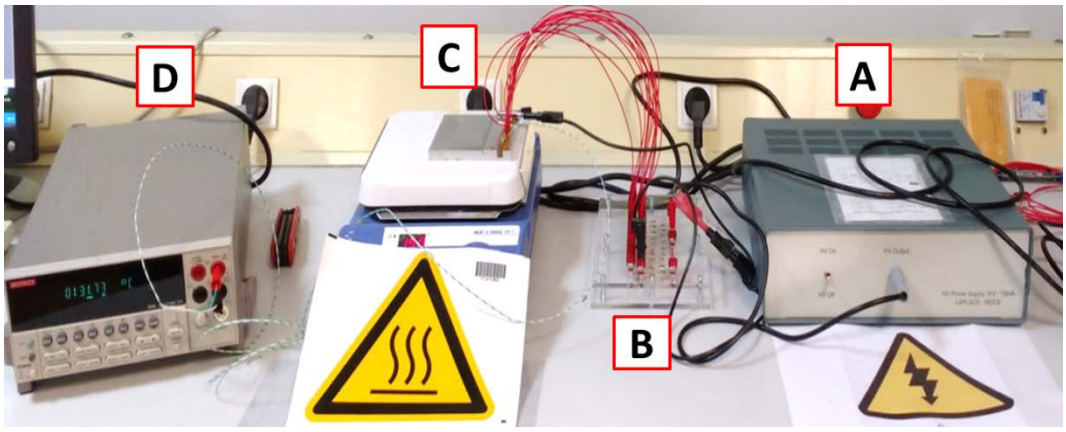

Figure 2.3. *System for perform HALT over multiple samples at once. (A) HV power supplier (1 kV – 10 mA). (B) Plate with protective resistors in parallel to connect the samples that are inside (C) a metallic cell placed over a heating plate which temperature is monitored with (D) a multimeter reading the measurements of a thermocouple (K type).*

The setting up of the samples for the test performance includes the details shown in Fig. 2.4. To maintain the voltage after a capacitor failed, the protective resistors (MS176-5 μΩ, Caddock Electronics Inc.) were joined (Fig. 2.4.a) and considering the total current that the dc supply could deliver (1 mA), the system had a maximum capacity of 20 samples. To connect the samples (Fig. 2.4.b-1) and avoid welding, they were placed inside a capillary glass (Fig. 2.4.b-2) and pressed with a spring test probe (RS Pro 1.27mm Pitch Spring Test Probe with Point Tip) (Fig. 2.4.b-3), which ensured both the electrical contact and the mechanical support of the sample. The glass tubes with the samples and springs were placed inside an aluminum block to maintain thermal homogeneity (Fig. 2.4.c-d). The aluminum block also served as the electrical ground. The heating plate temperature was fixed and measured with a thermocouple (K-type), which was inserted inside a glass tube in the aluminum block. The temperature was always kept below 280 °C, which takes into account the melting temperature (296–300 °C) of the solder material used to assemble the springs with the connecting cables. When the set-up was ready (Fig. 2.5) and the desired temperature reached, the electrical stress was applied.

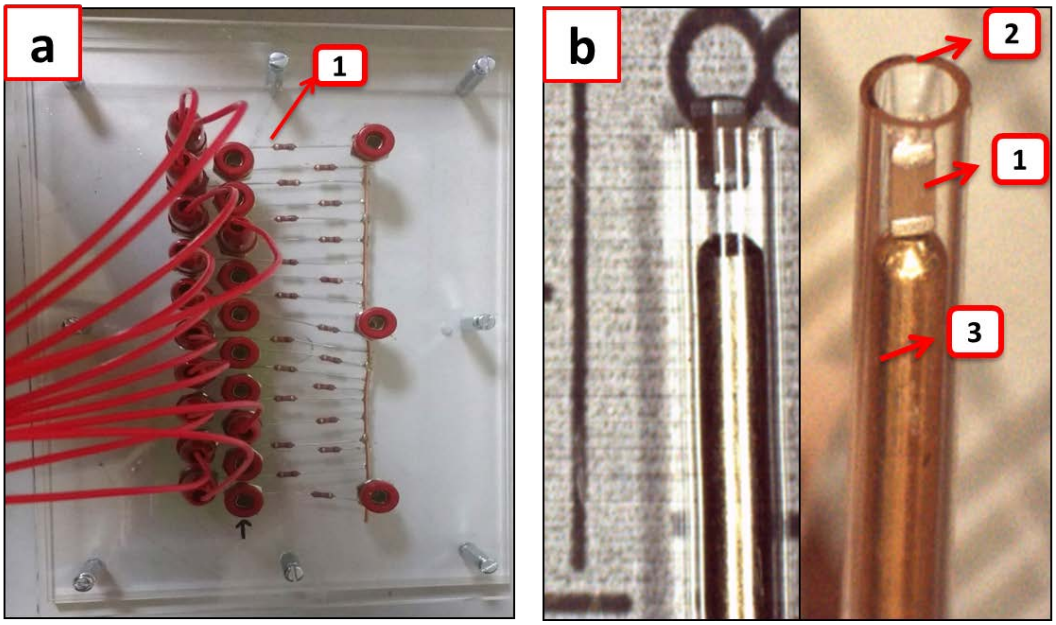

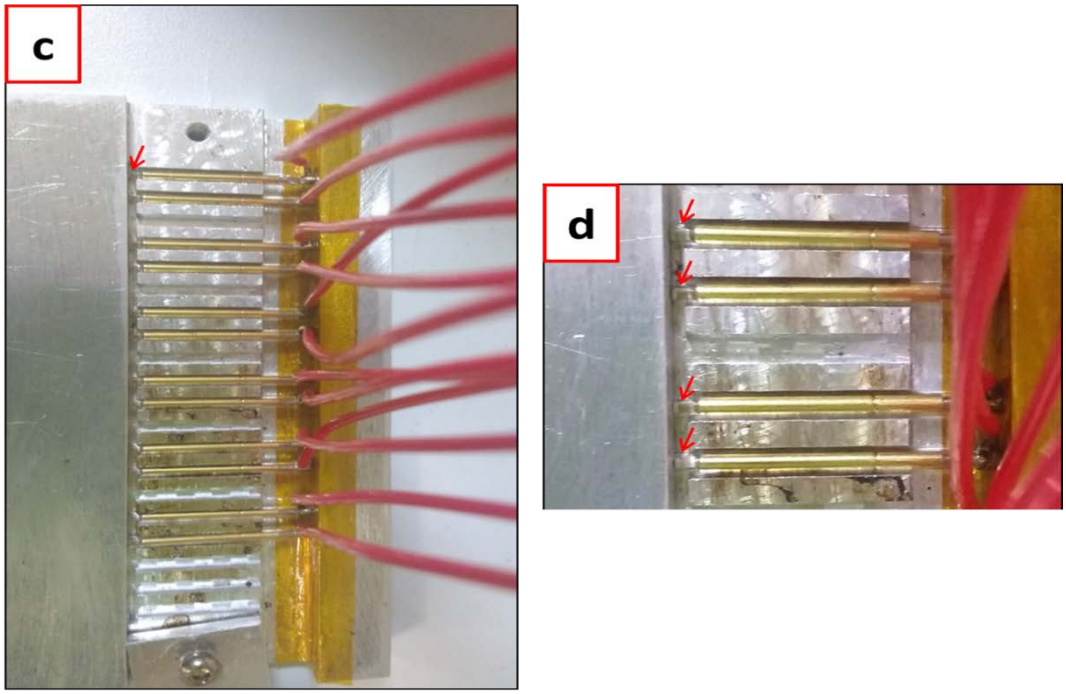

Figure 2.4. *(a) Plate with the protective resistors (1) connected in series with each sample; (b) View of an MLCC (1) inside the glass capillary (2) together with a spring (3); (c) View of the assembled connections (cables + springs) together with the MLCCs in the metallic plate interior canals; (d) Enlarged view of the interior of the cell, where red arrows highlight the samples inside of a glass capillary.*

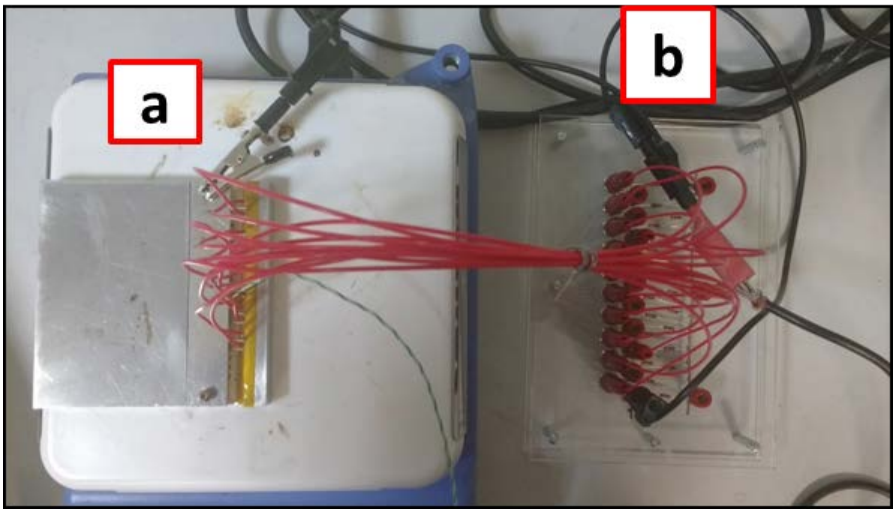

Figure 2.5. *Upper view of the set-up.* ***a.*** *Metallic cell closed (with the samples inside) above the heating plate.* ***b.*** *Plate with protective resistors.*

The capacitors are connected in parallel to a voltage source. If they are working right, the current will not pass through them; otherwise they will become conductive leading to a decrease of the resistance, reflected in a current rising. The data acquired from each HALT experiment was followed in real time with the software, being possible to know the current value in function of the time. Thus, it was possible to know when one or more samples simultaneously, had suffered a breakdown each time the current value increased. This can be seen in the Fig. 2.6, where each step is a rise of the current corresponding to an electrical broken sample. The value of that increment depends on the imposed voltage as well as the resistance value of the protective resistors. This value is constant per failed sample. In the example taken for the Fig. 2.6, under the experimental conditions shown for Fig. 2.6.A, it is 0.6 mA because the applied voltage was 600 V; while in the second case shown in Fig. 2.6.B it is 0.4 mA because the applied voltage was 400 V. When more than one sample fails at the same time, the step will correspond to the mentioned rising of current value multiplied by the number of failed samples. An example of this case is shown enclosed in a green box in the Fig. 2.6.A, the failures 6 and 7 occurred simultaneously, thus that step is equivalent to 1.2 mA and the time to failure was considered two times at the moment to analyze the data. In the plots presented in Fig. 2.6, each failure is signaled with an “F” letter and a number, also the initial and final current values are presented. These values, as explained, are determined based on the failed samples. To assure the circuit was correctly functioning, a short circuit connection was always incorporated to the system, so it was observable that the current was flowing through it and this is why the initial value of the current is not zero.

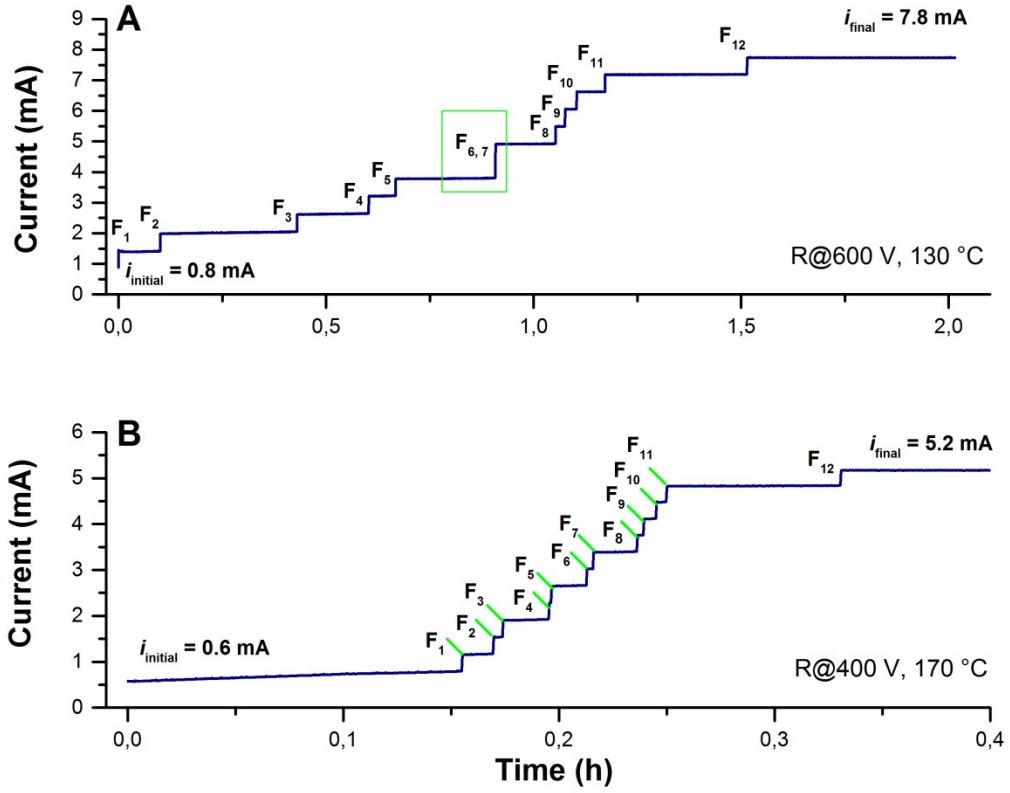

Figure 2.6. *Representation of the data acquired in a HALT experiment.* ***(A)*** *Insulation resistance measurements at 600 V and 130 °C.* ***(B)*** *Insulation resistance measurements at 400 V and 170 °C.*

2.1. Powders characterization

The barium titanate powders used as the dielectric in the production of the Group B and C MLCCs are the same that were utilized in this work for the fabrication of the ceramics described subsequently in this chapter. These ceramics will be denominated as BT-B and BT-C, respectively. It is important to remark that BT-A powder was not used in any case to fabricate MLCCs, as well as that the base-powder of the MLCCs – Group A, was not used for this part of the work.

2.1.1. X-Ray Diffraction

The determination of the crystalline structure and phase were achieved using non-destructive analytical X-ray diffraction (XRD) analyses. This method is based on constructive interference of monochromatic X-rays and a crystalline sample. The X-rays are generated by a cathode ray tube; then they are passed through three basic steps: filtered to produce a monochromatic radiation, concentrated by collimation, and directed toward the sample. The interaction given between the sample and the incident rays produces constructive interference (and a diffractive ray) when conditions satisfy Bragg´s Law (H. Bragg, & L. Bragg, 1913):

$$n\lambda = 2d \sin\theta \qquad (5)$$

Where λ is the wavelength of the electromagnetic radiation to the diffraction angle and the lattice spacing in a crystalline sample, d is the distance between different plane of atoms in the crystal lattice, and θ is the angle of diffraction. The X-rays are then detected, processed and counted, generating a diffraction pattern that can be considered as a “fingerprint” of the material. It provides information about the crystalline phase(s) present in the sample.

In this work, X-ray analyses were performed using a Bruker D4 Endeavor diffractometer shown in Fig. 2.7. Powders and ceramics were deposited on a circular sample holder in poly-(methyl methacrylate) (PMMA). The diffraction patterns were recorded in 2θ mode from 10 to 100º with a 0.02º (2θ) step scan, the acquisition time of 21.7 s in steps and an opening angle fixed slot equal to 1º. Copper anode was used as an X-ray source emitter by using a generator (40 kV, 40 mA) with the corresponding Kα radiations ($\lambda_{K\alpha1}$ = 0.15406 nm and $\lambda_{K\alpha2}$ = 0.15444 nm). The analysis of the obtained diffraction patterns was executed using EVA software, and the JCPDS crystallographic database to identify the phases present in the sample.

Figure 2.7. *X-ray Diffractometer Bruker D4 Endeavor.*

2.1.2. Induced coupled plasma atomic emission spectroscopy

This analytical technique was used for the determination of the chemical elements composition of the different starting powders. The inductively coupled plasma atomic emission spectroscopy (ICP-AES) is a technique that exploits the fact that excited electrons emit energy at a given wavelength as they return to ground state. The fundamental characteristic of this process is that each element emits energy at specific wavelengths peculiar to its chemical character. Although each element emits energy at multiple wavelengths, in the ICP-AES technique it is most common to select a single wavelength (or a very few) for a given element. The intensity of the energy emitted at the chosen wavelength is proportional to the amount (concentration) of that element in the analyzed sample (Thomson, 2012). With the determined wavelengths that are emitted by the sample and by determining their intensities, the analyst can quantify the elemental composition of the given sample relative to a reference standard. The ICP-AES analyses for this work were executed by Marion Technologies.

2.1.3. Scanning electron microscopy

The SEM analyses were performed using a scanning electron microscope JEOL JSM-6510LV. The electron bombardment was carried out to an acceleration voltage from 0.5 kV to 30 kV. The images were obtained at 20 kV.

The samples, either powders or ceramics, were fixed over the sample holder using a graphene adhesive, and then covered with a thin layer of silver. The surface and grain morphologies were observed by this technique. Frequency counts of particles and grain sizes were performed by the analysis of several SEM micrographies with the Image J software. Gaussian distribution was applied to determine the mean size and standard deviation of the samples.

2.2. Manufacture and characterization of ceramics

2.2.1. Raw materials description

Two types of barium titanate (BT) powders were used for doping them with Y_2O_3. In the first place a reagent-grade BT (Ferro Electronic Materials INC) without additives. Then, two BT powders commercially formulated for its application as the dielectric ceramic material of X7R MLCCs. The composition of the three BT powders is shown in Table 2.2, it was determined by an inductively coupled plasma atomic emission spectroscopy (ICP-AES) analysis (performed at Marion Technologies). From these analyses it is worth to highlight the fact that the formulated powders already contain 1.05 wt% of Y_2O_3, which is one of the most common additives for BT dielectric ceramic powder and the one chosen in this work for the doping experiments.

Table 2.2. *Chemical composition of $BaTiO_3$ powders.*

	Ba	**Ti**	**Y**	**Ca**	**Sr**	**Si**	**Mn**	**Mg**	**Co**
BT_A* **Ba/Ti = 2.88**	57.55	19.96	<0.01	0.006	0.04	<0.01	<0.001	0.001	<0.01
BT_B** **Ba/Ti = 2.85**	54.67	19.17	1.05	1.34	0.09	0.30	0.05	0.29	0.012
BT_C** **Ba/Ti = 2.86**	53.86	18.85	1.05	0.57	0.09	0.17	0.05	0.006	0.017

Values are given in wt%. *: BT reagent grade (pure). **: BT commercially formulated.

The powders were also analyzed by X-ray diffraction obtaining the diffraction patterns shown in Fig. 2.8. Even though the three powders have a tetragonal structure (JCPDS: 89-1428), the definition of the peaks is better for the BT-B and BT-C powders, that correspond to the commercially formulated for its industrial application. This is due to the presence of the additives, whose interaction with the BT matrix enhances the intensity between the peaks, as seen for the (002) and (200) planes (Kim et al., 2008).

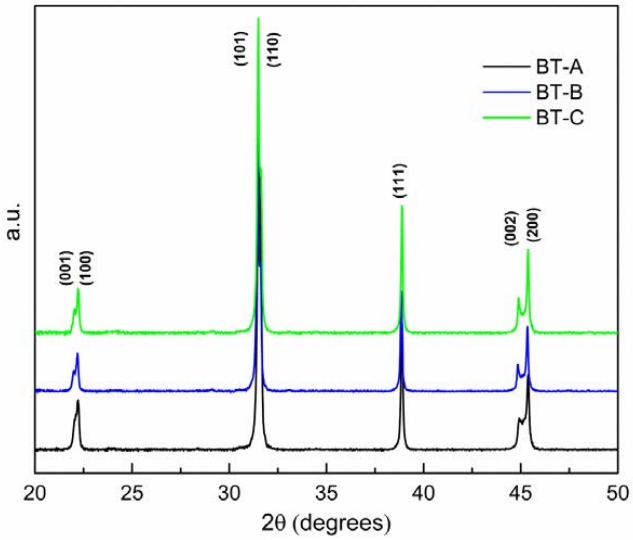

Figure 2.8. *XRD patterns of $BaTiO_3$ starting powders. JCPDS: 89-1428.*

SEM images from BT-A and BT-B were obtained and can be observed in Fig. 2.9. Both powders present similar particles morphology and their sizes are in a close range.

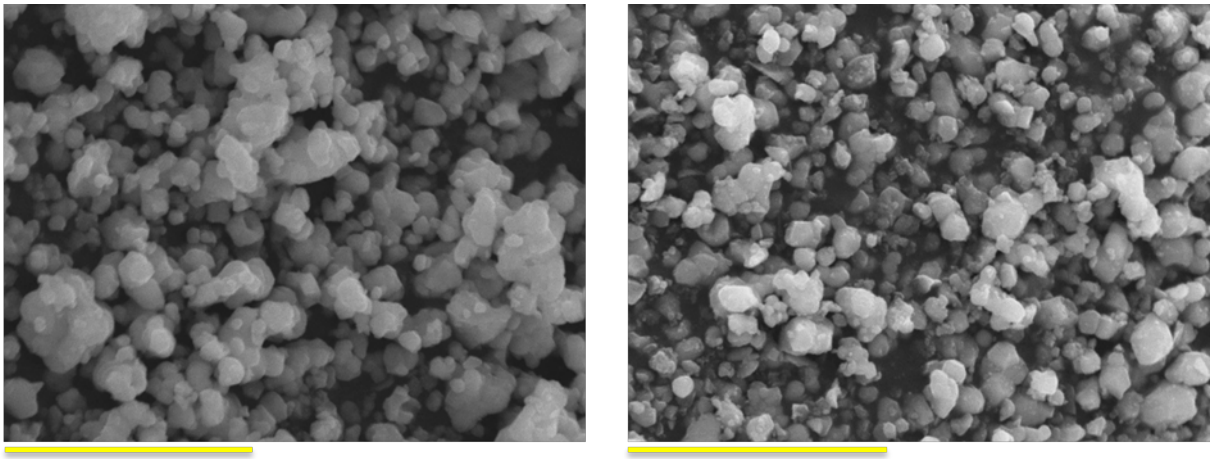

Figure 2.9. *SEM images of (a) BT-A and (b) BT-B powders. Particles size: BT-A: 0.48 – 1.25 µm; BT-B: 0.46 – 0.81 µm. Scale bar: 5 µm.*

2.2.2. Powders doping procedure

Barium titanate (BT) powders (composition shown in Table 2.1) were mixed with the appropriate amount of Y_2O_3 to achieve the corresponding doping concentrations presented in Table 2.2. The raw materials were mixed by traditional solid-state reaction. Powders were ball-milled in a polyurethane mill bottle with yttrium-stabilized zirconia balls, using ethanol as the grinding media for 4 h. Doped powders were dried and 1 wt% of polyvinyl butyral (PVB) was added as binder. Finally, this mixture was grinded and sieved obtaining the desired powder.

Table 2.3. *Sample identification of prepared powders doped with Y_2O_3.*

Composition (wt% Y_2O_3)→ Type of powder↓	0	1.0	1.5	2.0	2.5	5.0	20.0
BT-A*	BT-A_0	BT-A_1	BT-A_1.5	BT-A_2	BT-A_2.5	BT-A_5	BT-A_20
BT-B**	------	BT-B_1	BT-B_1.5	BT-B_2	BT-B_2.5	BT-B_5	BT-B_20
BT-C**	------	BT-C_1	BT-C_1.5	BT-C_2	------	------	------

*: BT reagent grade (pure). **: BT commercially formulated.

2.2.3. Green ceramics manufacturing

Ceramics were obtained from the powders previously prepared. The powders were compacted with a manual hydraulic press (Specac) using uniaxial pressure to compact the powders in a pressing die as shown in Fig. 2.10. Cylindrical pellets (diameter: 8 mm, thickness: 1.7 mm) were produced applying a uniaxial pressure of 300 MPa for 30 s. The mass and dimensions of each compact disk were measured before and after the sintering to determine the density value. The density values of the ceramics are reported based on the theoretical density of 6.02 g/cm^3, reported of the barium titanate.

Figure 2.10. *Manual hydraulic press and pressing die during the making of green ceramics.*

2.2.4. Ceramics sintering

The term sintering refers to the thermal treatment that allows the bonding of particles into a more consistent solid structure. The two principal phenomena included in sintering process are the reduction of the porosity (densification) and the grain growth. This happens by mechanisms of mass transport that often occurs on the atomic scale. From the thermodynamic point of view the sintering is driven by a reduction of the surface energy (Coble, 1961; German, 2014).

In this work, different sintering programs were used for the conducted experiments. One sintering program was performed using a laboratory chamber furnace with fiber insulation (model LF, Nabertherm). Pellets were placed over a platinum cover inside an alumina container. The thermal cycle was a two-steps program: samples were first heated to a higher temperature aiming to promote an intermediate densification, then the temperature was reduced, and a lower temperature value was held to complete the densification. This strategy has been reported to present advantages such as a uniform pore microstructure while controlling grain growth and enhancing densification (Chen & Wang, 2000; Polotai, Breece, Dickey, Randall, & Ragulya, 2005; X. Wang et al., 2006). The thermal program followed for the production of undoped and doped BT ceramics under air is shown in the Fig. 2.11. The thermal cycle was carried out from room temperature until 1350 °C (no holding time) with a heating rate of 10 °C/min, then a cooling rate of 30 °C/min was applied till reach a sintering temperature of 1150 °C that was held for 15 h; finally, a cooling rate of 150 °C/h was used in the final stage. This two-step sintering program was used to obtain undoped and 2.5 and 5 wt % Y_2O_3-doped ceramics issued from BT-A and BT-B powders.

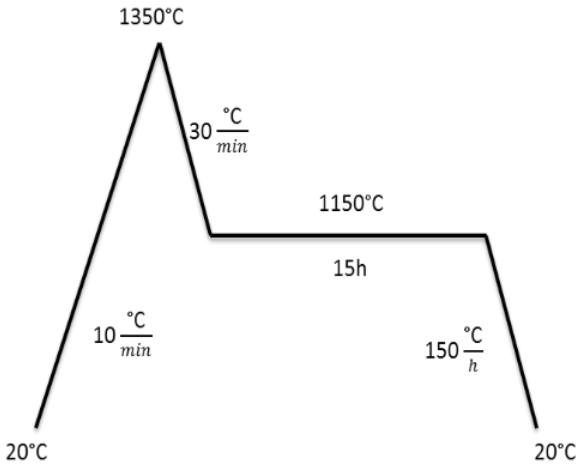

Figure 2.11. *Sintering program A: Two-steps sintering program in air. (BT-A and BT-B ceramics undoped and with 2.5 and 5 wt% of Y_2O_3).*

On the other hand, it was also performed a sintering process carried out at a company (KEMET de México). This sintering process was used aiming to mimic the industrial production conditions for the X7R-MLCCs. The thermal program and conditions are shown in Fig. 2.12; samples are fired in a kiln with reducing atmosphere and a temperature of 1310 °C hold for 3 h, then samples are taken out and passed to a kiln for a post-sintering treatment with an oxidizing atmosphere (used to restore the characteristics of the dielectric). In this case, due to the nature of the process, two set of samples were derived from each lot of processed ceramics. Each group was divided taking the half of the ceramics just after the firing under reducing atmosphere and the rest of them were passed through the re-oxidizing step.

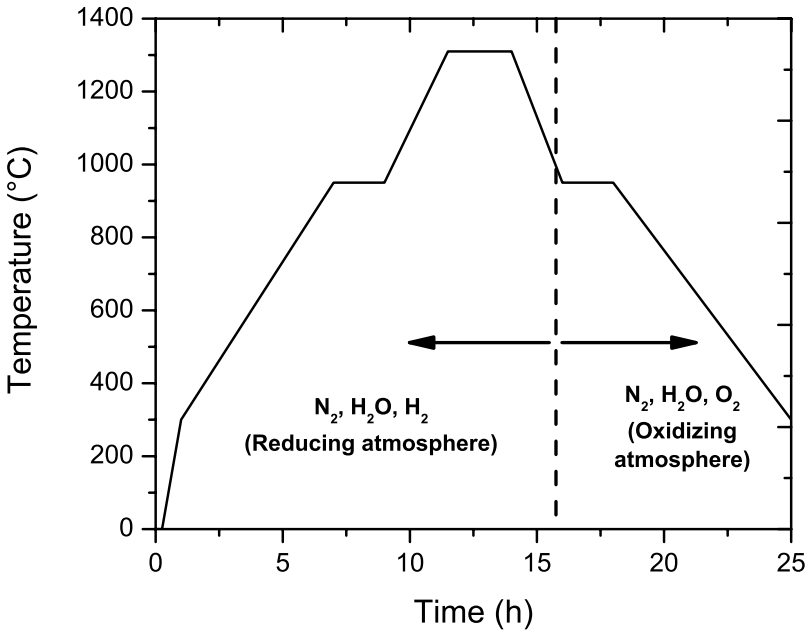

Figure 2.12. *Representation of the sintering program at industrial level.*

2.2.5. Thermal treatment of powders

Aiming to observe the behavior of the samples as powders, the doped ones with the higher Y_2O_3 content were subjected to a thermal program in air. BT-A and BT-B powders undoped and Y_2O_3-doped with 2.5, 5 and 20 wt%, were thermally treated in air under 1310 °C for 3h. This process was performed in a laboratory chamber furnace using the program observed in Fig 2.13.

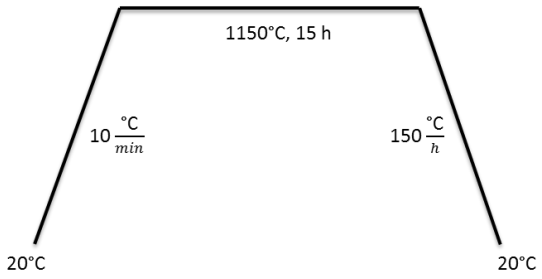

Figure 2.13. *Thermal program for powders treated in air.*

References

Bragg, W. H., & Bragg, W. L. (1913). The reflection of X-rays by crystals. *Proceedings of the Royal Society of London. Series A, Containing Papers of a Mathematical and Physical Character, 88*(605), 428-438.

Chen, I. W., & Wang, X. H. (2000). Sintering dense nanocrystalline ceramics without final-stage grain growth. *Nature, 404*(6774), 168-171.

Coble, R. L. (1961). Sintering crystalline solids. I. Intermediate and final state diffusion models. *Journal of applied physics, 32*(5), 787-792.

German, R. (2014). *Sintering: from empirical observations to scientific principles*. Butterworth-Heinemann.

Kim, C. H., Park, K. J., Yoon, Y. J., Hong, M. H., Hong, J. O., & Hur, K. H. (2008). Role of yttrium and magnesium in the formation of core-shell structure of $BaTiO_3$ grains in MLCC. *Journal of the European Ceramic Society, 28*(6), 1213-1219.

Polotai, A., Breece, K., Dickey, E., Randall, C., & Ragulya, A. (2005). A novel approach to sintering nanocrystalline barium titanate ceramics. *Journal of the American Ceramic Society, 88*(11), 3008-3012.

Thompson, M. (2012). *Handbook of inductively coupled plasma spectrometry*. Springer Science & Business Media.

Wang, X. H., Deng, X. Y., Bai, H. L., Zhou, H., Qu, W. G., Li, L. T., & Chen, I. W. (2006). Two-Step Sintering of Ceramics with Constant Grain-Size, II: BaTiO3 and Ni–Cu–Zn Ferrite. *Journal of the American Ceramic Society, 89*(2), 438-443.

Chapter 3: Electrical characterization of MLCCs

Introduction

Multilayer ceramic capacitors (MLCCs) are one of the most important electric components used in most of the electronics areas. MLCCs present an economical volumetric efficiency for capacitance and high reliability (Wang et al., 2012). They are characterized by a high dielectric constant and thinner dielectric layers (Jain, Fung, Hsiao, & Chan, 2010). The global production of these pieces has abruptly increased with the growing of the electronic market. They are mainly demanded for its use in consumer products (notebook computers, mobile phones, digital cameras), as well as in military products (aerospace, aviation, ships, weapons) and industrial products (equipment of communication, medical electronics, automotive electronics, oil exploration) (Fantozzi, Niepce, & Bonnefont, 2013; J. Yoon, K. Lee, & S. Lee, 2009). The global production accounts for about 3 trillion units per year (Foeller, Dean, Reaney, & Sinclair, 2016), and its costs are relatively low being few USD cents per unit. During the design of consumer electronics, it is considered as a reliable component when used within the specifications. MLCCs can be fabricated with a base metal electrode technology (BME), where successive layers of dielectric and electrodes are stacked and sintered to obtain an interdigitated electrode structure. The main dielectric material is based on a ferroelectric barium titanate.

Although $BaTiO_3$ presents electromagnetic properties that make it suitable as base material for the formulation of the dielectric material for MLCCs (Tsur, Dunbar, & Randall, 2001; Wang et al., 2014), it is not by itself adapted for applications since it must follow an industrial process (shaping

and sintering) along with intrinsic properties that show a large variation with temperature. (D. Yoon, & Lee, 2004; J. Yoon et al., 2009).

Capacitors must maintain their properties within a certain tolerance in a wide range of temperatures during its lifetime. Doping remains the strategy to adapt the dielectric properties of the dielectric layer to the target application, especially for broad temperature use under high electric fields. (Ashburn, & Skamser, 2008; Paunović, Živković, Vračar, Mitić, & Miljković, 2004).

Since reliability is a critical parameter in design of electronics, components manufacturers keep track of it through different parameters. Assessment of the reliability can be very accurate trough periodic analysis of products on service and by accounting for failed products, but it is not predictive and takes a long time. Therefore, other methods need to be used to reduce the evaluation time to have an indication of the reliability prior the commercial release of the components. Accelerated test conditions have to be designed to get the most accurate prediction possible of the lifetime of capacitors in service conditions. The most common tests for reliability of MLCCs are the insulation resistance and combined stress measurements, also known as highly accelerated lifetime test (HALT). (Paulsen & Reed, 2001; Vassilious & Mettas, 2001).

Electrical systems such as capacitors may be tested using two types of tests; either constant stress test or progressive stress test can be performed. In the first type, a number of specimens are taken to their breakdown under defined stress conditions, and then the times to failure are measured; in the second type, breakdown voltages may be measured. At the moment of performing the electrical test, whatever the type, for the given conditions each tested sample will produce a different result, so the total of obtained data can be analyzed by a statistical distribution. (Chauvet & Laurent, 1992 June).

Different statistical distribution models could be applied in the data analysis from these tests, including the Weibull, Gumbel and lognormal. The Weibull distribution is widely used in this field,

and is the one used in this work, in which a two-parameter Weibull analysis is performed. (Chauvet & Laurent, 1992 June; Diaham et al., 2010).

When tailoring the properties of MLCCs, besides the initial electrical parameters, it is of great interest to analyze and seek the correlations between basic structural and chemical formulation to the reliability (time-to-failure) of capacitors. Very few studies in the literature address this, understandably because producing MLCC for reliability testing requires at least pilot size facilities to produce many samples with a reproducible process to minimize the influence of other parameters than the one being tested.

Moreover, the aim of the test is over a fixed kind of capacitors since dielectric is formulated to the best possible performance. Hence, conclusions regarding the effect of the doping over the reliability of the MLCC are rather speculative.

Given the numerous and complex interactions between the additives and dopants during and after the sintering process, a simpler approach needs to be undertaken. In this work we determine the time-to-failure of $BaTiO_3$-based X7R MLCC capacitors containing 1.05 %wt yttrium in their formulation.

3.1. High Accelerated Life Tests

The traditional way to evaluate the reliability of MLCCs is performing an accelerated test under a representative number of samples subjected to determined conditions of temperature and voltage with the aim to determine the time to failure using a statistical model. Also, it is possible to determine the failure modes (Liu, 2011). At industrial level this kind of tests are performed under fixed values of temperature and voltage, however they can be carried out using different values covering a broad range of stresses, with the aim to know if the failure mechanism changes depending on the value of those (Scarpulla, 2016).

High Accelerated Life Tests (HALT) have been widely used to evaluate the reliability of electronic devices such as multilayer ceramic capacitors. The principal result of these kinds of tests is the determination of the time-to-failure (TTF) of the MLCCs when they are subjected to life stress conditions much higher than the normal using-level conditions (ambient temperature and rated voltage). The expected or average TTF is known as the mean time to failure (MTTF) which can be taken as a reliability indicator. The high-raised stress conditions are normally high voltages and temperatures that cause an electrical and thermal stress which would be not caused at normal conditions since these devices have a very long expected life (Liu, 2013 March). To evidence the moment when a breakdown occurs, the HALT follows the leakage current or insulation resistance of the MLCCs under the defined stress parameters (J. Yoon et al., 2009). The collection of TTF data from HALTs allows using it for the estimation of an activation energy associated to the electrical degradation mechanism(s) that causes the breakdown (Paulsen & Reed, 2001).

The HALT methodology normally begins by causing the failure of the electronic components, MLCCs in this case, under different combinations of electric and thermal stress. Then a failure distribution can be fitted, and the quantification of the time-to-failure is done. Having this data is then possible to determine the value of the activation energy (E_a) and get an insight of the information about the failure mechanism of the tested samples. As previously mentioned, the objective of preforming a HALT is to obtain the TTF, this value can also be used to predict median life under normal conditions of use. However, it must be used carefully and considering there are different factors beside the stress conditions that can highly influence the median life of an electronic component like ceramic capacitors.

In this study, failure data are fit to a Weibull distribution and the statistic $t_{63.2}$ is chosen as the characteristic time life of the samples. The Weibull parameters are determined and then used in conjunction with an Arrhenius model to find the activation energy related with the failure under determined conditions of the tested groups of MLCCs.

3.1.1. High Accelerated Life Test (HALT) – standard conditions

High accelerated life tests are widely used in the industries that produce ceramic capacitors in order to assure the reliability of its products. The conditions of the HALT are mostly determined by the protocols that have been developed for the different applications capacitors can have. In this way, capacitors can be tested for long periods under different combinations of temperatures and voltages. The testing voltage is given by *n* times the rated voltage (*n*Vr), which is basically a voltage beyond which the capacitor will be operating under unusual conditions. Thus, it was intended to perform a HALT using industrial testing parameters in-house. The main objective of this first experiment was to examine if it is possible to take the results as a criterion to discriminate among the MLCCs groups. The HALT conditions that we will denominate as standard will be a testing period of 24 h applying 140 °C and 8*Vr = 400 V. Thus, resistance evolution was observed during the time lapse of 24 h or until a breakdown was evidenced by a conspicuous decrease of the resistance (Paulsen & Reed, 2001). Samples from three groups (A, B, and C) of MLCCs X7R-type were subjected to the HALT standard conditions (400 V and 140 °C) while following the current evolution under these conditions.

As to the groups A and B, the behaviors of their samples under the standard HALT conditions (400 V and 140 °C) are shown in the Fig. 3.1. In this figure is possible to observe the current evolution of these groups of MLCCs, each one of the “steps” correspond to an increase in the current given by the breakdown of a capacitor, i.e. each step is a failure.

As seen in this figure, the first remarkable observation is the clear shorter time in which the samples from Group B fail. The Group A showed to be affected to a lesser extent by the high voltage and temperature compared to the Group B. While the Group A did not show evidence of breakdown before 24 h, the samples from the Group B failed before this period.

Testing the samples in this way allowed us to observe the clear differences among the three groups with respect to their response when submitted to these stress conditions. The first group that showed a clearly different behavior when standard HALT conditions where applied was the Group C. It was not possible to perform the HALT at standard conditions for Group C samples since they suffered a breakdown immediately when tested at this voltage (400 V) and a temperature above 90 °C, so there is no gathering data for this group under the HALT standard parameters. However, HALT tests for this group were performed using the same electrical stress conditions but lower temperature ranges. They are certainly affected in a higher or less extension by the voltage and temperature imposed. Under these conditions, the MLCC pieces from the Group A are considered a more reliable material, bearing in mind that they did not fail at extreme conditions before 24 h. The Group B is more affected by these stress conditions, presenting higher resistance degradation over the time. Finally, the Group C is the most damaged when subjected to this test since its breakdown was instantaneous under these conditions.

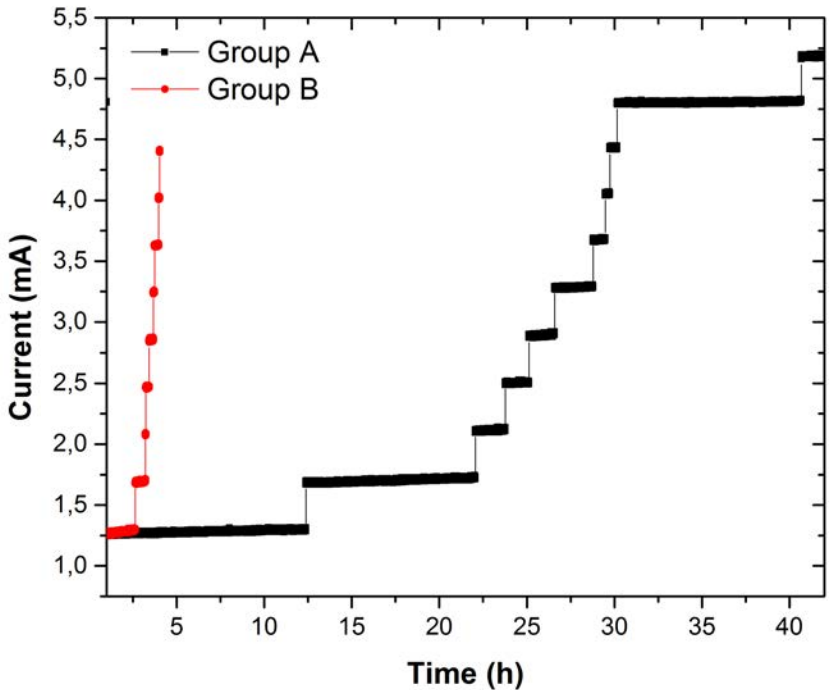

Figure 3.1. *Current evolution of Groups A and B during HALT experiment at standard conditions (400 V, 140 °C).*

From this starting point it was possible to expect that the different behavior among the groups was observed as well at different HALT combination of conditions. To confirm this, the next step was to broad the range of thermal stress.

3.1.2. Impact of temperature on breakdown of MLCCs

For a first attempt, the experiment was carried out testing one sample at time in a Signatone S-1160 probe station. The thermal stress was provided by a hot chuck system and the electrical parameters were controlled and followed by a Keithley's 2410 Source Measure Unit (SMU).

Performing high accelerated life tests in the probe station (one sample per test) allowed to follow the current and resistance evolution of the three groups of samples, when tested at 400 V and different temperatures.

A general overview of the resistance behavior of the three groups, when HALT was performed at 400 V and different temperatures, is shown in the Fig. 3.2. For the three cases, the resistance was rather stable during the beginning of the test and then it started to decrease until a rapid step down that was the signal for a breakdown of the sample.

As is possible to observe in Fig. 3.2, there is a distinct difference in the range of time that the failures of the MLCCs are produced. Even for groups A and B that were tested under the same temperatures, the longer times to failure were seen for Group A (Fig. 3.2.a). Despite the TTF for MLCCs from Group B (Fig. 3.2.b) are in the middle of the ones from Groups A and C, the values are closer to the first. In fact, Group A and B show more similitudes with regard to its behavior under higher stress values; i.e. these groups are possible to test under temperatures above of 100 °C while Group C is not. Regarding the Group C (Fig. 3.2.c) this set of samples was the most affected by the high temperature. The first evidence is that as previously said, the range of testing

temperatures had to be set to a maximum of 80 °C so the failure was not immediate and then the data showed that Group C presents the shorter times to failure of the three groups.

Since the voltage was the same in all the cases (400 V), the effect of the temperature over the resistance degradation is clear; when the thermal stress is higher the time-to-failure is shorter. This is a common effect for the three groups; however, we remind that each group of MLCCs is affected to a greater or lesser extent by the thermal stress.

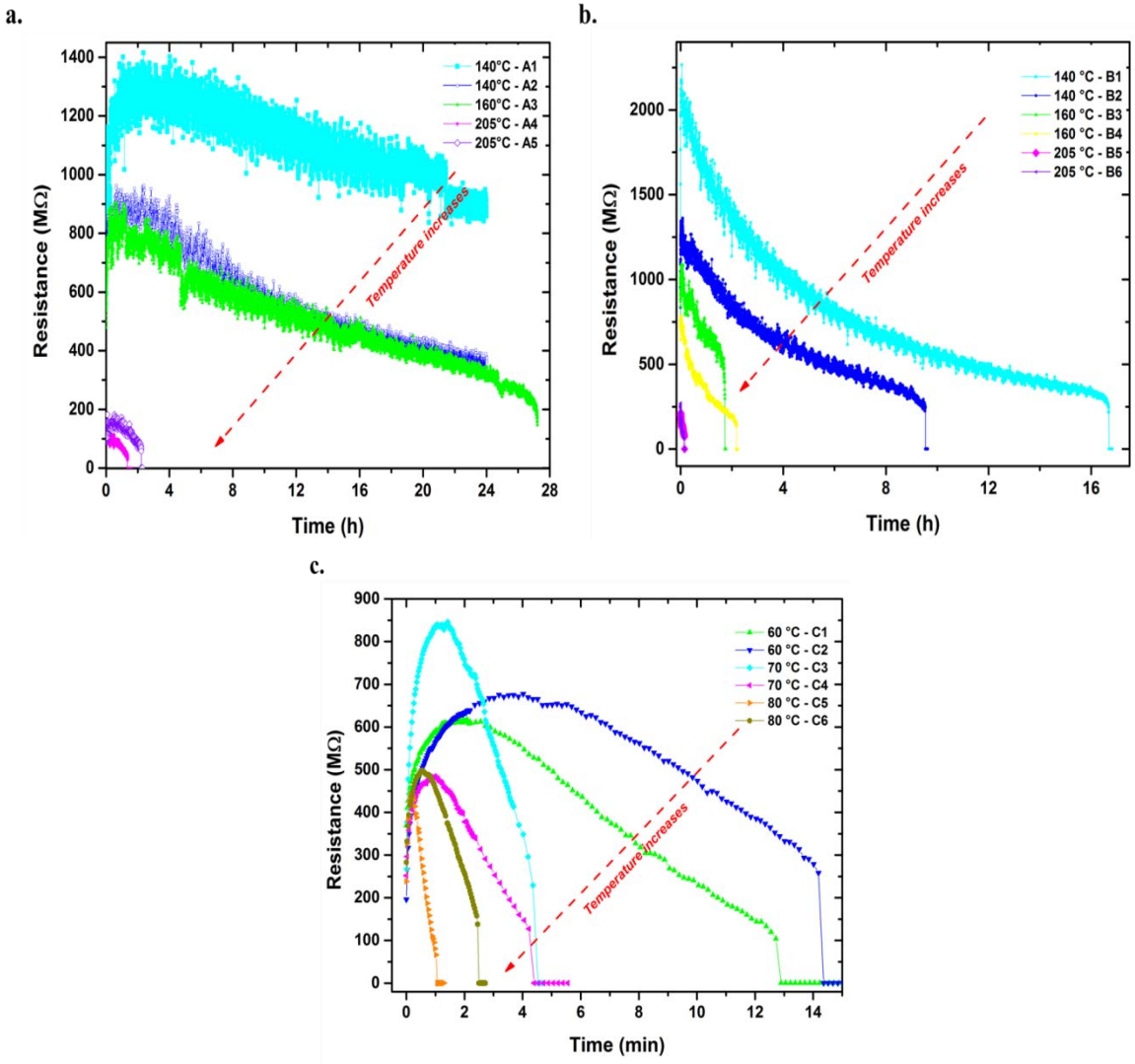

Figure 3.2. *Resistance evolution of individual MLCCs from (**a**) Group A, (**b**) Group B, and (**c**) Group C during HALT performed with 400 V and different temperatures.*

Thus, these experiments allow not only differentiate and even classify the MLCCs groups by their time-to-failure (TTF) but also provide a clear clue of how the thermal stress causes an important effect over the resistance degradation of the samples. Knowing this and considering the tests reproducibility and time to perform them, the next step was to perform the HALT testing multiple samples at once under the same stress conditions. In this way, the performance of a statistical analysis of the TTF will be achieved and a characteristic life time will for each group will be obtained, which will also lead us to obtain an activation energy related with the failure of each sample.

3.1.3. Determination of Time to Failure (TTF) and Mean Time to Failure (MTTF)

The Mean Time to Failure (MTTF) is a value that provides the average life time expected for non-repairable items such as the MLCCs.

To continue with the characterization of the three groups of MLCCs, high accelerated life tests were from then performed in an in-house device that allows testing multiple samples at the same time while controlling the voltage and temperature (Section 2.3.2.4). Aiming to gather enough data to the subsequently statistical analyses, 12 samples of each group were tested under HALT.

Breakdown was assumed to have occurred when an abrupt increase in the current of about 0.4 mA (when testing at 400 V) was detected. The failure times were determined by these increments in current indicating a short circuit. This increase in current is well described in the literature, and often related to the breakdown of the layer of dielectric (Teverovsky, 2012).

The MLCCs groups have very distinct behaviors according the HALT conditions, with the breakdown times ranging from seconds (Group C) to tenths of hours (Group A). The times to failure of samples from Groups A and B when tested under standard HALT conditions are shown in the Fig. 3.3. Samples Group A last longer than the ones from Group B, having a range of TTF from

approximately 22 to 30 hours, while the Group B has a TTF range from about 3 to 4 hours. Despite the early failures, both groups of samples fail with a low dispersion that allows performing HALTs with multiple samples tested at the same time, obtaining accurate data. However, as observed in the parallel plot of the TTF for each detected failure, is possible to say that the Group A under these conditions presented less dispersion, being the majority of the failures around the same value of time.

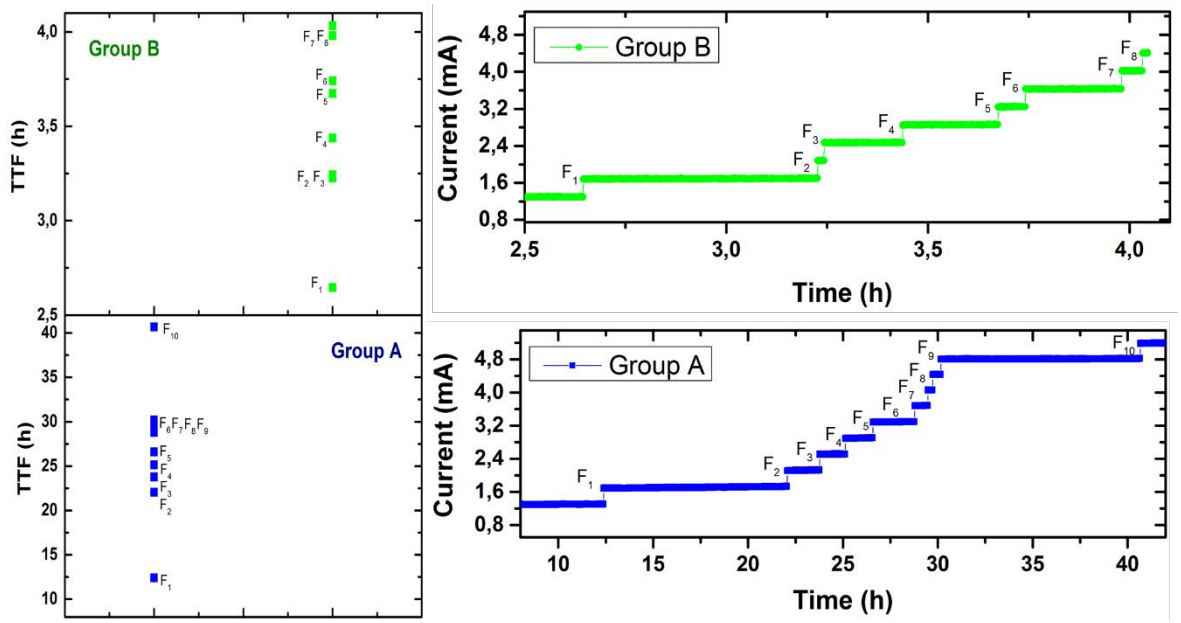

Figure 3.3. *Comparison of the TTF and current evolution for MLCCs from Groups* ***A*** *and* ***B*** *when tested under HALT standard conditions (400 V, 140 °C).*

In the Fig. 3.4 are shown the comparative plots of the obtained times-to-failure for the three groups when tested under a HALT with 400 V and different temperatures. These plots show that under these different conditions, in most of the cases (temperatures) for the three groups, the TTF data have low dispersion. The samples tend to be grouped in a lapse of time, i.e. fail at close times, although there are some samples that are early or late failures. Also, it is obvious that for the three groups the TTF decreases as the temperature increases. A closer insight of dispersion of the TTF in function of the failure sequence for each applied temperature can be seen in the Fig. 3.5.

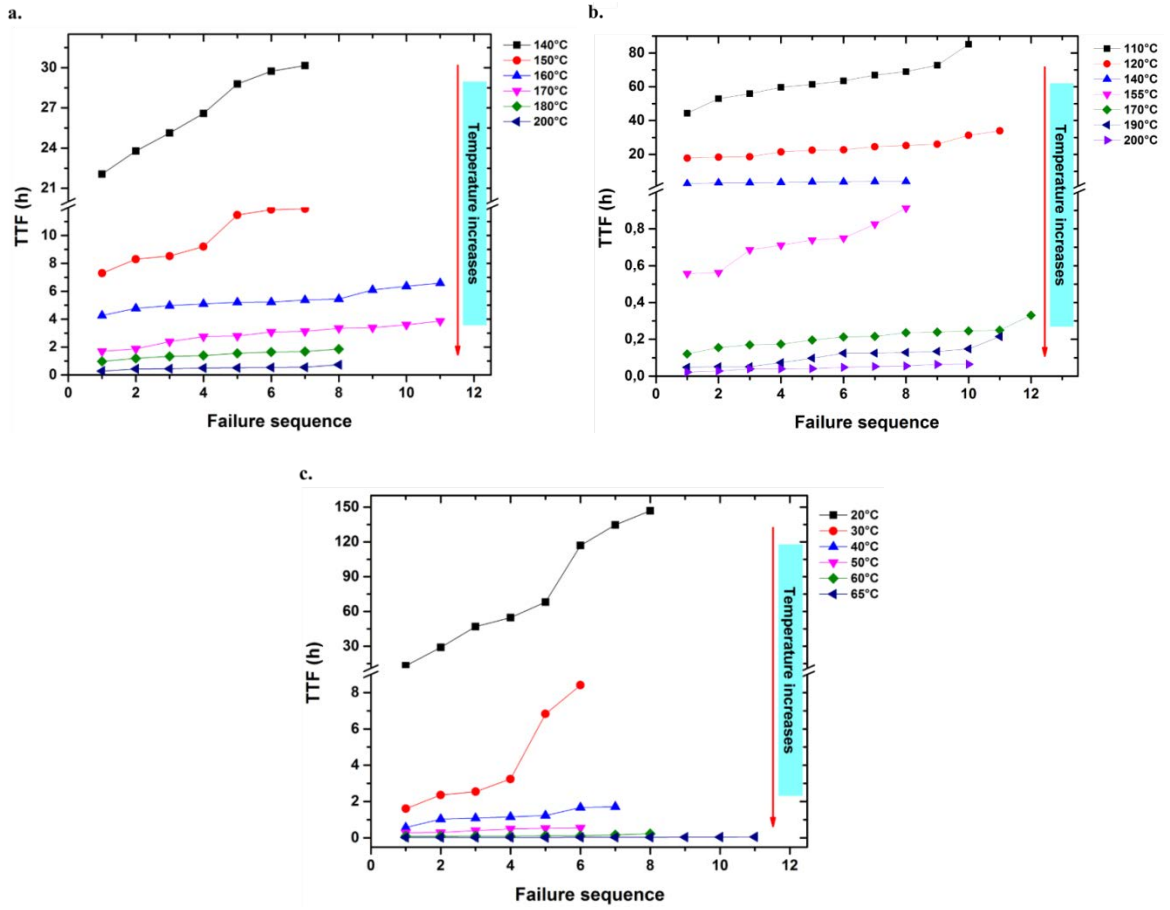

Figure 3.4. *Correlation of the time-to-failure for the failures of each group of MLCCs. HALT conditions: 400 V and temperature indicated on the plots. (**a**) Group A, (**b**) Group B and (**c**) Group C.*

From these figures (Fig. 3.4.) is also observed that the dispersion of TTF decrease at higher values of temperature. This could be related with the failure mechanism and the way it is thermally activated. At low temperatures it is more difficult to overpass the activation energy necessary to start the breakdown phenomenon.

However, these results only provided an insight about the way that thermal stress affects the samples reliability. Considering this, another voltage value was applied while using a thermal stress of about the same range of temperatures, so the effect of electrical stress could also be analyzed.

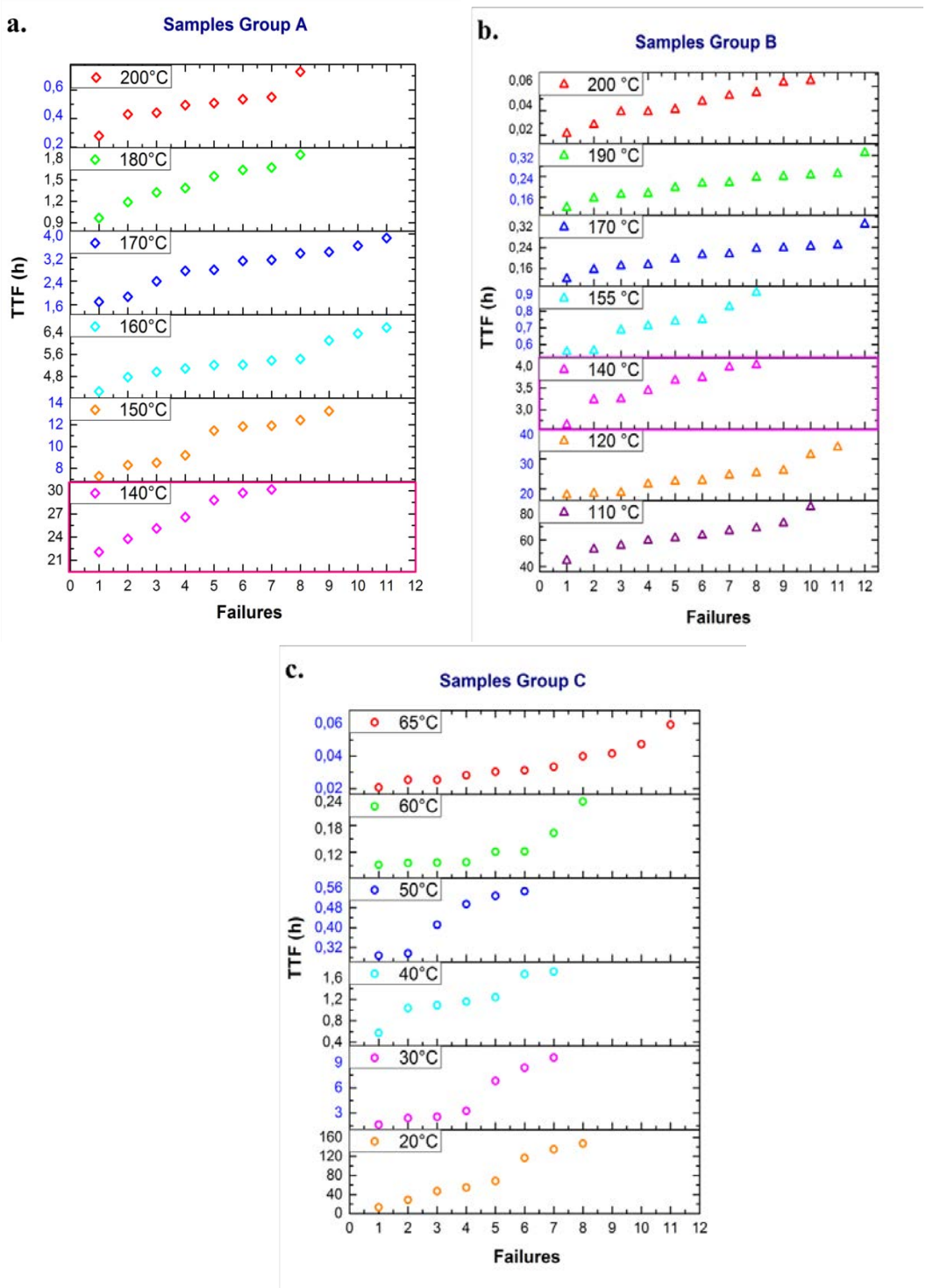

Figure 3.5. *Comparison of the TTF for MLCCs from* ***(a)*** *Group A,* ***(b)*** *Group B, and* ***(c)*** *Group C. HALT conditions: 400 V, temperature indicated on the plots.*

In this way, HALTs were performed with an electric stress of 600 V and the results of the times-to-failure can be seen in the Fig. 3.6. Again, it can be seen the effect of the thermal stress over the TTF

as it decreases while the temperature increases. However, now is possible to compare the Fig. 3.6 and Fig. 3.4 and see that there is also an effect over the TTF exerted by the electrical stress.

Comparing the TTF observed in Fig. 3.6 and Fig. 3.7 against the ones presented in Fig. 3.4 and Fig. 3.5, at the same temperatures but higher voltage, the breakdown of the samples was achieved in shorter times. Taking by example the HALT at 140 °C at both voltages, for samples of Group A and Group B and HALT performed at 60 °C at both voltages for Group C, the TTF is decreased when the higher voltage is applied as shown in Table 3.1.

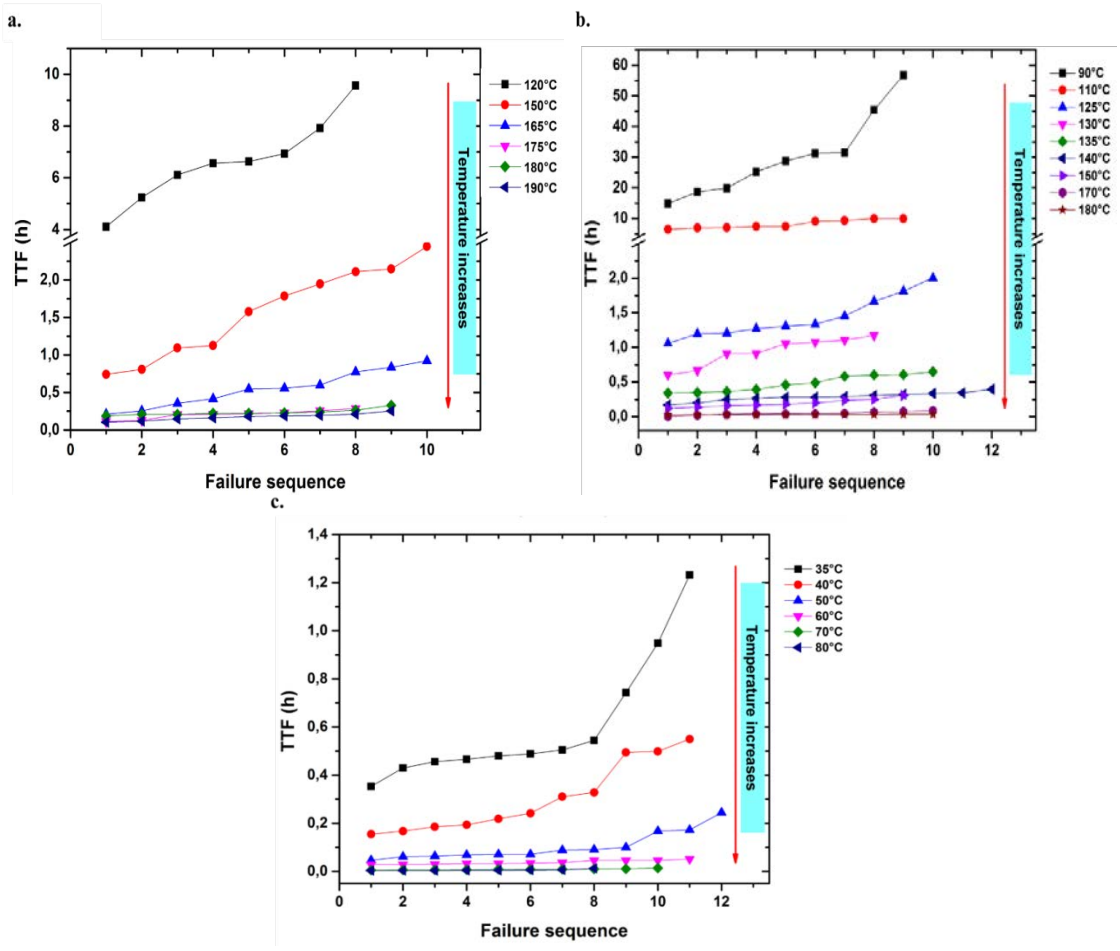

Figure 3.6. *Correlation of the time-to-failure for the failures of each group of MLCCs. HALT conditions: 600 V and temperature indicated on the plots.* ***(a)*** *Group A,* ***(b)*** *Group B and* ***(c)*** *Group C.*

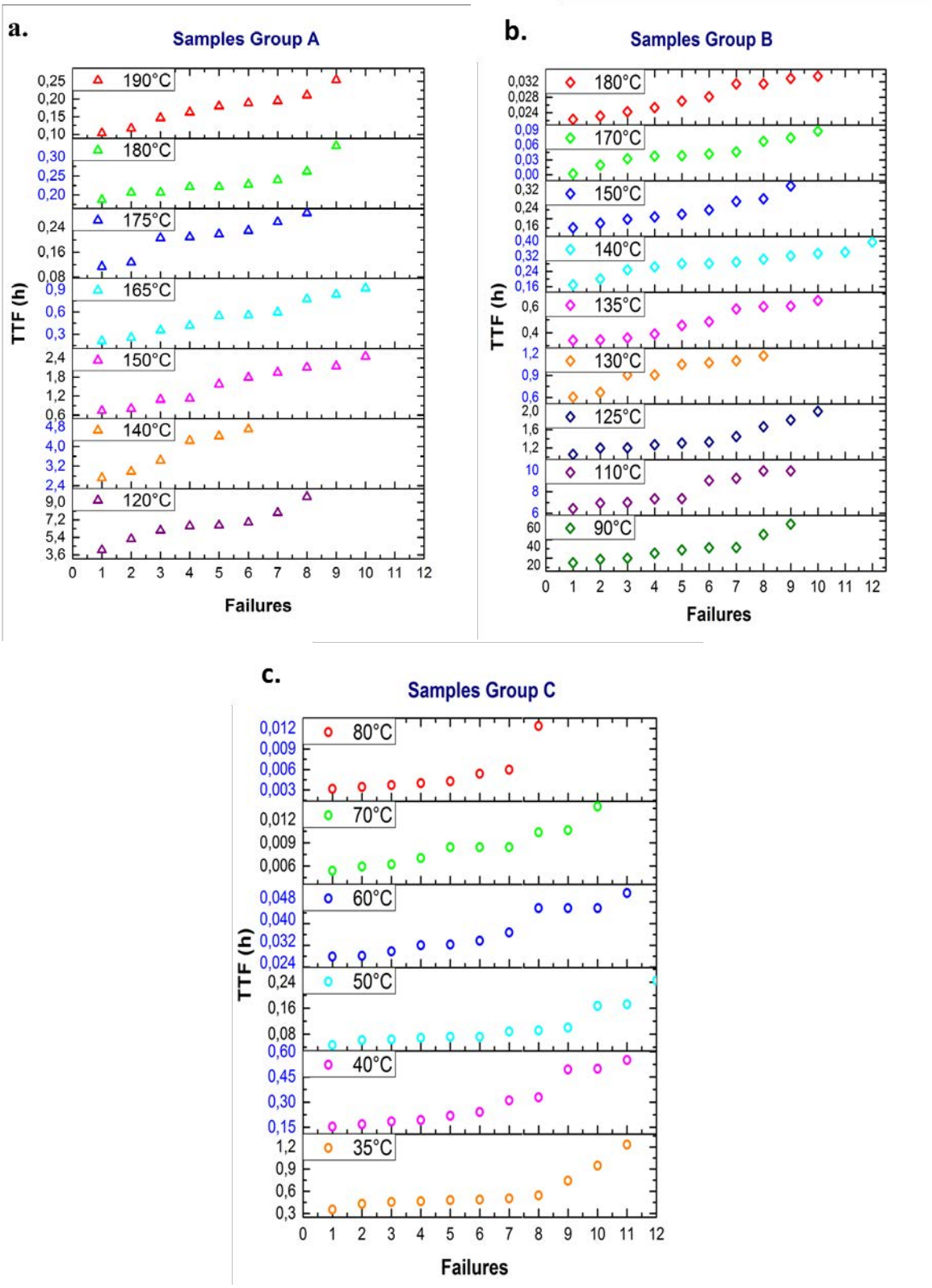

Figure 3.7. *Comparison of the TTF for MLCCs from (**a**) Group A, (**b**) Group B, and (**c**) Group C. HALT conditions: 600 V, temperature indicated on the plots.*

Table 3.1. *TTF when HALT is performed using different voltages and the same temperature.*

MLCC Group and HALT temperature conditions	**Range of TTF when tested at 400 V**	**Range of TTF when tested at 600 V**
Group A – 140 °C	21 – 30 h	3 – 5 h
Group B – 140 °C	3 – 4 h	0.2 – 0.4 h
Group C – 60 °C	5 – 13 min	2 – 4 min

As seen, the drop in the TTF values can be considered as significant, decreasing in several hours for the case of Group A and Group B and some minutes for the Group C. About the dispersion of the TTF results it is as well low, as seen in the time ranges in Fig. 3.7.

Until this point, it can be suspected that there is an interaction among the two stress variables. In further sections it will be analyzed considering the statistical analyses performed to the obtained results from HALT experiments.

3.2. The Weibull distribution

In this study, times to failure are fit to a Weibull distribution and the statistic $t_{63.2}$ has been chosen as the characteristic life of the samples.

The cumulative density function for the two-parameter Weibull distribution is represented by the following expression:

$$F(x) = 1 - e^{-(\frac{x-\gamma}{\alpha})^{\beta}} \qquad (1)$$

Where F(x) is the cumulative probability of failure, α is the scale parameter that represents the time or voltage for which the failure probability is 63.2%. The units of α are the same of the measured times or voltages. The shape parameter β is a measure of the range of the failure times or voltages,

and, the larger its value, the smaller is the range of measured data. The location (or threshold) parameter is frequently set as zero (it implies a threshold voltage in a progressive test or a threshold time to breakdown in a constant stress one) (Abernethy, 2006; Chauvet & Laurent, 1992 June; Diaham et al., 2010).

Data sets can be complete or censored; the second group corresponds to those sample sets in which not all of them present breakdown. Both the first or second type of data sets, they must be ranked, and a good approximation can be given by the median rank equation known as Bernard's approximation (Ross, 1999):

$$F(i,n) = \frac{i-0.44}{n+0.25} \qquad (2)$$

Where *i* represents the rank of a failed sample and n the total number of tested samples.

For plotting the Weibull distribution law, the cumulative density function (cdf) (1) must be transformed as follows:

$$ln\left(1 - F(x)\right) = ln\left(e^{-(\frac{x}{\alpha})^{\beta}}\right) \qquad (3)$$

$$ln\left(1 - F(x)\right) = -\left(\frac{x}{\alpha}\right)^{\beta} \qquad (4)$$

$$ln\left[-ln\left(1 - F(x)\right)\right] = \beta\, ln\left(\frac{x}{\alpha}\right) \qquad (5)$$

$$ln\left[ln\left(\frac{1}{1-F(x)}\right)\right] = \beta\, ln(x) - \beta\, ln(\alpha) \qquad (6)$$

The equation 6 represents the linear way to plot the Weibull *cdf*, having as the terms:

$$y = ln\left[ln\left(\frac{1}{1 - F(x)}\right)\right];\ x = ln(x);\ b = -\beta\, ln(\alpha);\ m = \beta$$

From where is possible to obtain the values of α and β.

With the aim to know the α value, is possible to manipulate the Weibull cdf equation so this value can be read from the x-axis time scale, it can be expressed mathematically as $\alpha = x$, substituting this into the Weibull function, we get:

$$F(x) = 1 - e^{\frac{\alpha^{\beta}}{\alpha}}$$

$$= 1 - e^{-1}$$

$$= 0.632$$

The characteristic life has as unique feature that it occurs at the F(x) = 63.2% regardless of the Weibull distribution, i.e. the β value.

In the present work, the Weibull parameters have been determined applying a graphical and an analytical procedure, the median rank (MR) and the least squares method (LSM), which in fact is related with the first one and is also known as the rank regression method (RRM) because the estimation of the parameters by using it is dependent upon regressing some form of logarithm and rank transformations of the data according to the rank position (Nwobi & Ugomma, 2014; Ross, 1999).

The reliability of different samples of multilayer ceramic capacitors (MLCCs) was studied by the performing of highly accelerated life tests (HALT). Regarding fit the results to a statistical model, a number of mean time to failure (MTTF) data under various levels of electric (V) and thermal (T) stress were collected (Liu, 2013).

As previously described, data was collected from HALT at different values of temperature and two voltage values, 400 V and 600 V. It is worth to emphasize that choosing to perform the HALT using distinct voltages and thermal values that covered really low and high temperatures had the goal to

observe the behavior of the insulation resistance in a wide window of imposed stresses. This was thought on the basis that it has been reported that the failure modes are related with the slope of the Weibull fitting (Abernethy, 2006; Liu & Sampson, 2012), but this parameter can be quite different depending on the range of stress levels in which the HALT is being carried out (Härtler, 1986). This could lead to an inaccurate prediction of the life-time from the TTF obtained data. In fact, there are other factors that can influence the prediction of the life time, such as the fact that to induce the dielectric breakdown under the nature of the HALT, is necessary to apply stress values that might introduce different failure mechanisms, different to the ones that could be present under normal conditions of use. Also, since more than one failure mode could be present, the statistical model used for the data analyses, must be capable to show those mechanisms (Liu, 2013).

3.2.1. Weibull analysis – Group A

The Fig. 3.8.a and Fig. 3.8.b show the life data points of MLCCs of the Group A, at 400 V and 600 V, respectively. Data was statistically analyzed and fitted according a Weibull distribution.

As seen in figures 3.18.a and 3.18.b the data fit properly with a Weibull distribution, showing an analogous behavior between the different temperatures; i.e. straight lines are obtained at different temperatures and are approximately parallel between them. Nevertheless, a different behavior of the distribution is observed for temperatures higher than 200 °C.

Thus, it could be said not only that life distribution under different thermal stress values obey the Weibull distribution but also, the failure mechanism(s) of the MLCCs – Group A appear to be the same up to a 200 °C (Wang, Gong, & Grzybowski, 2011). A change in the behavior of the failures when thermal stress is higher than 200 °C is related with a new failure mechanism. Also, the observation of this behavior supports the choice of studying a wide range of temperatures while keeping the electrical stress constant. Our results until now show that when HALT is performed at

low thermal stresses the dispersion and the distribution of the failures is not the same that at high temperatures.

From the linear equation of each plot shown in Fig. 3.8 were determined the parameters α and β, that are associated to the characteristic life and may provide a clue of physics of failure, respectively. The values of the scale parameter α and the shape parameter β for each temperature and voltage are presented in the Table 3.2. For both electrical stress values, the characteristic life decreases as the temperature increases, this behavior was also observed when testing the samples in the probe station. In the case of the α value, it is constantly reduced until the temperature is 200 °C, from there it does not present a clear pattern. The changes of α according the testing temperatures are shown in Fig. 3.9. In the figure is possible to see that not all the points could be fitted under a same distribution as the selected ones are delimited by the dashed lines in Fig. 3.9. With respect to the observed influence of the electrical effect, it is noticeable that it decreases the median life of the capacitors as well, so it confirms that both stresses affect significantly the insulation resistance of the samples.

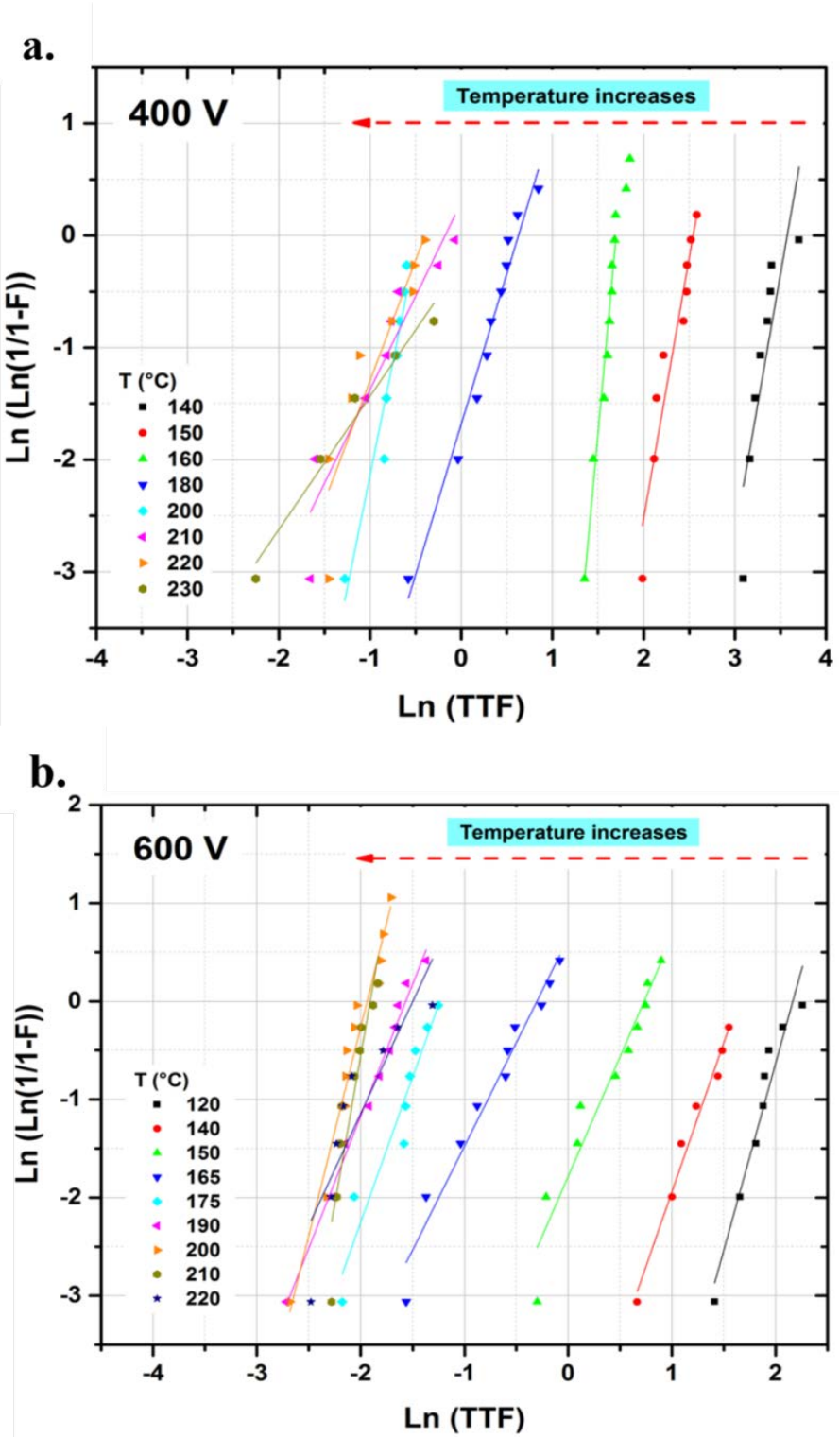

Figure 3.8. *Weibull plot for Group A. HALT conditions: (**a**) 400 V, 140 – 230 °C and (**b**) 600 V, 140 – 220 °C.*

Taking into account that the values obtained for T > 200 °C are not congruent with the expected response to the imposed thermal stress, only values below this limit were considered for further determination of the activation energy for the failure, considering that another mode of failure could be involved up to this limit.

On the other hand, the values of the shape parameter (β) determined for the data gathered using 400 V and temperatures below 200 °C are all higher than 2 and beyond that temperature they tend to be lower than 2. For the 600 V case, the β values are above 2 for all the temperatures. However, this parameter does not present a tendency in function of the temperature as can be seen in Table 3.1. It has been reported that when 1.0 < β < 4.0 it implies failure due an early wear out, while if β > 4.0 it implies a rapid wear out (Liu & Sampson, 2012; Abernethy, 2006).

Table 3.2. *Weibull parameters for MLCCs - Group A.*

Voltage (V)	**Temperature (°C)**	**α (h)**	**β**	**Voltage (V)**	**Temperature (°C)**	**α (h)**	**β**
	140	35.67	4.66		120	8.71	3.81
	150	12.72	4,65		140	5.15	3.04
	160	5.62	8.89		150	2.08	2.44
	180	1.87	2.68		165	0.74	2.12
400	200	0.63	4.02	600	175	0.29	2.96
	210	0.84	1.67		190	0.21	2.69
	220	0.67	2.16		200	0.14	4.25
	230	1.23	1.19		210	0.15	6.05
	250	1.01	0.85		220	0.22	2.28

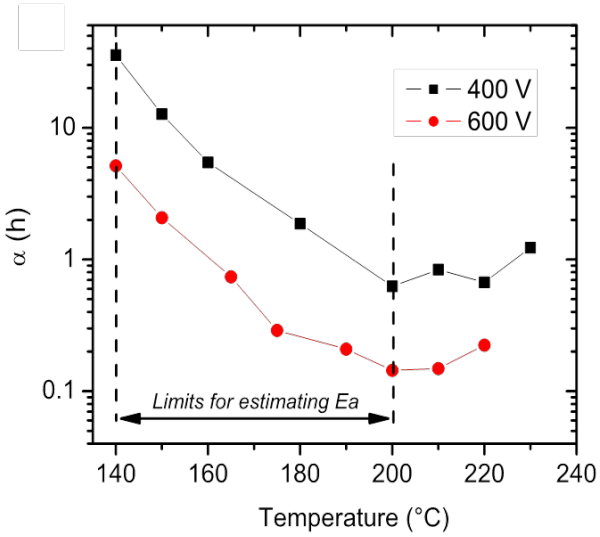

Figure 3.9. *Changes in the scale parameter of Group A as a function of the HALT temperature. The temperatures delimited by the dashed lines were considered for the Arrhenius plot in the next section.*

3.2.2. Weibull analysis – Group B

The times-to-failure of MLCCs from the Group B stressed at 400 and 600 V were determined and analyzed using the Weibull distribution. The results are shown in Fig. 3.10, in both cases of electrical stress it was found a similar behavior of data in the tested temperatures in terms of the applied fit. This leads to say that these samples fail under the same failure mode. Also, in Fig. 3.10.a is seen that when the HALT is performed at 400V and over 200 °C, the data obtained at 210 °C and 225 °C is almost overlapped with the data at 200 °C. In fact, as seen in Table 3.3, the α values for these three test temperatures (200 °, 210 ° and 225 °C) are the same.

The changes of the scale parameter are shown in Table 3.3 and more clearly in the Fig. 3.11, from there is possible to observe that it decreases as the temperature increases. Regarding the shape parameter, in this case the values are all higher than 2 and they do not present a tendency according the temperature.

The observed in the Fig.3.10 as well as the data shown in Table 3.3, show that the life of MLCCs - Group B is affected both, by higher values of thermal and electrical stress. The characteristic life

decreases when either stress is applied at higher values. However, it can be considered that the failure mechanism does not change in the used range of HALT conditions.

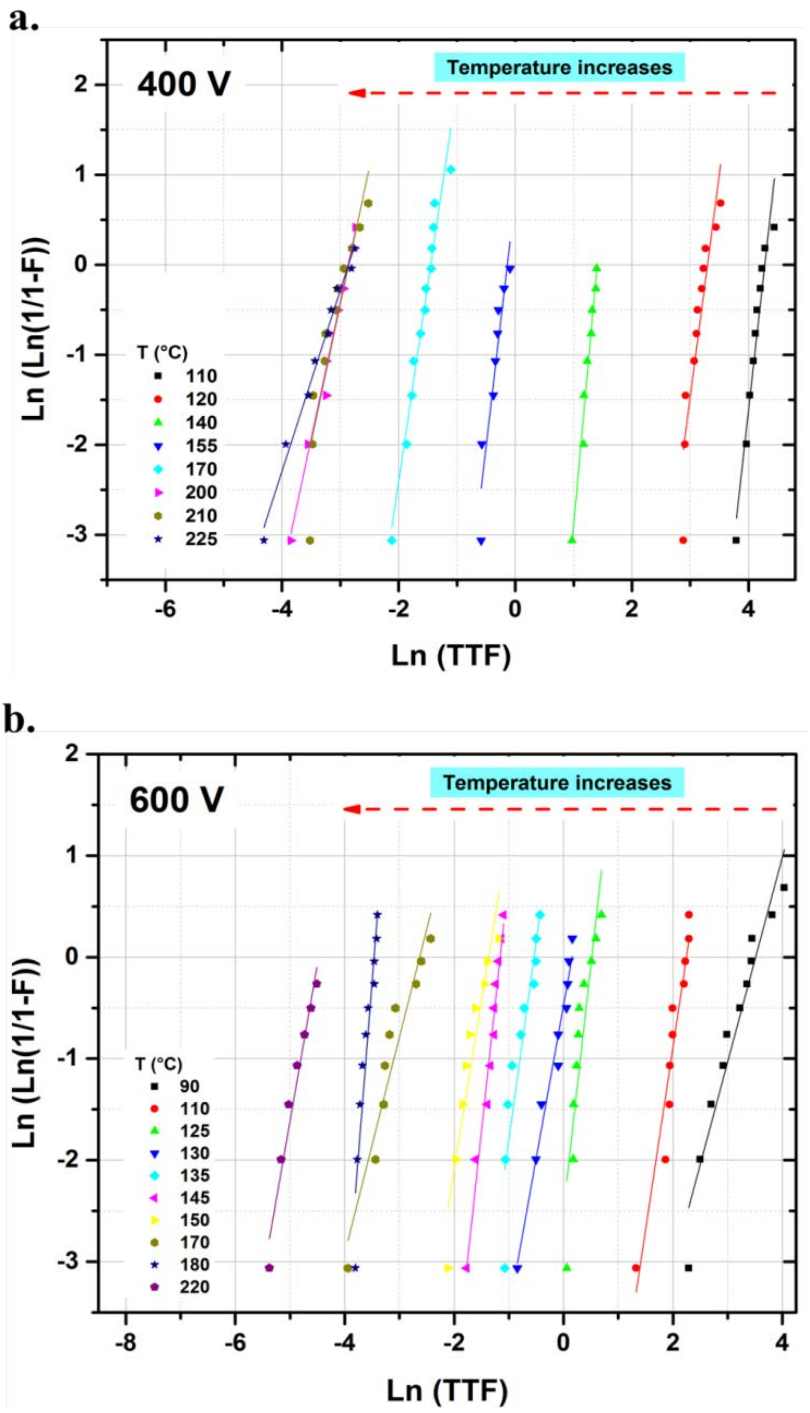

Figure 3.10. *Weibull plot for Group B. HALT conditions: (**a**) 400 V, 110 – 225 °C and (**b**) 600 V, 90 – 220 °C.*

Table 3.3. *Weibull parameters for MLCCs - Group B.*

Voltage (V)	Temperature (°C)	α (h)	β	Voltage (V)	Temperature (°C)	α (h)	β
400	110	72.2	5.8	600	90	33.5	2.02
	120	27.0	4.95		110	9.46	3.59
	140	4.07	7.16		125	1.68	4.81
	155	0.87	5.54		130	1.17	3.01
	170	0.23	4.59		135	0.58	3.9
	190	0.14	2.1		145	0.31	5.01
	200	0.06	3.11		150	0.25	3.32
	210	0.06	3.06		170	0.07	2.13
	225	0.06	2.01		180	0.03	6.81
					220	0.01	3.08

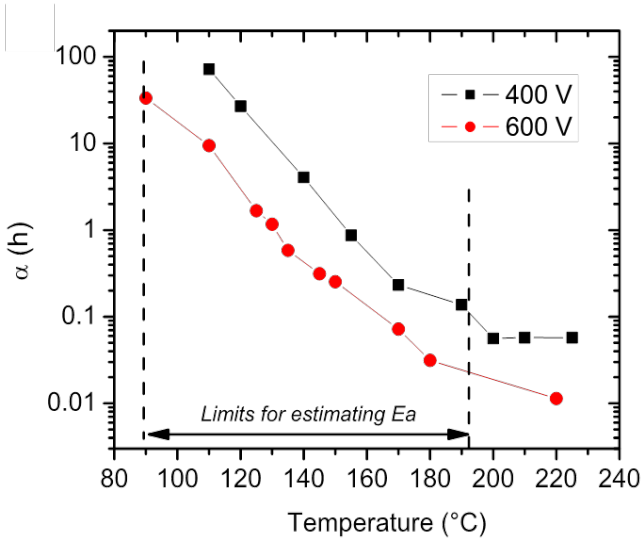

Figure 3.11. *Changes in the scale parameter of Group B as a function of the HALT temperature. The temperatures delimited by the dashed lines were considered for the Arrhenius plot in the next section.*

3.2.3. Weibull analyses – Group C

MLCCs from Group C have shown to behave different from those of groups A and B, being impossible to test them under exactly same experimental parameters. The temperature range used to test this group of samples was considerably lower than the one utilized for Groups A and B. This fact can lead to the consideration that the dielectric material of the Group C MLCCs is less resistant to the high stress values than the one of A and B samples; i.e., it has a lower insulation resistance.

Despite this fact and also with the aim to confirm these differences, HALT experiments were conducted and TTF at different temperatures using 400 V and 600 V were determined. The Weibull analysis was performed obtaining the plots observed in Fig. 3.12 and the parameters presented in Table 3.4 and Fig. 3.13.

TTF was as well affected, decreasing when either temperature or voltage values were augmented. Also, the behavior is fitted with a Weibull model and lines are parallel-like, indicating the failure of the samples occurs under the same mechanism(s). Some deviations from this behavior are observed in the cases of 80 °C and 90 °C (Fig. 3.12.a) and 80 °C when 600V are applied (Fig. 3.12.b), which could mean that similar to the cases of Group A and B, there is a limit of temperature under the one the failure mechanisms are the same and then a change occurs. This is as well reflected in the data shown in Table 3.4 and Fig. 3.13, from where is possible to see that the characteristic life decreases at higher temperatures with some exceptions after the 70 °C in both electrical stress cases. Also, at higher voltage the mean life is lower.

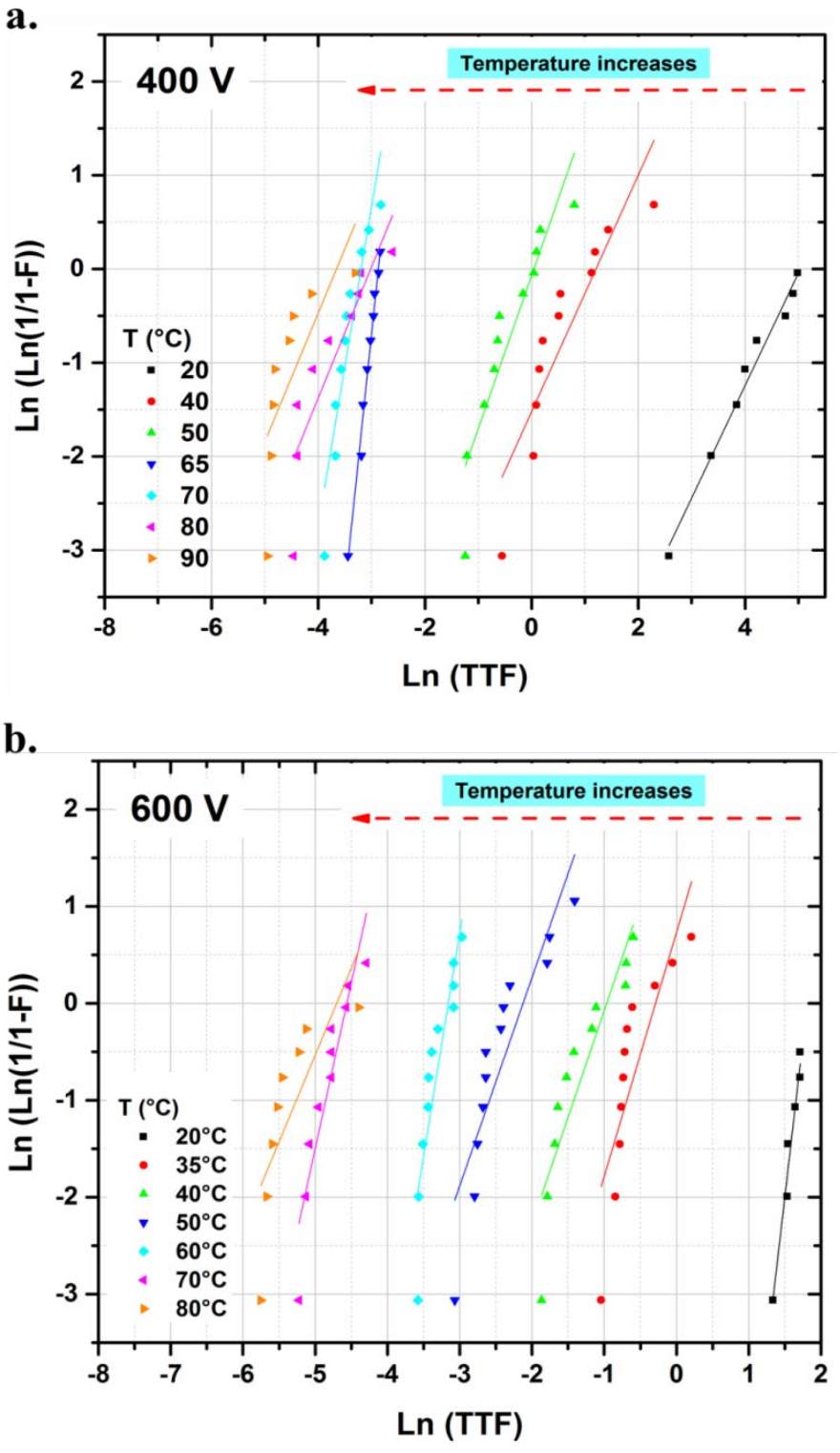

Figure 3.12. *Weibull plot for Group C. HALT conditions: (**a**) 400 V, 20 – 90 °C and (**b**) 600 V, 20 – 80 °C.*

Table 3.4. *Weibull parameters for MLCCs - Group C.*

Voltage (V)	Temperature (°C)	α (h)	β	Voltage (V)	Temperature (°C)	α (h)	β
	20	154.2	1.20		20	6.11	6.44
	40	3.34	1.26		35	0.75	2.52
	50	1.04	1.63		40	0.38	2.20
400	65	0.06	5.45	600	50	0.12	2.15
	70	0.04	3.40		60	0.04	4.61
	80	0.05	1.40		70	0.01	3.42
	90	0.03	1.37		80	0.01	1.80

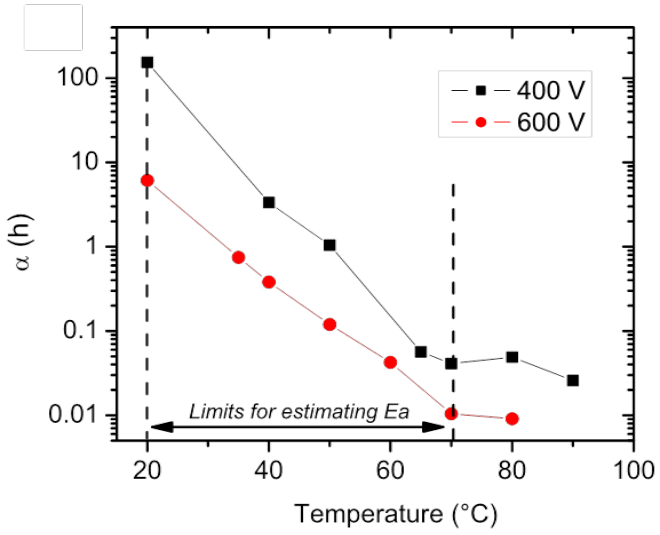

Figure 3.13. *Changes in the scale parameter of Group C as a function of the HALT temperature. The temperatures delimited by the dashed lines were considered for the Arrhenius plot in the next section.*

With the performance of high accelerated life tests at different temperatures and voltages it was possible to differentiate the groups according to its insulation resistance. According to the statistical analyses of the obtained data, the Group A has the higher mean life time, then the Group B and last, the Group C.

The three groups of MLCCs samples were designed based on a typical X7R composition with 1.05 % of Y_2O_3. However, the composition of their dielectric material, i.e. the amount of dopants in each one, is not exactly the same. This might be reflected in the behavior of the samples when they are tested under a HALT, as the results analyzed by the Weibull distribution have shown.

The following step to continue with the characterization of the samples through its characteristic life is to determine the activation energy (E_a) related to the failures. The estimation of the E_a will be based on the collected accelerated-tests data and applying the Arrhenius-Weibull model. Once the parameters of the life-stress have been determined using the Weibull distribution as the life distribution as in our case, it is possible to utilize the Arrhenius model to find the E_a value.

It is worth to remind that the activation energy that will be determined for each group of MLCCs does not represent a single particular failure mode since a combination of failure modes can be given according the tests conditions and other parameters inherent to the nature of the dielectric material such as its composition or even the production process of the ceramic capacitors (Groebel, Mettas, & Sun, 2001).

Regarding the parameters determined by the Weibull analyses, all the shape (slope) parameters were higher than 1. This indicates that the failures cannot be reversed by a regular thermal process (burn-in) as if they were infant mortalities.

3.3. Arrhenius model applied to the analysis of combined stress (V, T) effect over MLCCs life.

HALT uses the simultaneous application of an electric and thermal stress while measuring the time to failure (TTF) for the MLCCs. These two combined factors can induce a shorter time to failure that provides information about the expected life under service conditions. In the case of the temperature, as for other thermally activated processes, failure seems to follow an Arrhenius-type

behavior (Eq. 1), with the failure frequency (inverse of time to failure) increasing with an increase in temperature (Groebel, 2001; Hartler, 1986; Liu, 2015).

$$\frac{1}{t} = Ae^{-E_a/kT} \tag{1}$$

t: time to failure (TTF) (s);

E_a: activation energy for the thermally activated process (eV);

k: Boltzmann's constant (8.62×10^{-5} eV/K);

T: absolute temperature (K);

A: pre-exponential factor (s^{-1}).

The TTF due to thermal activation at a given temperature can be calculated from the data at different temperatures if the activation energy is known from Eq. 1, as a set of two time-temperature conditions (Eq. 2).

$$\frac{t_1}{t_2} = e^{\frac{E_a}{k}(\frac{1}{T_1}-\frac{1}{T_2})} \tag{2}$$

where t_1 = TTF, at T_1 and V_1, (s); and t_2 = TTF, at T_2 and V_2, (s).

In Eq. 2, both the activation energy and the pre-exponential factors in Eq. 1 are constant. Regarding factor A, it represents the minimum TTF, which is consistent with the fact that these processes do not take place instantaneously, even at a very high temperature.

Since the electric field affects the time to failure of the capacitors, an empirical equation in which the pre-exponential factor that is still constant is modified by the applied voltage, has been proposed (Eq. 3) (Ashburn, 2013).

$$\frac{t_1}{t_2} = \left(\frac{V_2}{V_1}\right)^n e^{\frac{E_a}{k}(\frac{1}{T_1}-\frac{1}{T_2})} \tag{3}$$

t_1 = TTF, at T_1 and V_1, (s);

t_2 = TTF, at T_2 and V_2, (s);

V_1 and V_2 = test voltages under conditions (V);

n = voltage stress exponent;

E_a = activation energy for dielectric wear out (eV);

k = Boltzmann's constant (8.62×10^{-5} eV/K);

T_1 and T_2 = absolute test temperature (K).

These factors are well-described in the literature (Ashburn, 2013) and the expected coefficient of the voltage stress exponent (n) is in the range of 1.5–7.1 (Ashburn, 2013; Maher, G., Wilson & Maher, S., 2003; Randall, Gurav, Skamser, & Beeson, 2003). This great variation in n is an indicator of the uncertainty related to the effect of the voltage. It also highlights the importance of determining any correlations of the basic structural and chemical formulation with the reliability (TTF) of capacitors.

Very few studies in the literature addressing this were found, which is understandable because producing MLCCs for reliability testing requires at least pilot size facilities to produce many samples with a reproducible process in order to minimize the influence of other parameters than the one being tested.

The Arrhenius model was developed originally to define the rates of chemical reaction according to the temperature it is carried out. However, it has also been applied in accelerated life testing because it helps to stablish a relationship between the reliability and the thermal (i.e. temperature) stress imposed during these tests. Commonly in the industry this model is applied with the assumption of fixed parameters that are related to defined values of failure mechanisms such as electromigration of corrosion. In the literature activation energy values can be found related to a precise type of material, electronic component or failure mode, and this is precisely what can represent an issue when using them to determine the characteristic life of a different system. The activation energy can provide clues about how the life of a product is affected by its service

conditions. This means that the activation energy can vary even from one product batch to another. Also, it can be different according to the present failure modes and which one can be prevalent. (Groebel, 2001; Hartler, 1986) In this work we chose to estimate the E_a based on the results of performed tests to get more accurate information regarding the effect of the imposed stresses in this study and the correlation of the same.

As we plotted the data according to Eq. 1, the activation energies can be estimated if we only consider the data below 200 °C for the Group A and Group B (Fig. 3.9 and Fig. 3.11) samples and below 70 °C for the Group C (Fig. 3.9) samples. Eq. 1 shows the relationship of the frequency of failure (mean time to failure; MTTF), as shown below in Eq. 4, which can be transformed into Eq. 5 to obtain the activation energies related to the failures of the three types of MLCCs. The E_a values were determined by applying the Arrhenius model to the life time of the capacitors (Fig. 3.14).

$$\frac{1}{t} = Ae^{-E_a/kT} = MTTF \tag{4}$$

$$\ln(MTTF) = \ln(A) - \frac{E_a}{kT} \tag{5}$$

where MTTF is the mean time to failure (s^{-1}).

The value of the E_a can be taken as a measure of the effect that the imposed thermal stress over the capacitor has on its life. Since the pre-exponential factor in this equation includes both the electrical stress and the thermal contributions (Eq. 3), a large activation energy value will imply a large effect of the imposed temperature on the capacitor life.

Applying the Arrhenius model, the plots shown in Fig. 3.14 were obtained. Then a linear fitting according equation (3) was adapted and the values of the activation energy were determined and are presented in Table 3.5.

a.

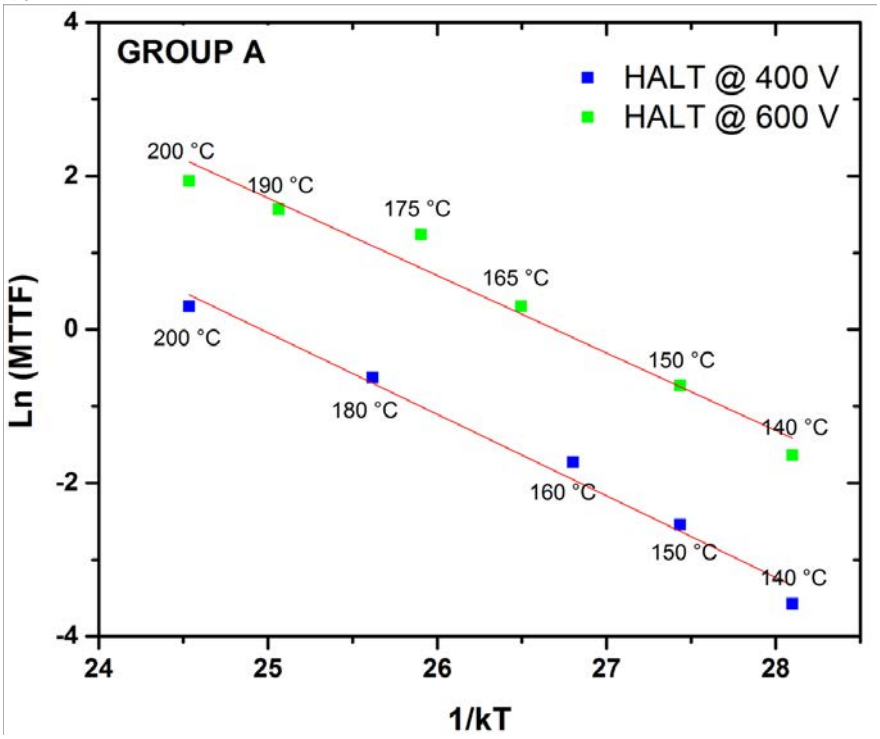
GROUP A
HALT @ 400 V
HALT @ 600 V
200 °C
190 °C
175 °C
165 °C
150 °C
140 °C
200 °C
180 °C
160 °C
150 °C
140 °C
Ln (MTTF)
1/kT
4
2
0
-2
-4
24
25
26
27
28

b.

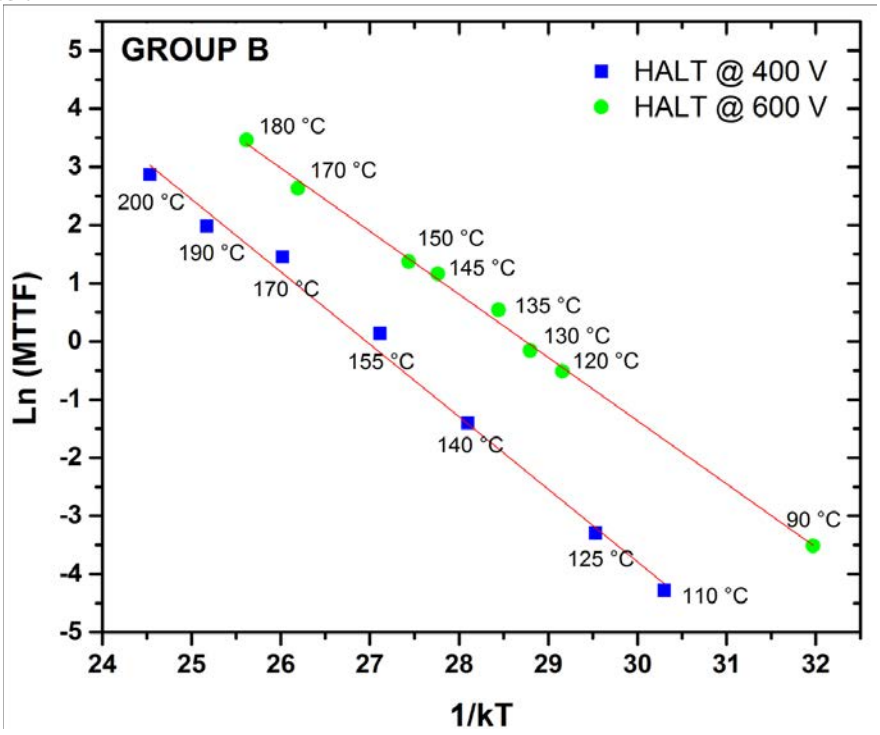
GROUP B
HALT @ 400 V
HALT @ 600 V
180 °C
170 °C
150 °C
145 °C
135 °C
130 °C
120 °C
90 °C
200 °C
190 °C
170 °C
155 °C
140 °C
125 °C
110 °C
Ln (MTTF)
1/kT
5
4
3
2
1
0
-1
-2
-3
-4
-5
24
25
26
27
28
29
30
31
32

c.

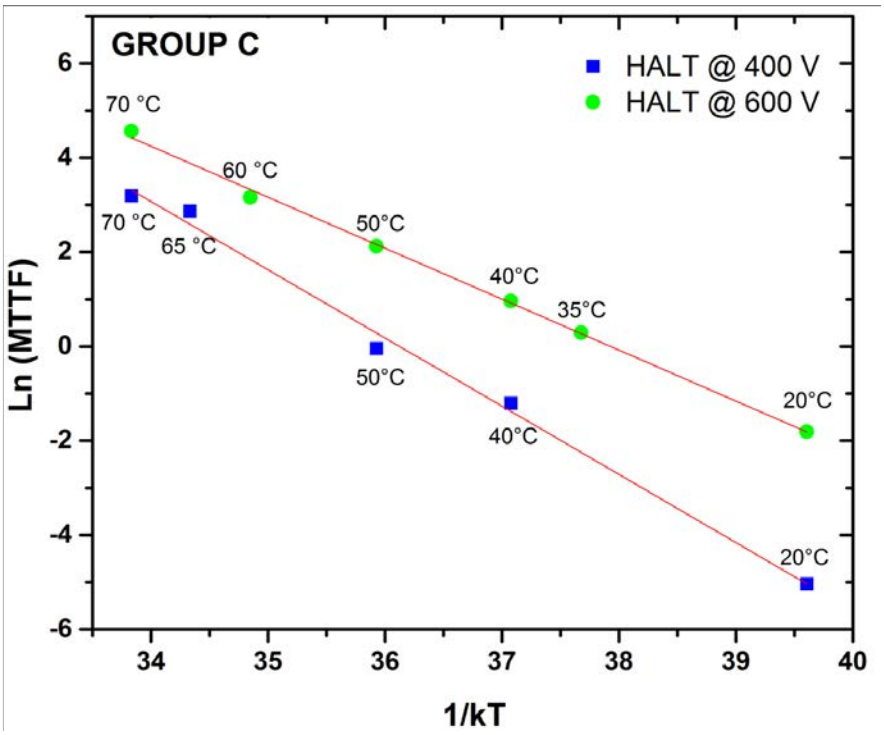

Figure 3.14. *Characteristic life according the Arrhenius model for MLCCs from (**a**) Group A, (**b**) Group B, and (**c**) Group C according the electrical and thermal stress. Solid lines represent the best fits given by equation (3).*

The activation energies are reported in Table 3.5. Those values are calculated by assuming that the voltage and thermal effects are a single combined factor and thus, the activation energy was calculated following the Arrhenius expression.

The activation energy values found when HALT was performed using 400 V show that the thermal effect is higher for the MLCCs from Group C, then for Group B and last the Group A. This confirms what we have previously stated, the life of MLCCs - Group A will change slowly as the temperature changes, i.e., it has better insulation resistance than the other samples. Regarding the E_a found when 600 V were applied, is possible to say that the values are different compared to the ones at 400 V for Groups B and C, while the E_a of the Group A is not significantly different when electric stress is higher. This can indicate that lives of Groups B and C are more affected when

voltage is higher than life of Group A, so their failure mechanism(s) can be activated faster when the electrical stress is as well increased. Also, the E_a values for the three groups at 600 V are rather similar. These results can indicate that the electrical stress affects in a lesser extension the life of the tested capacitors than the thermal stress does it.

Table 3.5. *Activation energy values obtained from Arrhenius-Weibull model for MLCCs tested under two different voltages and a range of temperatures.*

MLCCs Group	*E*a (eV) at 400 V	*E*a (eV) at 600 V	ln(*A*) at 400 V	ln(*A*) at 600 V	Temperature Range at 400 V	Temperature Range at 600 V
A	1.06 ± 0.07	1.01 ± 0.09	26.96 ± 2.5	26.52 ± 2.1	140–200 °C	120–200 °C
B	1.25 ± 0.06	1.09 ± 0.02	33.62 ± 1.3	31.23 ± 0.7	110–200 °C	90–180 °C
C	1.45 ± 0.05	1.08 ± 0.02	39.90 ± 2.9	38.30 ± 1.8	20–70 °C	20–70 °C

The numeric values of the activation energies should be related to the failure mechanism of the dielectric breakdown under stress conditions. It has been reported in general that the activation energy value of 1.9 eV was associated with an avalanche breakdown mode; while this can be in a range of 1.25–1.42 eV for the thermal activated failure (Nomura, Miura, Arashi, Nakano, & Sato, 1996; Rawal, & Chan, 1984). Other authors have suggested that for a thermal breakdown in MLCCs, the E_a will fall within the range of 1–2 eV (Liu & Sampson, 2012). Furthermore, the values in a range from 1.3 – 1.5 eV have been described as being related to a dielectric wear out in $BaTiO_3$-based dielectric capacitors (Yoon, Lee, & Lee, 2009).

Considering this and the results described in this work, such as the E_a values presented in Table 3.5, it could be confirmed that the failures were highly influenced by a thermal activated breakdown process. It is worth to remind that electronic components may have multiple failure modes and one of them tends to prevail over the others, and the found results in this kind of works can be pointing out to it; i.e., to the one with the lower activation energy. For this reason, we consider it is better not to take the reported E_a values since it should be determined for the conditions of the experimental life test instead of simply associate one by default. Nevertheless, it is possible to use the value of the

activation energy to know and describe how large it is the effect that the imposed stress is causing over the time-life of capacitors. In this work it could be seen that the capacitors (when HALT is conducted at 400 V) have different E_a, giving us a clue about which one is most affected by the thermal stress.

Even if the activation energy ranges overlap, this does not contribute to defining the exact failure mechanism. Among the possible mechanisms that may explain the obtained values, Chazono et al. (Chazono, & Kishi, 2001) proposed that the oxygen vacancies migrate under the influence of the high electrical field that is applied during the HALT testing. Yoon et al. (2009) suggested that as the vacancies are accumulated at the electrode interface, a Fowler-Nordheim (tunneling) conduction mechanism can be induced, which favors the breakdown of the dielectric layer due to the local increase in the conductivity. The activation energies within the range of 1–2 eV fall reasonably within the range of the E_a required for the mobility of oxygen vacancies (Chan, Sharma, & Smyth, 1981; Han, Appleby, & Smyth, 1987). In the present study, higher doping with calcium had a significant impact on the time to failure of the Group C samples.

A rough estimation of *n* for Group A composition, which only considered the test conducted at the same temperature, so that the relationship excludes the thermal part between 400 V and 600 V, gives the average value reported in Table 3.6 (*n* (T_1 = T_2)). To calculate this parameter with all the temperatures and the two voltages by means of the objective function (Eq. 6), the obtained values of n are shown in Table 3.6 (*n* (all conditions)).

$$fo = -\ln\left(\frac{t_1}{t_2}\right) + n\ln\left(\frac{V_2}{V_1}\right) + \frac{Ea}{k}\left(\frac{1}{T_1} - \frac{1}{T_2}\right) \quad (6)$$

Table 3.6. *Voltage stress constant (n).*

Group	*n* (T_1 = T_2)	*n* (All Conditions)
A	5.51	4.46
B	1.93	5.02
C	4.95	3.26

Although all values in Table 3.6 seem to be consistent with other reports (Rawal & Chan, 1984), the most accurate is *n* (all conditions) because it predicts the failure time under more conditions.

Is important to mention that with the results find in this work we cannot specifically talk about the reliability of the tested MLCCs, however we could consider them as reliable under certain use conditions. At an industrial level is rather the same way, since they are defined reliable within the determined use conditions by the producer. Also, the performance of this type of electronic components is highly related to its base-material composition itself. Considering this, we think that the differences found about the behavior of the capacitors that lead us to say that some groups are more affected by the high stress levels can be analyzed as well from a chemical compositional point of view of its dielectric material. Since it has been reported that the decrease in the insulation resistance of ceramic capacitors can be due to the formation of secondary phases such as the $Y_2Ti_2O_7$ in the $BaTiO_3$ dielectric layers (Zhang et al, 2016), we continued this work with the systematic analyses of two of the base-powders use for the fabrication of the MLCCs from Group B and Group C, considering the fact that they seem to be the less reliable. In the next part of this Chapter we are going to develop a study based on the doping of $BaTiO_3$ powders with Y_2O_3. The aim of this study will be to drive the system in an isolated way (not in the form of capacitors but prepared as ceramics) to the formation of secondary phases and by the performance of structural and microstructural analyses determine if the $BaTiO_3$ structure can be affected by its presence, and maybe understand how this can change its electrical properties.

References

Abernethy, R. B. (2006). The new Weibull handbook fifth edition, reliability and statistical analysis for predicting life, safety, supportability, risk, cost and warranty claims. *Published and distributed by Robert B. Abernethy*.

Ashburn, T., & Skamser, D. (2008, January). Highly accelerated testing of capacitors for medical applications. In *Proceedings of the 5th SMTA Medical Electronics Symposium*.

Chan, N. H., Sharma, R. K., & Smyth, D. M. (1981). Nonstoichiometry in undoped $BaTiO_3$. *Journal of the American Ceramic Society*, 64(9), 556-562.

Chauvet, C., & Laurent, C. (1992, June). Breakdown statistics as a tool to investigate electrical aging. *Conduction and Breakdown in Solid Dielectrics, 1992. Proceedings of the 4th International Conference on* (pp. 483-487). IEEE.

Chazono, H., & Kishi, H. (2001). DC-electrical degradation of the BT-based material for multilayer ceramic capacitor with Ni internal electrode: impedance analysis and microstructure. *Japanese Journal of Applied Physics*, 40(9S), 5624.

Diaham, S., Zelmat, S., Locatelli, M. L., Dinculescu, S., Decup, M., & Lebey, T. (2010). Dielectric breakdown of polyimide films: Area, thickness and temperature dependence. *IEEE Transactions on Dielectrics and Electrical Insulation*, *17*(1).

Ellerman, P. (2012). Calculating Reliability using FIT & MTTF: Arrhenius HTOL Model. *microsemi, Tech. Rep*.

Fantozzi, G., Niepce, J. C., & Bonnefont, G. (2013). *Les céramiques industrielles: Propriétés, mise en forme et applications*. Paris FR: Dunod.

Foeller, P. Y., Dean, J. S., Reaney, I. M., & Sinclair, D. C. (2016). Design of a bilayer ceramic capacitor with low temperature coefficient of capacitance. *Applied Physics Letters*, *109*(8), 082904.

Groebel, D. J., Mettas, A., & Sun, F. B. (2001). Determination and interpretation of activation energy using accelerated-test data. In *Reliability and Maintainability Symposium, 2001. Proceedings. Annual* (pp. 58-63). IEEE.

Han, Y. H., Appleby, J. B., & Smyth, D. M. (1987). Calcium as an acceptor impurity in $BaTiO_3$. *Journal of the American Ceramic Society*, 70(2), 96-100.

Hartler, G. (1986). Parameter estimation for the Arrhenius model. *IEEE transactions on reliability*, *35*(4), 414-418.

IEC/IEEE Guide for the Statistical Analysis of Electrical Insulation Breakdown Data (Adoption of IEEE Std 930-2004), IEC 62539 First Edition 2007-07 IEEE 930, vol., no., pp.1-53, 2007 doi: 10.1109/IEEESTD.2007.4288250.

Liu, D., & Sampson, M. (2011). Reliability evaluation of base-metal-electrode multilayer ceramic capacitors for potential space applications. *CARTS proceed*, 45-63.

Liu, D. D., & Sampson, M. J. (2012). Some aspects of the failure mechanisms in $BaTiO_3$-Based multilayer ceramic capacitors.

Liu, D. (2013, March). Highly accelerated life stress testing (HALST) of base-metal electrode multilayer ceramic capacitors. In *Proc. CARTS* (pp. 235-248).

Liu, D. D. (2015). Insulation resistance degradation in Ni–$BaTiO_3$ multilayer ceramic capacitors. *IEEE Transactions on Components, Packaging and Manufacturing Technology*, *5*(1), 40-48.

Maher, G. H., Wilson, J. M., & Maher, S. G. (2003). Electric Field Effects on the Insulation Resistance and Reliability of Various Types of BaTiO3 based X7R MLCC's at Elevated Temperatures. *Group*, *1* (10), 3.

Nomura, T., Miura, J., Arashi, T., Nakano, Y., & Sato, A. (1996, August). Multilayer ceramic capacitors-recent trends. In *Applications of Ferroelectrics, 1996. ISAF'96., Proceedings of the Tenth IEEE International Symposium on* (Vol. 1, pp. 135-141). IEEE.

Nwobi, F. N., & Ugomma, C. A. (2014). A comparison of methods for the estimation of Weibull distribution parameters. *Metodoloski zvezki*, *11*(1), 65.

Paulsen, J., & Reed, E. (2001). Highly accelerated lifetesting (HALT) of kemet Base-Metal-Electrode (BME) ceramic chip capacitors. In *CARTS-CONFERENCE-* (pp. 265-270).

Paunović, V. V., Živković, L. M., Vračar, L., Mitić, V., & Miljković, M. M. (2004). The effects of additive on microstructure and electrical properties of $BaTiO_3$ ceramics. *Serbian Journal of Electrical Engineering*, *1*(3), 89-98.

Randall, M., Gurav, A., Skamser, D., & Beeson, J. (2003, March). Lifetime modeling of sub 2 micron dielectric thickness BME MLCC. In *CARTS-CONFERENCE-* (pp. 134-140). COMPONENTS TECHNOLOGY INSTITUTE INC..

Rawal, B. S., & Chan, N. H. (1984, May). Conduction and failure mechanisms in barium titanate based ceramics under highly accelerated conditions. In *Proceedings of the 34th Electronic Components Conference, New Orleans* (pp. 184-188).

Ross, R. (1999). Comparing linear regression and maximum likelihood methods to estimate Weibull distributions on limited data sets: systematic and random errors. In *Electrical Insulation and Dielectric Phenomena, 1999 Annual Report Conference on* (pp. 170-173). IEEE.

Scarpulla, J., Ayvazian, T., Buell, W., Campbell, M., Dubitsky, A., Lin, R., ... & Young, J. (2016, September). Thin MLCC (multi-layer ceramic capacitor) reliability evaluation using an accelerated ramp voltage test. In *Accelerated Stress Testing & Reliability Conference (ASTR), 2016 IEEE* (pp. 1-12). IEEE.

Tsur, Y., Dunbar, T. D., & Randall, C. A. (2001). Crystal and defect chemistry of rare earth cations in $BaTiO_3$. *Journal of electroceramics, 7*(1), 25-34.

Teverovsky, A. (2012). Breakdown voltages in ceramic capacitors with cracks. *IEEE Transactions on Dielectrics and Electrical Insulation, 19*(4).

Vassilious, A., & Mettas, A. (2001). Understanding accelerated life-testing analysis. In *Annual Reliability and Maintainability symposium, Tutorial Notes* (pp. 1-21).

Wang, J., Jiang, S., Jiang, D., Tian, J., Li, Y., & Wang, Y. (2012). Microstructural design of $BaTiO_3$-based ceramics for temperature-stable multilayer ceramic capacitors. *Ceramics International*, 38(7), 5853-5857.

Wang, M. J., Yang, H., Zhang, Q. L., Lin, Z. S., Zhang, Z. S., Yu, D., & Hu, L. (2014). Microstructure and dielectric properties of $BaTiO_3$ ceramic doped with yttrium, magnesium, gallium and silicon for AC capacitor application. *Materials Research Bulletin, 60*, 485-491.

Wang, Y., Gong, S., & Grzybowski, S. (2011). Reliability evaluation method for oil–paper insulation in power transformers. *Energies, 4*(9), 1362-1375.

Yoon, J. R., Lee, K. M., & Lee, S. W. (2009). Analysis the reliability of multilayer ceramic capacitor with inner Ni electrode under highly accelerated life test conditions. *Transactions on electrical and electronic materials, 10*(1), 5-8.

Yoon, D. H., & Lee, B. I. (2004). Processing of barium titanate tapes with different binders for MLCC applications—Part I: Optimization using design of experiments. *Journal of the European ceramic society, 24*(5), 739-752.

Zhang, J., Hou, Y., Zheng, M., Jia, W., Zhu, M., & Yan, H. (2016). The occupation behavior of Y_2O_3 and its effect on the microstructure and electric properties in X7R dielectrics. *Journal of the American Ceramic Society, 99*(4), 1375-1382.

Chapter 4: Y_2O_3-Doping of $BaTiO_3$

Introduction

In the tailoring of $BaTiO_3$ as the base dielectric material for MLCCs fabrication, it is important to define the relations between the structure, microstructure and electrical properties. There are reports of secondary phases due to the presence of other elements, such as the dopants, which addition is intended to improve the electrical properties of the material. Among the reported phases are the pyrochlores, $Y_2Ti_2O_7$ related to Y_2O_3, that as side effect are supposed to be the cause of long term failure mechanisms of MLCCs under nominal operation (Zhang et al., 2016).

This research is aimed to find the secondary phases in this material and to perform an evaluation of the reliability of MLCCs that use $BaTiO_3$ based material that might contain those phases. All the conditions to which the ceramic is exposed during its preparation, from the raw material to the last thermal treatment, must be well known as well as the output from those steps. For that reason, it is necessary to perform powders and ceramic characterization by techniques such as Induced Coupled Plasma (ICP) spectroscopy, X-Ray Diffraction analyses and SEM, to know the chemical composition, structure and phase composition, porosity and grain size, respectively.

The formulation used in this application must be designed to control the electromagnetic properties of the layer, especially at high temperature and under high electric field (Ashburn & Skamser, 2008; Yoon, Park, Hong, & Sinn, 2007) so that several additives and dopants are added to $BaTiO_3$. They include cations such as Mn^{2+}, Mg^{2+} and Ca^{2+}, which can partially compensate the electrons and holes in the system due to the presence of oxygen vacancies (Yoon et al., 2007; Yoon, Kang, Kwon, & Hur, 2010). They also include sintering aids, such as SiO_2, which reduce the sintering

temperature. Indeed, it has been reported that SiO_2 leads to the formation of a liquid phase from the ternary system BaO-TiO_2-SiO_2, diminishing the eutectic point from 1320 °C to near 1260 °C (Liu & Roseman, 1999; Koschek & Kubalek, 1987; Ösküs, Torman, S. Sen, & U. Sen, 2016). Rare-earth elements (Dy^{3+}, Ho^{3+}, Sm^{3+}, La^{3+}, Yb^{3+} or Y^{3+}) have been used as well; they substitute Ba and Ti sites in the $BaTiO_3$ structure (Zhang et al., 2016; Wang et al., 2014a). However, in particular Dy^{3+}, Ho^{3+} and Y^{3+}, have shown an amphoteric behavior (occupying A- or B-site) which claims to be helpful for the lifetime of the MLCCs (Tsur, Dunbar, & Randall, 2001). Y_2O_3 is commonly employed as dopant in the commercial formulation of powder for industrial fabrication of MLCCs because it results in similar properties than adding Ho_2O_3, Er_2O_3 or Dy_2O_3, and it is less expensive (Zhang et al., 2016). Dopants also take part in the formation of a so-called "core-shell" structure that is claimed to contribute to the temperature stability of the dielectric properties (Kim et al., 2008; Park et al., 2009; Wang et al. 2014; Zhang et al., 2016). Y^{3+} ionic radius (0.107 nm) is intermediate between that of the Ba^{2+} ion (0.161 nm) and the Ti^{4+} ion (0.06 nm). Therefore Y^{3+} can occupy either Ba^{2+} or Ti^{4+} cation site in the $BaTiO_3$ lattice (Tsur et al., 2001; Wang et al., 2014) and can behave as acceptor or donor according to the position in the lattice. The energy required to form a Ti^{4+} vacancy in the $BaTiO_3$ lattice is 7.56 eV whereas it is only 5.94 eV to form a Ba^{2+} vacancy (Belous, V'yunov, Kovalenko, & Makovec, 2005; Makovec, Samardžija, & Drofenik, 2004; Paredes-Olguín, Lira-Hernández, Gómez-Yañez & Espino-Cortes, 2013). The partial pressure of oxygen and sintering temperature will also induce the formation of Ba^{2+} or Ti^{4+} vacancies, leading Y^{3+} to occupy either one or both (Belous et al., 2005; Paredes-Olguín et al., 2013). This will be influenced also by the Ba/Ti ratio, the dopant concentration and its solubility, which varies according to Y^{3+} occupying either the Ba- or the Ti-site. Zhi et al. (1999) indicated a solubility of Y^{3+} at the Ba-site of about 1.5 at% when sintering in air at 1440 – 1470 °C, while it reaches 4 at% when sintering under reducing conditions (V'yunov, Kovalenko, Belous, & Belyakov, 2005). For the Ti-sites instead, the solubility is higher, i.e. around 12.2 at% at 1515°C when sintering in air. Wang et al. (2014a) reported that the introduction of Y^{3+} in the $BaTiO_3$ lattice can lead to structural

changes going from tetragonal to a so-called pseudocubic phase transformation. Also, it has been observed that the solid solubility of the dopant in the $BaTiO_3$ is surpassed, when secondary phases are formed as precipitates. In the case of Y^{3+}, Belous et al. (2008) reported the formation of the $Ba_6Ti_{17}O_{40}$ and $Y_2Ti_2O_7$ as secondary phases. The pyrochlore phase $Y_2Ti_2O_7$ was evidenced by Yoon et al. (2007) and Zhang et al. (2016) and they suspected that these phases are detrimental to the reliability of $BaTiO_3$-based MLCCs.

In this work, the role of Y_2O_3 was evaluated on two kinds of raw materials. The first one is pure $BaTiO_3$ while the second material is a commercial formulation designed for MLCCs of X7R type (-55 °C and 125 °C, 15% tolerance) which among other elements, already contains 1.05 wt% of Y_2O_3.

Powders and ceramics with different Y^{3+} doping concentrations (1 up to 20 wt%), as Y_2O_3, were prepared and subsequently thermally treated or sintered, respectively. The aim was to investigate the structural changes of $BaTiO_3$ induced by the doping with Y_2O_3 and to promote the formation of secondary phases.

4.1. $BaTiO_3$ raw powders

The chemical composition of the $BaTiO_3$ powders used as raw materials was determined by ICP analyses and is shown in Table 4.1. As previously mentioned, the powders that are formulated for an industrial application contain dopants and additives. In Table 4.2 is presented a brief summary of the function that these components should exert in the formulation of the $BaTiO_3$ powders as dielectric base of ceramic capacitors.

Table 4.1. *Ba/Ti ratio and chemical composition of $BaTiO_3$ powders.*

	Ba	**Ti**	**Y**	**Ca**	**Sr**	**Si**	**Mn**	**Mg**	**Co**
BT_A* **Ba/Ti = 2.88**	57.55	19.96	<0.01	0.006	0.04	<0.01	<0.001	0.001	<0.01
BT_B** **Ba/Ti = 2.85**	54.67	19.17	1.05	1.34	0.09	0.30	0.05	0.29	0.012
BT_C** **Ba/Ti = 2.86**	53.86	18.85	1.05	0.57	0.09	0.17	0.05	0.006	0.017

Values are given in wt%. *: BT reagent grade (pure). **: BT commercially formulated.

Table 4.2. *Additives and dopants on $BaTiO_3$ dielectric formulation.*

Compound	**Function**
SiO_2	Sintering aid that contributes to a better densification. Can contribute to the creation of a liquid phase, reducing the sintering temperature.
Mg^{2+}	Involved in the core-shell creation. Can replace Ti^{4+}-sites, inhibiting the grain growth.
Ca^{2+}	Can substitute A- or B-sites causing beneficial changes at a structural and electrical level. Contributes to enhance the reliability.
Mn^{2+}	Added to keep high insulation resistance. It can also inhibit the grain growth.
Rare Earth Elements (REE)	Particularly the amphoteric such as Dy^{3+}, Ho^{3+} and Y^{3+} (the one used in this study) have demonstrated to improve the MLCCs insulation resistance. Also involved in the core-shell creation.

The denomination of the different samples, according to the starting powder and the final concentration of Y_2O_3, is shown in the Table 4.3.

***Table 4.3**. Sample identification of prepared powders doped with Y_2O_3.*

Composition (wt% Y_2O_3)→ **Type of powder↓**	0	1.0	1.5	2.0	2.5	5.0	20.0
BT-A*	BT-A_0	BT-A_1	BT-A_1.5	BT-A_2	BT-A_2.5	BT-A_5	BT-A_20
BT-B**	------	BT-B_1	BT-B_1.5	BT-B_2	BT-B_2.5	BT-B_5	BT-B_20
BT-C**	------	BT-C_1	BT-C_1.5	BT-C_2	------	------	------

*: BT reagent grade (pure). **: BT commercially formulated.

4.2. $BaTiO_3$ powders thermal treatment and characterization

With the aim to observe any structural change induced by high level of doping, the powders BT-A_2.5, BT-A_5, BT-A_20, BT-B_2.5, BT-B_5, and BT-B_20 were thermally treated (TT) at 1310°C in air for 3 h. This thermal treatment replicates the sintering temperature conditions in which multilayer ceramic capacitors are produced at industry level. In this case the powders are denominated BT-X_YTT, where "X" indicates the raw $BaTiO_3$ powder, "Y" the Y_2O_3 wt%, and "TT" thermally treated.

- **Particles morphology and size**

SEM images of the undoped $BaTiO_3$ powders, BT-A_0 and BT-B_1, are shown in Fig. 4.1.a and Fig. 4.1.c respectively. Both powders present particles with a coarse-faceted morphology. Two particle sizes are observed, a range of 0.48 µm and 1.25 µm for the BT-A_0, and of 0.46 µm and 0.81 µm for the BT-B_1. The mean size value of the particles from BT-B_1 is roughly lower than the one of the BT-A_0 particles. This slight difference is probably related to the treatment given to the formulated powder to fulfill the particle size required for its use in the MLCCs production process.

After thermal treatment at high temperature, the SEM images of Y_2O_3-doped powders BT-A_5TT and BT-B_5TT (Fig. 4.1.b and Fig. 4.1.d), show more rounded and defined particles, compared to the non-thermally treated, non-doped powders (Fig. 4.1.a and Fig. 4.1.c, respectively). The mean grain size is similar for the two powders, respectively 0.58 µm and 0.53 µm. Some aggregates are observed, probably due to a beginning of sintering.

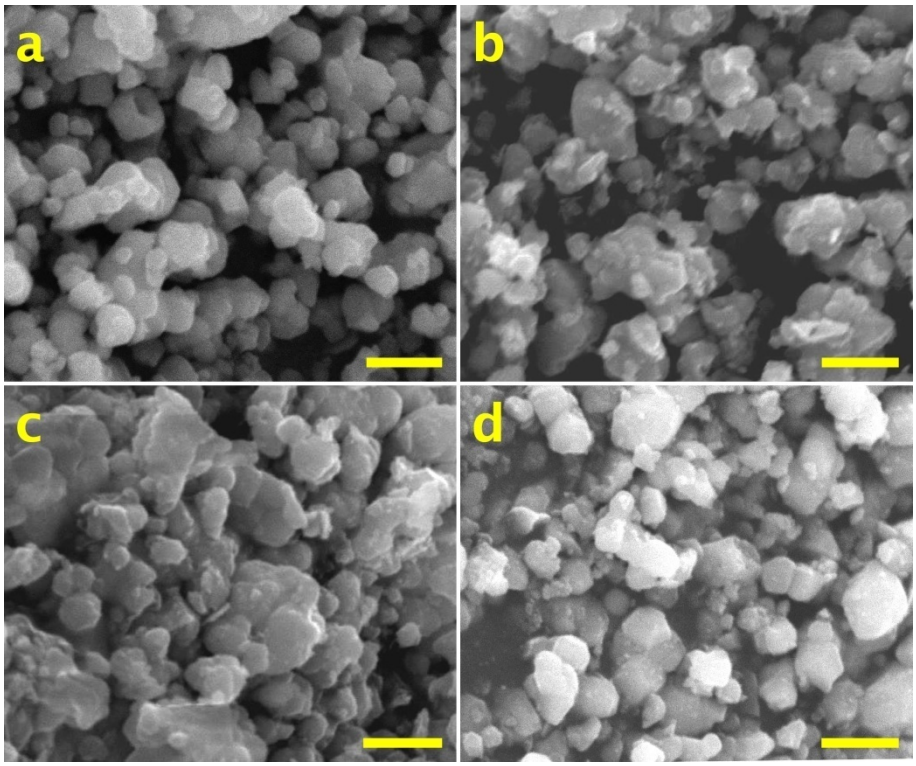

Figure 4.1. *SEM images of $BaTiO_3$ undoped raw powders and the respectively 5 wt% Y_2O_3-doped and thermally treated powders.* ***(a)*** *BT-A_0,* ***(b)*** *BT-A_5TT,* ***(c)*** *BT-B_1* ***(d)*** *BT-B_5TT powders. Scale bar: 1µm*

- **Structure and phase composition**

The way that the $BaTiO_3$ structure can be affected by an added dopant can be reflected in the c/a ratio, which changes from cubic structure (c/a = 1) to higher values when the crystal lattice is modified for reasons like the presence of other ions. This change in the c/a ratio is reflected directly in the diffraction pattern. For $BaTiO_3$ with a cubic crystalline phase, sharp peaks in a 2θ value

around 31.6° and 45.3° corresponding to the (110) and (200) planes respectively, are observed. When the symmetry of the system is not cubic anymore, it causes that certain planes can appear on the diffraction pattern. Thus, in some zones where just one peak was observed, are now spotted two or more depending on the crystalline arraignment. In the case of a tetragonal phase, the planes (101) and (110) will be seen, as well as the (002) and (200) around the same 2θ values previously mentioned. We calculated a theoretical change of the 2-theta value for the (002) plane as a function of the possible c/a ratio is shown in the Fig. 4.2. A change in the c/a ratio is more notorious for (002) and (200) planes since the distance between their peaks is higher than the one of (101) (110) peaks. In fact, as long as c/a value increases, the distance among their peaks is intensified; i.e. at higher values of c/a the tetragonality is more evident. Also, the intensity ratio between (002) and (200) peaks, when the $BaTiO_3$ is in a tetragonal phase, is 1:2. However if there is a gradient in the composition of the matrix, it is possible to have the presence of various c/a ratios, which leads to a different appearance of the peaks. They can look less intense, broaden and even like if they were joining.

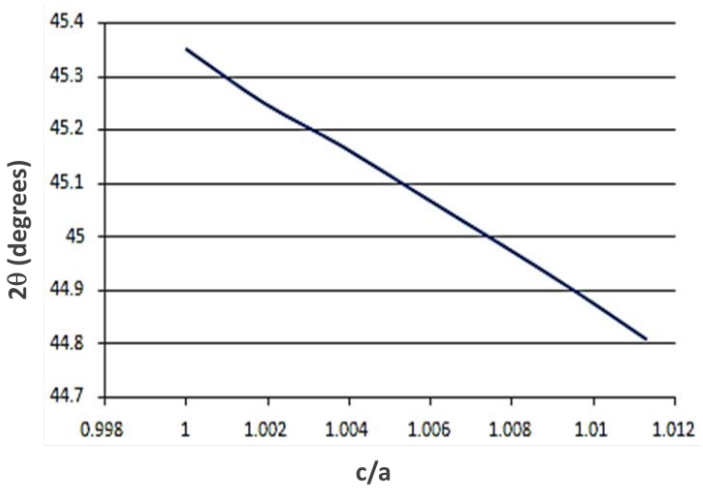

***Figure 4.2**. Variation of 2θ according the c/a ratio value, based on the cubic lattice 3.996 Å, for the planes (002).*

For these reasons, in this work we will discuss how the structural phase of the $BaTiO_3$ is affected by the presence of the added Y_2O_3, following principally the observable changes in the peaks around 45°.

To remind the structural phase of the $BaTiO_3$ starting powders, the corresponding diffractograms are shown in Fig. 4.3. The three powders present a distinct splitting of (002) and (200) planes around 45°, related to a tetragonal phase identified by the JCPDS: 89-1428. These results are going to be the base over which the structural analysis of the samples is going to be developed.

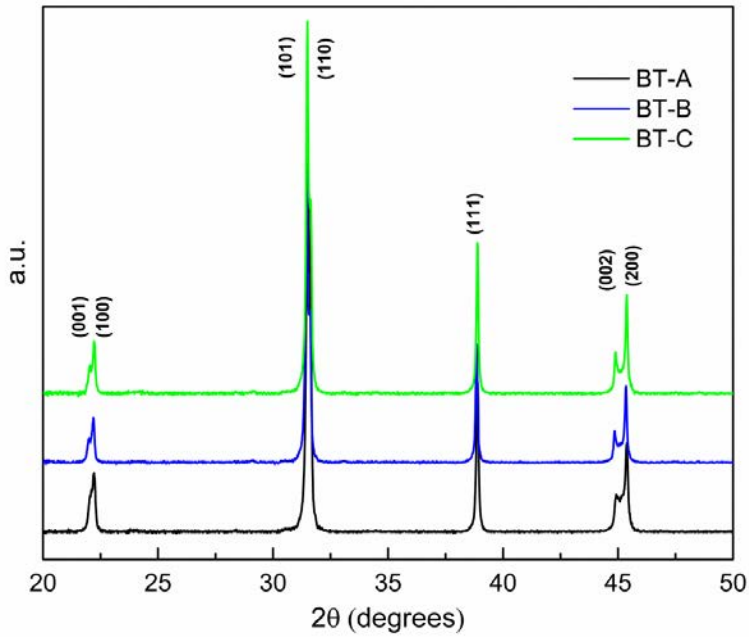

Figure 4.3. *X-ray diffraction patterns of raw $BaTiO_3$ powders. JCPDS: 89-1428.*

X-ray diffraction patterns corresponding to the thermally treated powders are presented in Fig. 4.4. The BT-A powders (Fig. 4.4.a) with Y_2O_3 content ranging from 0 to 20 wt% have a tetragonal crystalline structure, characterized by the two peaks around 45° which belong to the (002) and (200) planes. These two peaks are clearer seen in the enlargement made to this zone and shown in the Fig. 4.5.a. Thus, structurally the doped TT powders have no differences with respect to the undoped one. However, in the diffraction patterns of the thermally treated BT-A_5 and BT-A_20 (Fig. 4.4.a), is

possible to observe peaks corresponding to Y_2O_3 phase (JCPDS 89-5591) indicating that the solubility limit was surpassed.

On the other hand, the XRD patterns corresponding to the BT-B powders (Fig. 4.4.b) show more changes when Y_2O_3 concentration increases. In this case, we remind that the raw material already contains about 1.05 wt% of Y_2O_3. The pattern of powder BT-B_1 indicates a pure tetragonal phase, whereas those of powders containing more Y_2O_3 (2.5 wt% to 20 wt%) evidence a decrease of the tetragonality. In the Fig. 4.5.b can be observed with more detail the way in which the peaks around 45° look different with respect to the BT-B_1, being like joined. This might be related to an inhomogeneous distribution of the dopant in the BT matrix, which will lead to the presence of different c/a ratios in the samples; i.e. a mixture of tetragonal structures. Contrary to the BT-A samples, the Y_2O_3 phase is detected only for the BT-B_20 powder. Moreover, in the diffraction pattern of this sample, three additional peaks are detected between $2\theta \approx 29.5$ - 30°. They correspond to a secondary phase identified as $Ba_6Ti_{17}O_{40}$ (JCPDS 35-0817). This orthotitanate has been reported previously in different works such as the ones by Lu et al. (1990), Belous et al. (2008), and Paredes-Olguín et al. (2013). Since the BT-B matrix contains additives and dopants, it can be expected that they interact not only with the $BaTiO_3$ but also among them, and if an excess of ions is produced as a consequence, then some precipitates can get formed. In this case, it can be said that the incorporation of Y^{3+} atoms in the $BaTiO_3$ lattice leaded to a segregation of Ti^{4+}, being possible a a reaction between $BaTiO_3$ and TiO_2 producing the Ti-rich phase (Yuan, Zhang, & Li, 2004). Thus, the interaction between the doped matrix and the additives, under our experimental conditions, leaded to the precipitation of $Ba_6Ti_{17}O_{40}$.

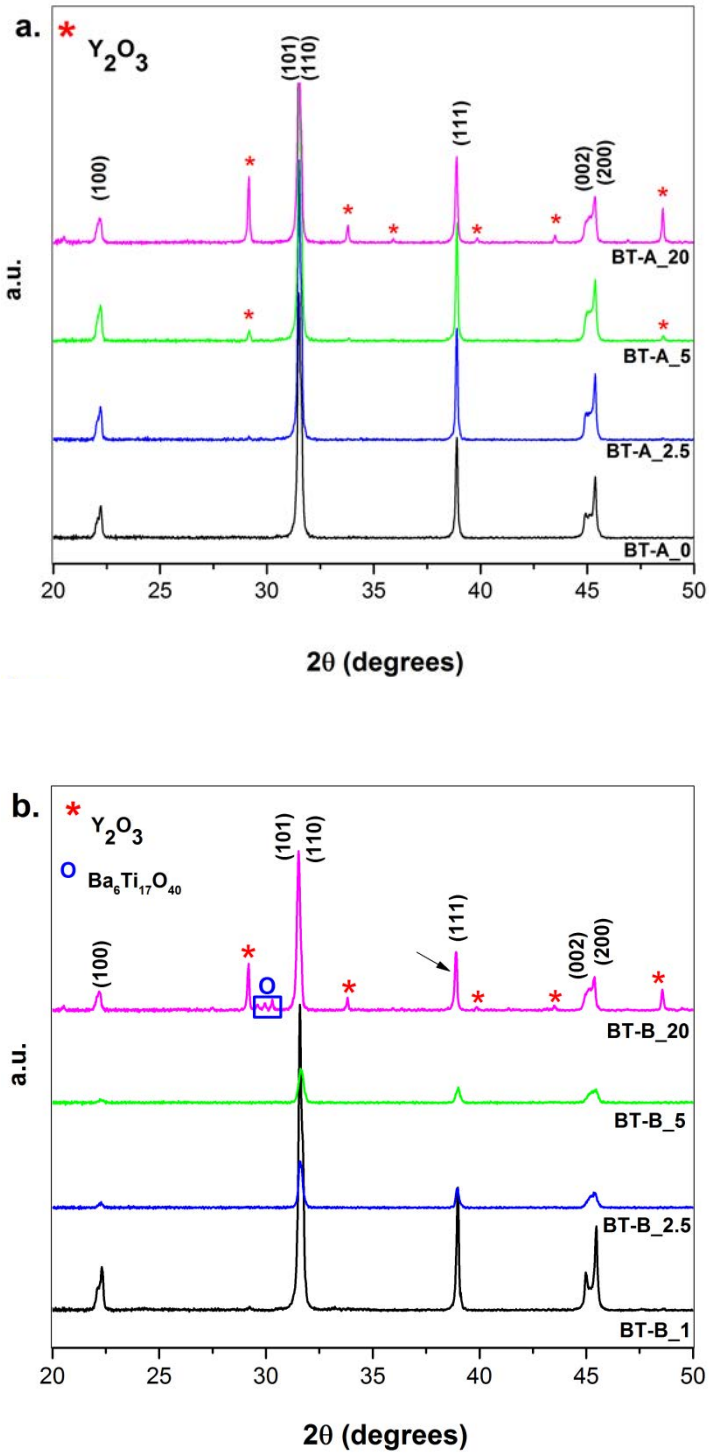

Figure 4.4. *X-ray diffraction patterns of thermally treated (1350 °C) undoped $BaTiO_3$ and Y_2O_3-doped $BaTiO_3$ (2.5, 5.0 and 20.0 wt%) powders. Powders issued from* ***(a)*** *BT-A and* ***(b)*** *BT-B.*

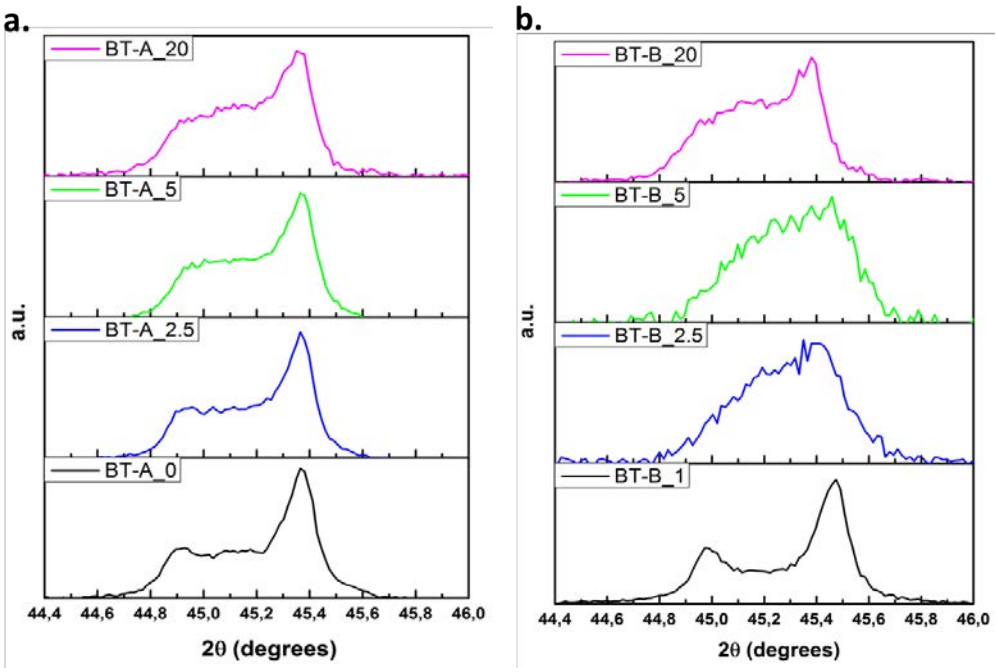

***Figure 4.5**. Enlargement in the zone around 45° for X-ray diffraction patterns of thermally treated (1350 °C) undoped $BaTiO_3$ and Y_2O_3-doped $BaTiO_3$ (2.5, 5.0 and 20.0 wt%) powders.*

4.3. $BaTiO_3$ ceramics characterization

The sintering of ceramics (powder compacted at 300 MPa) was carried out both, in air and reducing atmosphere following two different thermal cycles:

1) In air, two temperature steps: 1310 °C then 1150 °C for 15 h. The ceramics sintered using this program are BT-A (A_0, A_2.5, A_5) and BT-B (B_1, B_2.5, B_5).

2) In reducing atmosphere ($pO_2 \approx 10^{-8} – 10^{-11}$ atm, N_2, H_2O, H_2): 1310 °C for 3 h (this sintering process was carried out in industrial conditions (KEMET de México), simulating the production conditions of the MLCCs). The ceramics sintered using this program are BT-A (A_0, A_1.5, A_2, A_2.5, A_5, A_20), BT-B (B_1, B_1.5, B_2, B_2.5, B_5, B_20), and BT-C (C_1, C_1.5, C_2).

4.3.1. $BaTiO_3$ ceramics sintered in air

- **Density**

The density values of the BT-A and BT-B ceramics obtained under these sintering conditions are summarized in Table 4.4. It is possible to see that the high-level of Y_2O_3 affected the densification decreasing it with respect to the undoped samples. Nevertheless, as observed in Fig. 4.6, the density for BT-A undoped ceramic is higher than the one of the ceramics doped with 2.5 and 5 wt% Y_2O_3, although for these was quite equal. For the BT-B ceramics, the density values are different among them, being as well lower when the content of Y_2O_3 increases. Even when the densification for both cases (BT-A and BT-B) is lower according to the Y_2O_3 content, the ceramics formed from the BT-B powder present higher density values. This difference can be due to the additives present in the BT-B powder formulation, since one of the purposes for include them into the formulation is to improve the densification of the ceramic material.

Table 4.4. *Density of the ceramics sintered in air, two temperature steps: 1310 °C then 1150 °C for 15 h.*

$BaTiO_3$ raw material	**[Y_2O_3] (wt%)**	**Sample ID**	**Density (g/cm^3)**
BT-A (reagent-grade)	0	BT-A_0	5.62 ± 0.19
	2.5	BT-A_2.5	3.66 ± 0.03
	5	BT-A_5	3.67 ± 0.02
BT-B (commercially formulated)	1	BT-B_1	5.79 ± 0.07
	2.5	BT-B_2.5	4.82 ± 0.03
	5	BT-B_5	4.37 ± 0.02

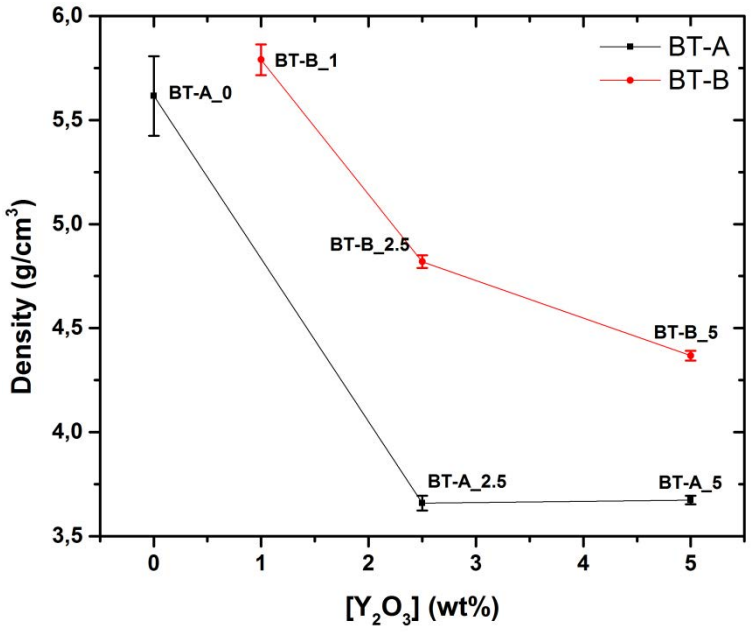

Figure 4.6. *Density of the ceramics sintered in air as a function of Y_2O_3 concentration.*

- **Grain morphology and grain size**

The SEM images of the BT-A_2.5 and BT-A_5 ceramics sintered in air are shown in Fig. 4.7. The mean grain sizes of this ceramics are 0.42 μm (Fig. 4.7.a) and 0.45 μm (Fig. 4.7.b), respectively as seen in Fig. 4.8 where the mean size distribution of both samples is shown. In both micrographs (Fig. 4.7), is possible to see grains with rounded morphology. Although some of them show signs of sintering, they are not really joined as in a dense ceramic. Indeed, the densification of the ceramics was not completed as reflected in the density values (Table 4.4), which could be caused by the high amount of Y_2O_3. Despite this fact, the grains present a homogeneous appearance. About the grain size, the difference among both ceramics is minimum, thus the doping level did not affect it.

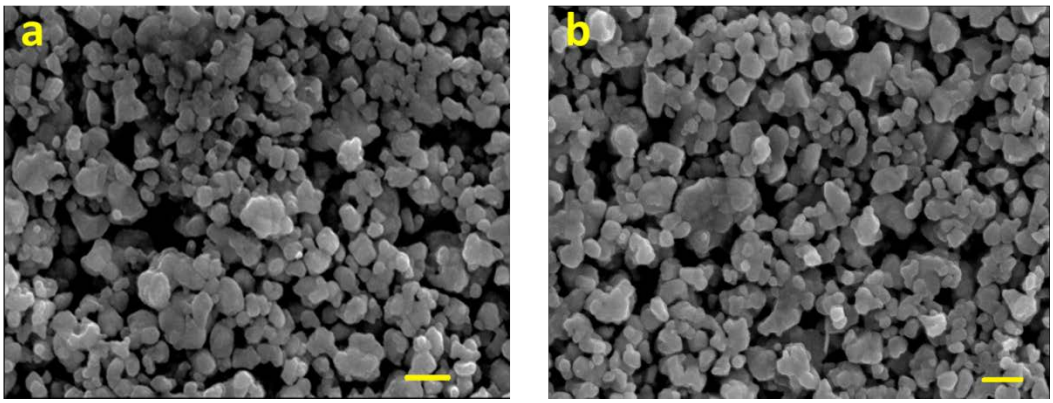

Figure 4.7. *SEM images from (a) BT-A_2.5 and (b) BT-A_5 ceramics sintered in air. Scale bar: 1μm.*

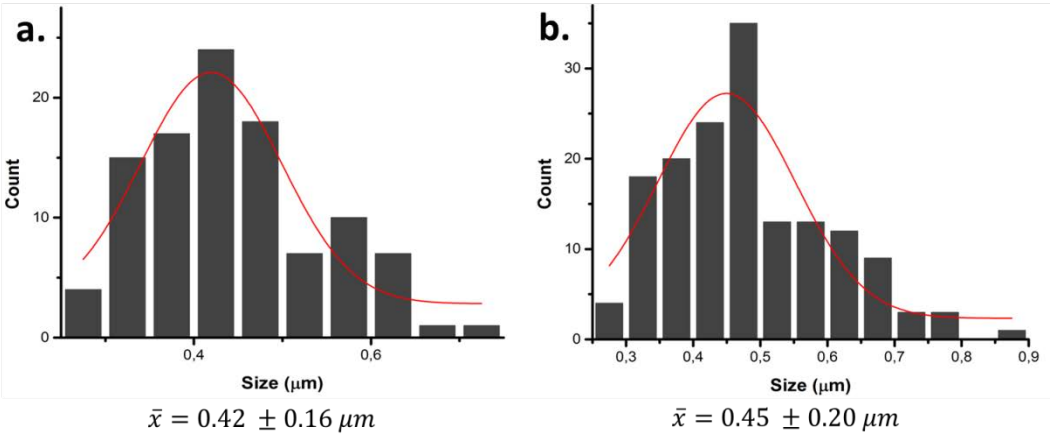

Figure 4.8. *Size distribution of* ***(a)*** *BT-A_2.5 and* ***(b)*** *BT-A_5 ceramics sintered in air.*

The Fig. 4.9.a and Fig. 4.9.b show the SEM images obtained from the BT-B_1 and BT-B_2.5 ceramics sintered in air. The mean grain sizes are 0.44 μm (Fig. 4.10.a) and 0.45 μm (Fig. 4.10.b). The grains have rounded appearance and they are homogeneously distributed. Comparing these ceramics with the ones from BT-A showed in Fig. 4.7, is recognizable that the space among the grains of these BT-B ceramics is lower than the observed in the BT-A micrographs. This is in agreement with higher densification.

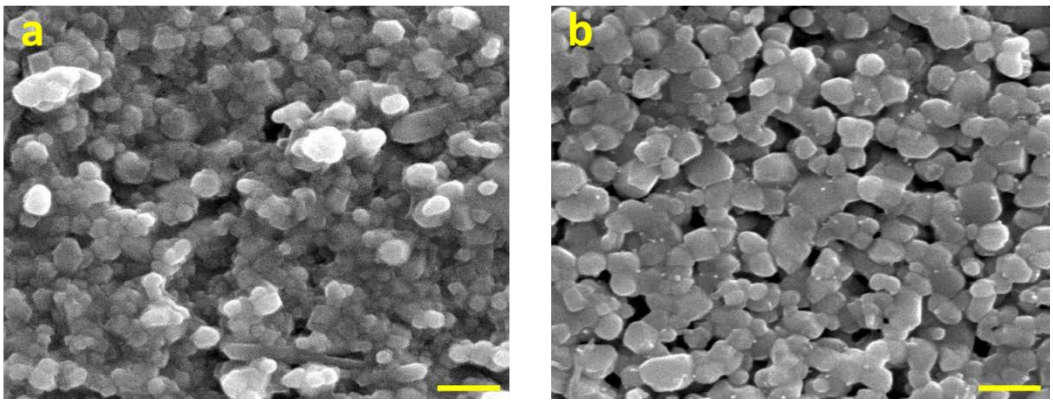

Figure 4.9. *SEM images from (**a**) BT-B_1 and (**b**) BT-B_5 ceramics sintered in air. Scale bar: 1µm.*

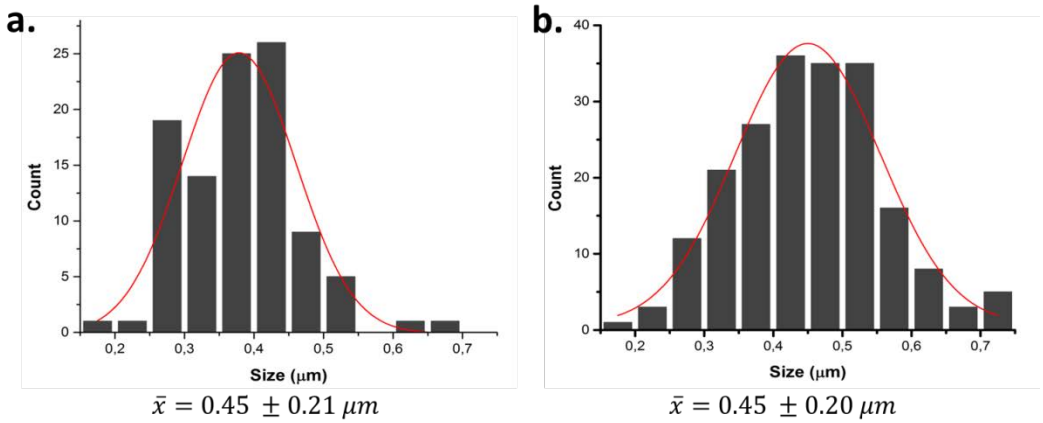

Figure 4.10. *Mean size distribution of (**a**) BT-B_1 and (**b**) BT-B_5 ceramics sintered in air.*

- **Structure and phase composition**

Fig. 4.11 shows the X-ray diffraction patterns of the air-sintered ceramics. The patterns from the ceramics formed from BT-A powders are shown in Fig. 4.11.a.

The BT-A ceramics crystallize in a tetragonal phase, as observed in the Fig. 4.11.a. The BT-A_2.5 and BT-A_5 ceramics however present a decrease of its tetragonality. Y_2O_3 phase is present in BT-A_5 ceramic, this phase was also observed on the BT-A_5 thermally treated powder (Fig. 4.4.a).

The diffraction patterns of ceramics formed from BT-B powder are shown in Fig. 4.11.b. These patterns are in agreeing with a $BaTiO_3$ perovskite and do not show secondary phases. However, it

can be seen the peaks corresponding to the (002) and (200) planes have changed according the dopant level. This can be a reflection of a chemically inhomogeneous composition of the ceramics. This results in the presence of various c/a ratios, which in turn affects the intensity and form of the peaks as well as the splitting of them.

Comparing the XRD patterns of doped ceramics (BT-A_2.5, BT-A_5, BT-B_2.5, and BT-B_5) it is possible to see that the influence of the Y^{3+} over the $BaTiO_3$ structure is greater in the case of the BT-B ceramics. If the peak splitting at 45° - which evidences a tetragonal phase – of both groups of ceramics is compared then it is possible to see that the ones from the BT-B doped ceramics look more joined, being almost like if there was just one broaden peak. It can be considered that the dopant effect on these samples lattices is stronger. This behavior points out the strong interaction between additives and dopants present in the BT-B, which was also reflected in the density values as well as on the microstructure of these ceramics.

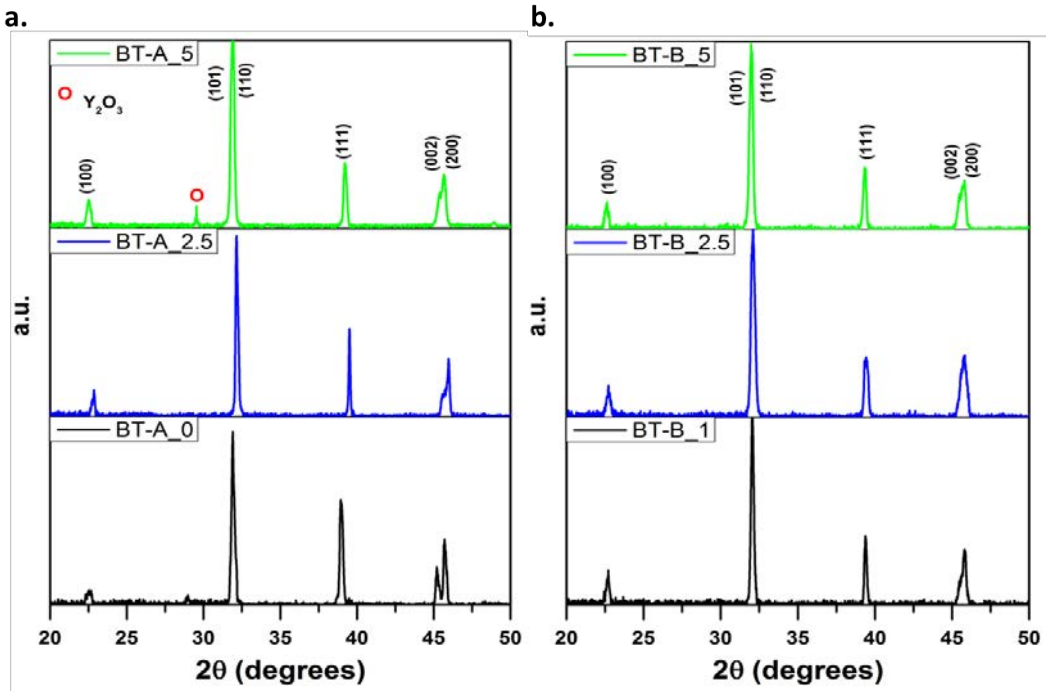

Figure 4.11. *X-ray diffraction patterns of undoped $BaTiO_3$ and 2.5 and 5.0 wt% Y_2O_3-doped $BaTiO_3$ ceramics. Ceramics formed from (**a**) BT-A and (**b**) BT-B, sintered in air.*

A summary of the observations for the thermally treated powders and sintered ceramics in air is shown in Table 4.5.

Table 4.5. *Secondary phases detected in the different powders and ceramics thermally treated and sintered in air, two temperature steps: 1310 °C then 1150 °C 15 h.*

$BaTiO_3$ raw material	**Y_2O_3 wt%**	**Sample ID**	**Secondary phase**	
			Powder (TT)	**Ceramic**
BT-A (reagent-grade)	0	BT-A_0	x	x
	2.5	BT-A_2.5	x	x
	5	BT-A_5	Y_2O_3	Y_2O_3
	20	BT-A_20	Y_2O_3	N.S.
BT-B (commercially formulated)	1	BT-B_1	x	x
	2.5	BT-B_2.5	x	x
	5	BT-B_5	x	x
	20	BT-B_20	$Ba_6Ti_{17}O_{40}$ and Y_2O_3	N.S.

x: no secondary phases were detected. N.S.: not sintered under these conditions.

4.3.2. $BaTiO_3$ ceramics sintered in reducing atmosphere

Ceramics from BT-A, BT-B and BT-C powders were sintered at 1310 °C during 3h, in a reducing atmosphere, and then underwent a re-oxidizing process. The ceramics sintered under this protocol were BT-A (A_0, A_1.5, A_2, A_2.5, A_5, A_20), BT-B (B_1, B_1.5, B_2, B_2.5, B_5, B_20), and BT-C (C_1, C_1.5, C_2).

With the purpose to detect differences among sintering steps (sintering in reducing atmosphere and re-oxidizing under a weekly oxidizing atmosphere), ceramics from each group were separated to perform analyses to both conditions, denominating them as “sint” and “reox” respectively. SEM analyses of some of the ceramics were also performed. In order to follow the dopant behavior into

the BT-lattice, and detect any structural change during the different treatments, the main tool used in this work is the X-Ray Diffraction analysis.

4.3.2.1. $BaTiO_3$ ceramics issued from BT-A powders with Y_2O_3 content from 0 to 20 wt%.

- **Density**

The effect of the dopant level was also observed under these sintering conditions. In the Table 4.6 are given the density values of BT-A ceramics, as well as in the Fig. 4.12. The densification for doped ceramics is lower and the values do not change significantly among the doped ceramics. With these ceramics, the effect of the Y_2O_3 content over their densification is noticeable, finding values between 60 – 75 % for the doped ceramics.

Table 4.6. *Density of BT-A ceramics sintered under reducing atmosphere and 1310 °C.*

$BaTiO_3$ raw material	**[Y_2O_3] (wt%)**	**Sample ID**	**Density (g/cm^3)**
BT-A (reagent grade)	0	BT-A_0	5.70 ± 0.05
	1	BT-A_1	4.51 ± 0.17
	1.5	BT-A_1.5	3.74 ± 0.04
	2	BT-A_2	3.74 ± 0.06
	2.5	BT-A_2.5	4.09 ± 0.09
	5	BT-A_5	4.29 ± 0.05
	20	BT-A_20	4.19 ± 0.06

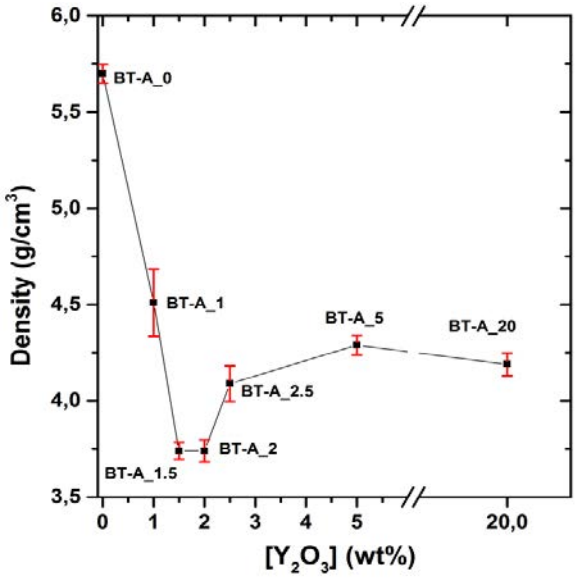

Figure 4.12. *Density of BT-A ceramics sintered in a reducing atmosphere as a function of Y_2O_3 content.*

Regarding the possible differences between the density of the ceramics with same dopant level sintered in air and the ones sintered in a reducing atmosphere, in Fig. 4.13 is shown a comparison of the values. For the ceramics BT-A_0, BT-A_2.5, and BT-A_5 sintered under reducing atmosphere the density is higher than the one obtained when sintered in air. The density of the undoped ceramics is about the same under both sintering processes. Meanwhile, the BT-A_2.5 and BT-A_2.5 ceramics sintered in reducing conditions are 7% and 10% denser than the ones sintered in air.

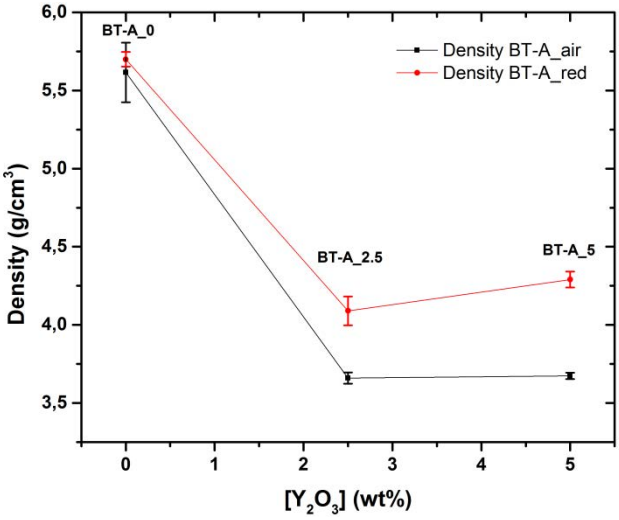

Figure 4.13. *Comparison of the BT-A ceramics density sintered using air or reducing atmosphere as a function of Y_2O_3 content.*

- **Grain morphology and grain size**

In the Fig. 4.14 the SEM analyses performed to BT-A ceramics doped with 5 and 20 wt% Y_2O_3 are shown. In this case, the Fig. 4.14.a correspond to the BT-A_5 ceramic that was taken out before the re-oxidizing step (BT-A_5_sint) and the Fig. 4.14.b to the one that passed through it (BT-A_5_reox). The mean grain size distribution of these ceramics is 0.43 μm and 0.41 μm, respectively. It means that apparently the size is not affected by the re-oxidizing step. Neither is the morphology, since their outward appearance is similar, the grains have angular borders and a smooth surface. The BT-A_20_sint ceramic, shown in Fig. 4.14.c has a mean grain size of 0.44 μm, which is pretty close to the BT-A_5 ceramics. About the morphology of this sample, the image (Fig. 4.14.c) allows seeing more angular-bordered grains.

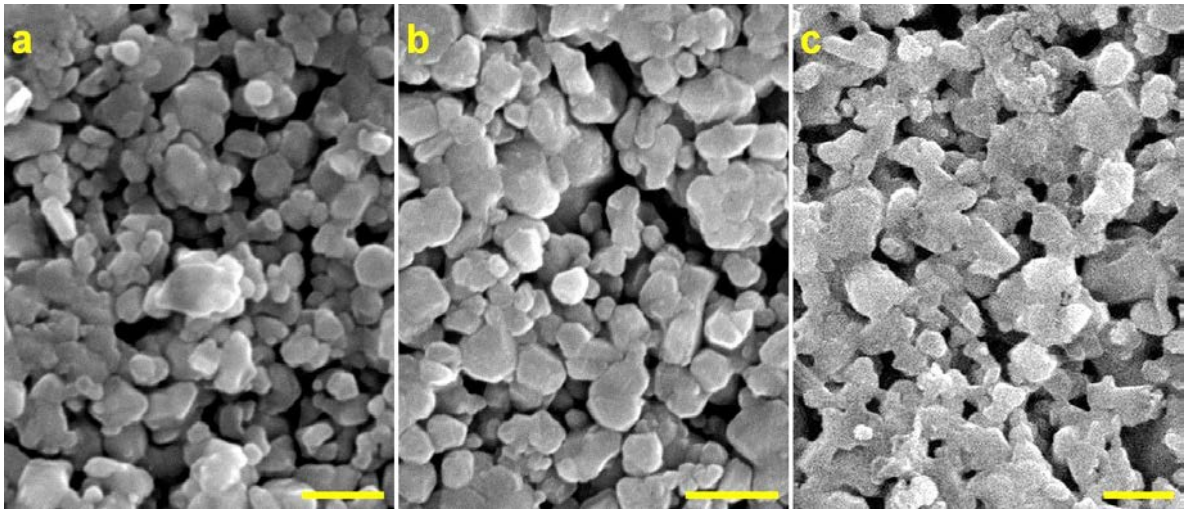

Figure 4.14. *SEM images from BT-A ceramics sintered in reducing atmosphere. (**a**) BT-A_5_sint, (**b**) BT-A_5_reox, and (**c**) BT-A_20_sint. Scale bar: 1μm.*

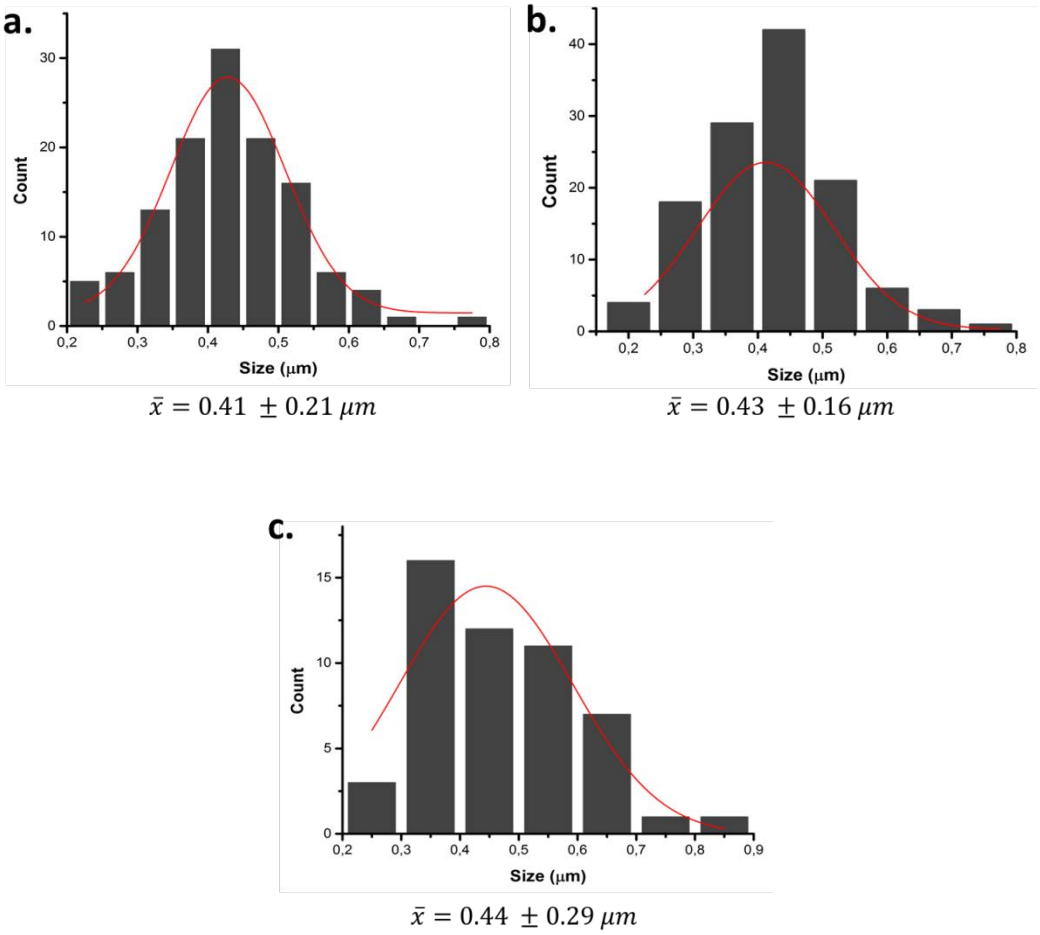

Figure 4.15. *Size distribution of BT-A ceramics sintered in reducing atmosphere. (**a**) BT-A_5_sint, (**b**) BT-A_5_reox, and (**c**) BT-A_20_sint.*

- **Structure and phase composition**

The XRD patterns of undoped and doped ceramics, sintered and re-oxidized, formed from the BT-A powders are shown in Fig. 4.16. Diffractograms from BT-A undoped ceramics are shown in Fig. 4.16.a, and from 1 wt% Y_2O_3-doped BT-A ceramics in Fig. 4.16.b. In both figures, a tetragonal perovskite structure (JCPDS: 89-1428) is observed in all cases. No traces of secondary phases can be detected, either in Fig. 4.16.a or Fig. 4.16.b. There is no structural evolution from the powder to the final dense ceramics or differences among the sintered and re-oxidized ceramics.

In the case of the 1.5 and 2 wt% Y_2O_3-doped BT-A ceramics (Fig. 4.16.c and Fig. 4.16.d), it is possible to say that the main phase remains tetragonal. The peaks corresponding to the planes (002) and (200) get closer to each other when Y_2O_3 concentration is 1.5 wt%, as seen in Fig. 4.16.c. It indicates a decrease in the tetragonality of the BT lattice. For samples with Y_2O_3 concentration higher than 1.5 wt% (Fig. 4.16.d to 4.16.g) those peaks get even more joined, i.e. when the dopant concentration increases, the tetragonality of the samples is decreased. For the 5 and 20 wt% Y_2O_3-doped BT-A ceramics (Fig. 4.16.f and Fig. 4.16.g), it could be even said that they seem merged, because the decrease of intensity and apparent lack of split. The change in the crystalline phase results from the Y^{3+} ions incorporation into the BT lattice (Kim et al., 2008; Wang et al., 2014a; Wang et al., 2014b). However, the incorporation of dopants results in a non-homogeneous distribution of these in the BT matrix during the sintering process. With the obtained patterns it is not possible to discriminate the c/a ratios corresponding to the range of 2θ that lead to the broadening of the peaks. Despite the changes in the lattice, the position of the BT planes was not shifted.

Moreover, in Fig. 4.16.d an additional peak at 2θ = 30.6° is noticed both, sintered and reoxidized ceramics, which corresponds to the cubic pyrochlore compound $Y_2Ti_2O_7$ (JCPDS: 42-0413). This compound has also been evidenced before by other authors like Belous et al. (2008), Yoon et al. (2007), and Zhang et al. (2016). The diffractograms of the 2.5 wt% Y_2O_3-doped BT-A ceramics (Fig 4.16.e.) also reveal the presence of a secondary phase. A peak of weak intensity at 29.5° is detected and identified as the yttrium titanate Y_2TiO_5 (JCPDS: 40-0795) phase. The BT-A_5 ceramics (Fig 4.16.f.) present peaks that correspond to the phases Y_2O_3 and $Y_2Ti_2O_7$.

Finally, the XRD analyses of the BT-A_20 ceramics (Fig. 4.16.g) revealed the presence of secondary phases as well. Nonetheless, there are some differences among the BT-A_20_sint and BT-A_20_reox patterns. In the BT-A_20_sint diffraction pattern, peaks corresponding to Y_2TiO_5 and $Y_2Ti_2O_7$ are observed. On the other hand, the BT-A_20_reox presents the $Y_2Ti_2O_7$ along with

Y_2O_3. The differences found between the reduced and re-oxidized ceramics with respect to their secondary phases can be due to the formation of some Ti^{4+} to Ti^{3+} during the sintering and with the post-sintering annealing process it is reverted, leaving less available to form secondary phases. Also, the lattice distortion and the formation of additional phases are related with the incorporation of Y^{3+} ions into the BT-lattice. Since the Y^{3+} ion has an intermediate size between Ba^{2+} and Ti^{4+} ions, it can occupy either A- or B-site in the BT crystal structure. In principle, Y^{3+} will replace first Ba^{2+} sites, but then if the activity increases on this site, it also replaces Ti^{4+} ions, which could have contributed to the formation of Ti-rich precipitates. Another factor that could lead to the formation of these secondary phases is that the solubility limit of Y_2O_3 in BT has been reached.

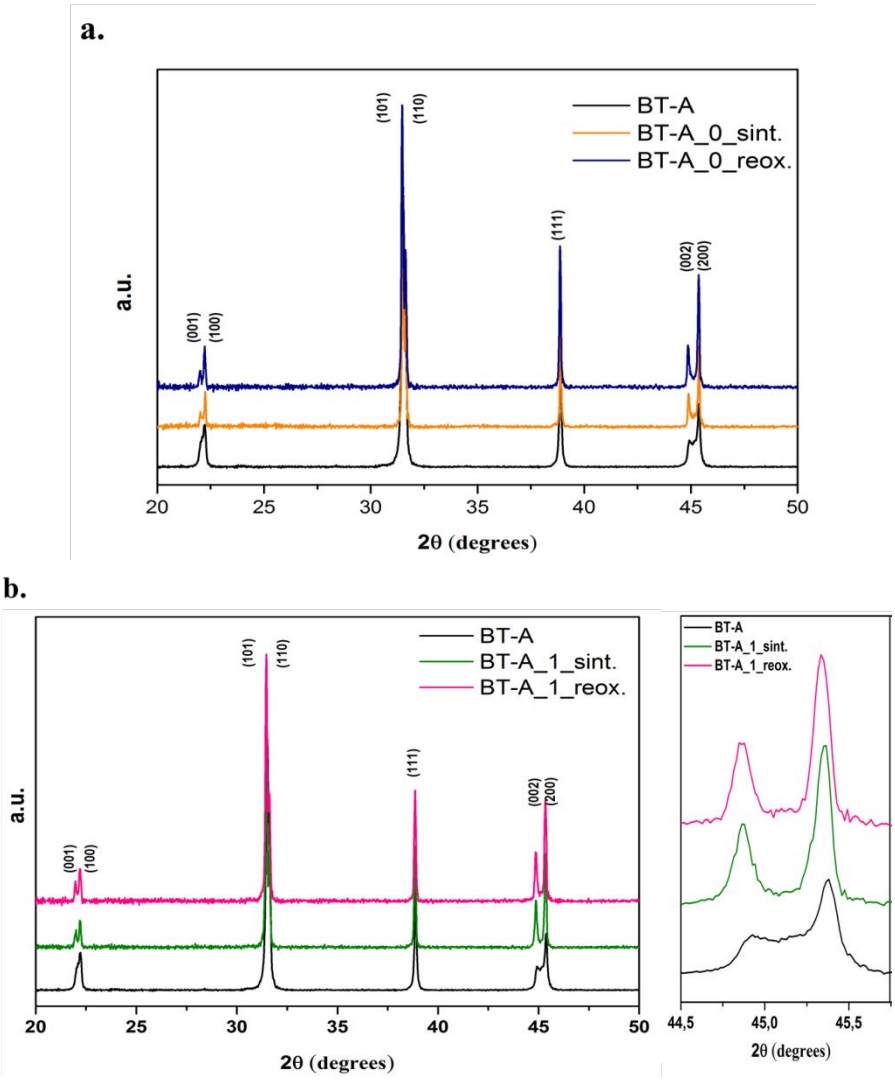

c.

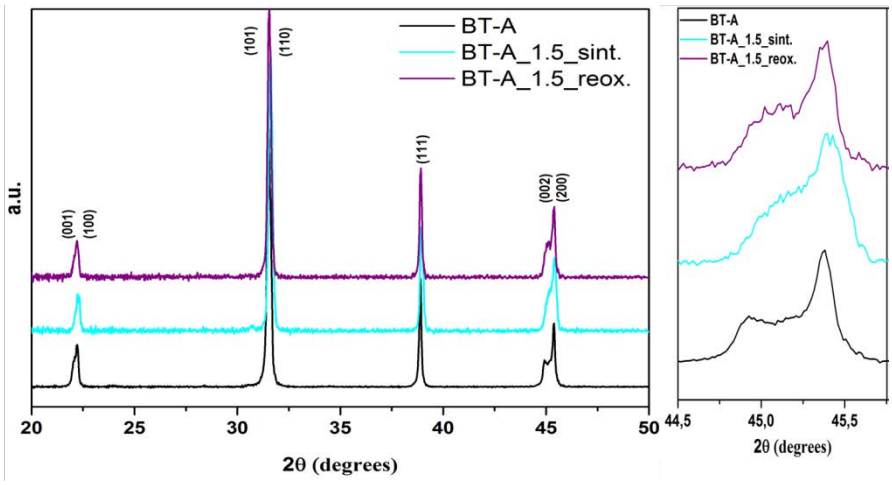
BT-A
BT-A_1.5_sint.
BT-A_1.5_reox.
(001)
(100)
(101)
(110)
(111)
(002)
(200)
a.u.
20
25
30
35
40
45
50
2θ (degrees)
44,5
45,0
45,5

d.

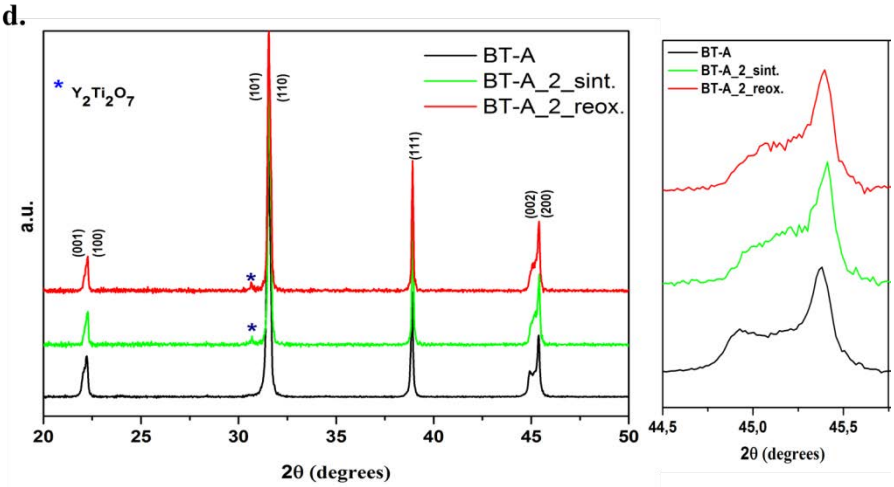
* $Y_2Ti_2O_7$
BT-A
BT-A_2_sint.
BT-A_2_reox.
(001)
(100)
(101)
(110)
(111)
(002)
(200)
a.u.
20
25
30
35
40
45
50
2θ (degrees)
44,5
45,0
45,5

e.

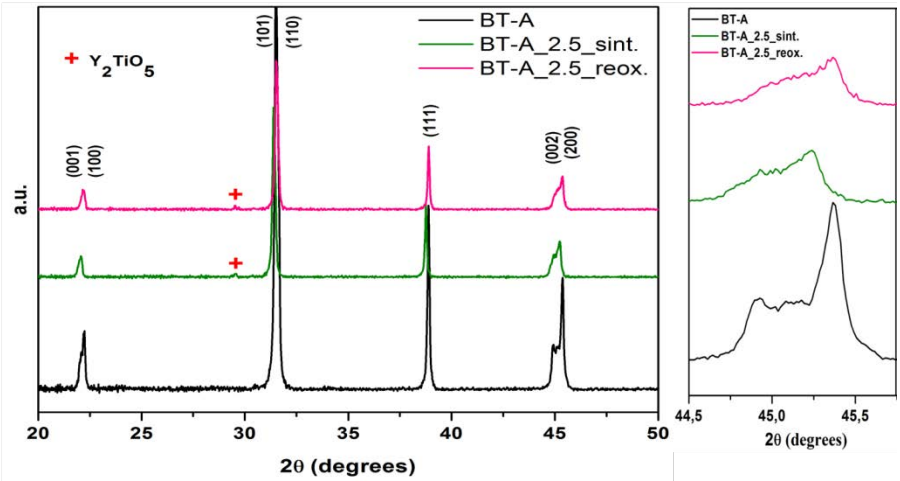
+ Y_2TiO_5
BT-A
BT-A_2.5_sint.
BT-A_2.5_reox.
(001)
(100)
(101)
(110)
(111)
(002)
(200)
a.u.
20
25
30
35
40
45
50
2θ (degrees)
44,5
45,0
45,5

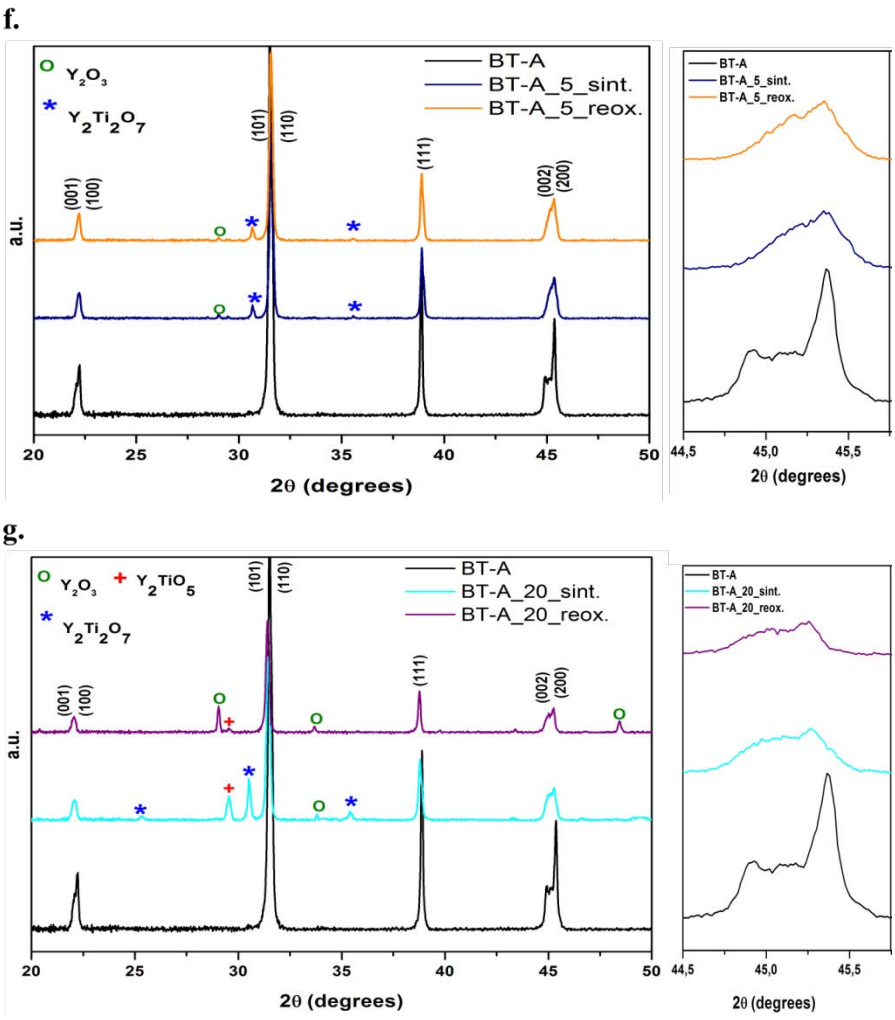

Figure 4.16. *XRD patterns of BT-A powder and ceramics sintered in reducing atmosphere and re-oxidized. Lateral enlargements of zone around 45° are presented for doped samples.*

A summary of the principal observations from the XRD analyses performed on BT-A ceramics sintered in reducing conditions is presented in Table 4.7.

Table 4.7. *Secondary phases detected in BT-A ceramics sintered in reducing atmosphere at 1310 °C.*

$BaTiO_3$ raw material	**Y_2O_3 wt%**	**Sample ID**	**Secondary phases**
BT-A (reagent-grade)	0	BT-A_0	x
	1	BT-A_1	x
	1.5	BT-A_1.5	x
	2	BT-A_2	$Y_2Ti_2O_7$
	2.5	BT-A_2.5	Y_2TiO_5
	5	BT-A_5	Y_2O_3; $Y_2Ti_2O_7$
	20	BT-A_20	sint. ceramic: Y_2O_3; $Y_2Ti_2O_7$; Y_2TiO_5. reox. ceramic: Y_2O_3; Y_2TiO_5.

x: no secondary phases were detected.

4.3.2.2. $BaTiO_3$ ceramics issued from BT-B powders with Y_2O_3 content from 1 to 20 wt%.

- **Density**

The density of the ceramics produced from the BT-B formulated powder, is shown in the Table 4.8. The density increases slightly when BT-B ceramics are doped with 1.5 and 2 wt% of Y_2O_3, then from 2.5 up to 20 wt% it decreases rapidly. The variation of density with Y_2O_3 content is plotted in Fig. 4.18, where it is seen that the density is clearly lower when Y_2O_3 level is higher than 2 wt%. The density values of BT-B ceramics (Table 4.8) are about 20% higher than the ones from the BT-A ceramics (Table 4.6). This was expected since the BT-B contains sintering additives that contribute to the improvement of the densification. In this case, the BT-B contains SiO_2 (0.30 wt%), which has been reported to contribute to the improvement of the densification process (Liu, & Roseman, 1999; Wu, Wang, McCauley, Chu, & Lu, 2007).

Table 4.8. *Density of BT-B ceramics sintered in reducing atmosphere at 1310 °C.*

$BaTiO_3$ raw material	**$[Y_2O_3]$ (wt%)**	**Sample ID**	**Density (g/cm^3)**
BT-B (commercially formulated)	1	BT-B_1	5.45 ± 0.07
	1.5	BT-B_1.5	5.56 ± 0.04
	2	BT-B_2	5.59 ± 0.05
	2.5	BT-B_2.5	5.03 ± 0.10
	5	BT-B_5	4.97 ± 0.04
	20	BT-B_20	4.84 ± 0.10

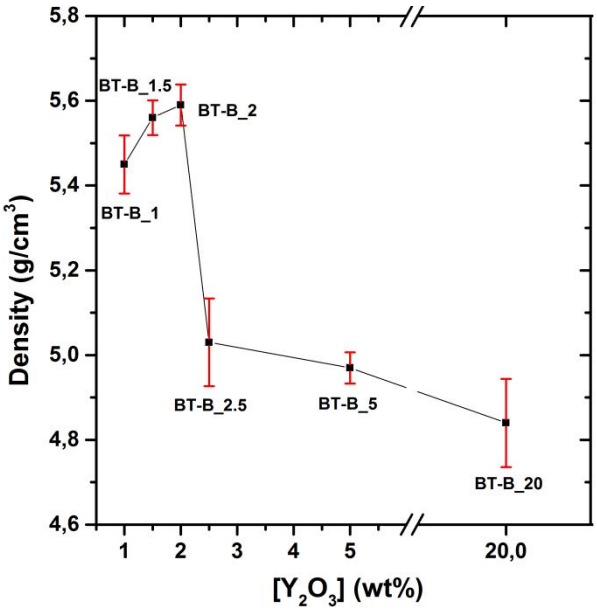

Figure 4.17. *Density of BT-B ceramics sintered in a reducing atmosphere as a function of Y_2O_3 content.*

A contrast between the density results obtained for the ceramics BT-B_1, BT-B_2.5, and BT-B_5 sintered under reducing atmosphere (Table 4.8) and the ones sintered in air (Table 4.6) is presented in the Fig. 4.18. This figure shows that the density of the ceramics sintered under the different atmospheres is different. For the BT-B_1 ceramics, the one sintered in air has higher density, but for the ceramics above this dopant level, the ones sintered in reducing conditions present higher

densities. The BT-B_1 fired in air is 6 % denser than the BT-B_1 fired in reducing atmosphere. While BT-B_2.5 and BT-B_5 sintered in air are about 3 % and 10 % respectively less dense than those sintered in reducing atmosphere.

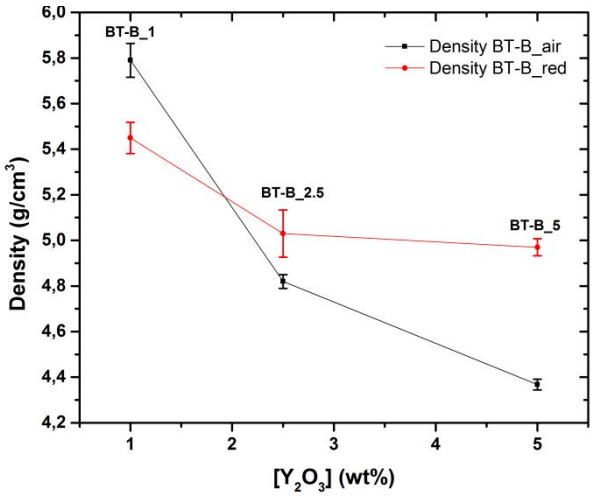

Figure 4.18. *Comparison of the BT-B ceramics density sintered using air or reducing atmosphere as a function of Y_2O_3 content.*

- **Grain morphology and grain size**

SEM images of BT-B doped-ceramics are shown in Fig. 4.19. In this case, the three analyzed ceramics have different Y_2O_3 concentration and are sintered, i.e. without the re-oxidation step. The mean grain distribution sizes can be observed in Fig. 4.20. It is roughly equal for the three samples. The value for BT-B_1.5_sint is 0.43 μm, 0.42 μm for BT-B_2_sint, and 0.41 μm for the BT-B_5_sint (Fig. 4.20). Thus, the grain size does not significantly change with the increase of Y_2O_3 content. Indeed, the morphology of the grains is similar between the three samples, i.e., the three of them present agglomerations of spherical grains and also some grains with a more angular-bordered form (Fig. 4.19).

Despite the differences in the density values of these three ceramics, the SEM images show that they have a similar morphology and surface.

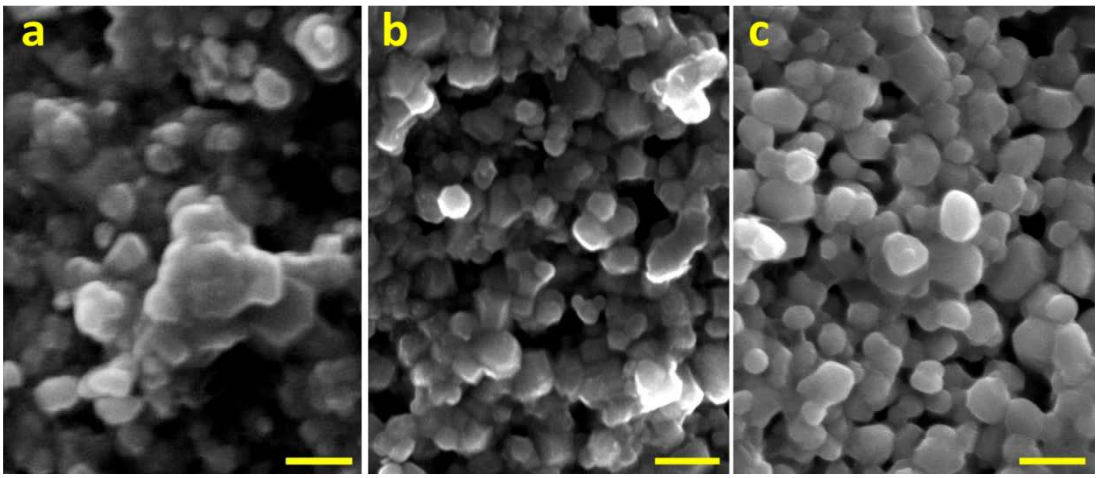

Figure 4.19. *SEM images from BT-B ceramics sintered in reducing atmosphere. (**a**) BT-B_1.5_sint, (**b**) BT-B_2_sint, and (**c**) BT-B_5_sint. Scale bar: 1 µm.*

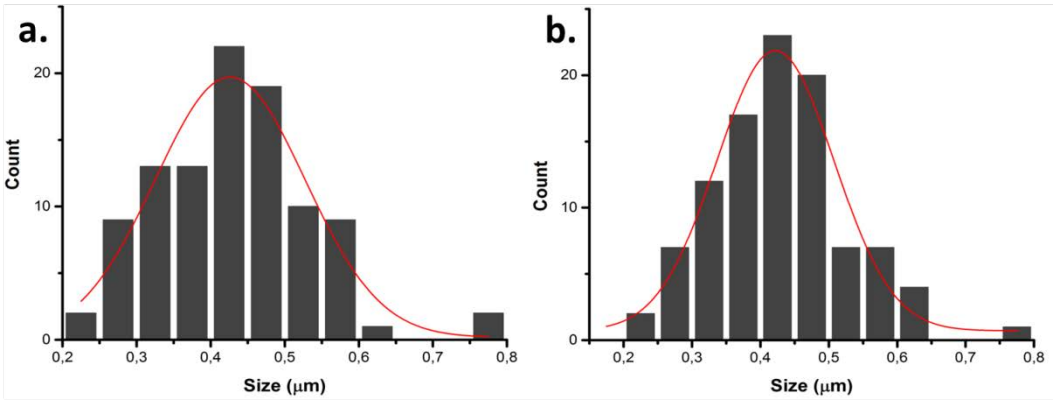

$\bar{x} = 0.43 \pm 0.20\ \mu m$ $\bar{x} = 0.42 \pm 0.17\ \mu m$

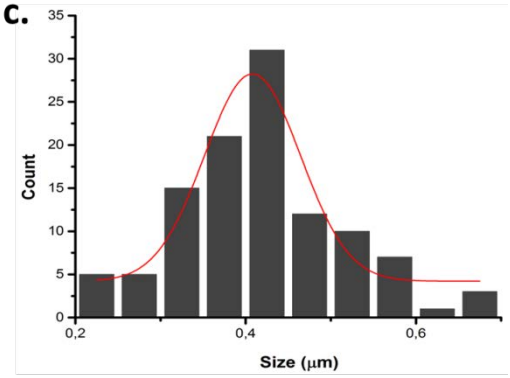

$\bar{x} = 0.41 \pm 0.11\ \mu m$

Figure 4.20. *Mean size distribution of BT-B ceramics sintered in reducing atmosphere. (**a**) BT-B_1.5_sint., (**b**) BT-B_2_sint., and (**c**) BT-B_5_sint.*

- **Structure and phase composition**

X-ray diffraction patterns corresponding to the ceramics prepared from powder BT-B doped with Y_2O_3 from 1 to 20 wt%, and sintered under industrial conditions are shown in Fig. 4.21.

As shown in Fig. 4.21.a for the lowest Y_2O_3 content (BT-B_1) there is no difference between the structure of the powder and sintered ceramics. The crystalline structure coincides with the tetragonal perovskite phase. All the ceramics with Y_2O_3 level from 1.5 wt% up to 20 wt% also crystallize in the tetragonal structure. The c/a ratio decreases affecting the tetragonality as seen in Fig. 4.21.b-f. The characteristic split of the planes (002) and (200) decreases with the increment of Y_2O_3 doping. The intensity of the peaks is also affected by the amount of Y_2O_3 they look almost like just one broaden peak.

These variations in the tetragonality can also be related with the secondary phases detected in the concerned ceramics. In the case of BT-B_1.5 and BT-B_2.0 (Fig. 4.21.b and 4.21.c), the $Y_2Ti_2O_7$ phase appears in the sintered ceramics and remains after the re-oxidation treatment. In the BT-B_2.5, the Y_2TiO_5 phase is detected in both, sintered and re-oxidized ceramics (Fig. 4.21.d). Finally, for the BT-B_5 and BT-B_20 ceramics, the $Ba_6Ti_{17}O_{40}$ phase was identified (Fig. 4.18.e and Fig. 4.18.f). Also, in the BT-B_20 ceramics, peaks corresponding to the Y_2O_3 phase are observed.

The precipitation of these different phases with respect to the Y_2O_3 concentration in the samples can be given by the interaction among the BT-B matrix and the additives and dopants it contains; i.e., the Y_2O_3 added to reach the specified doping concentrations.

In the case of the BT-B ceramics, it must be reminded that the raw powder contains a high content of Mg^{2+} (0.29 %), while the BT-A being reagent grade is considered practically Mg-free. The formulated powder BT-C has a ratio of Mg^{2+} of 0.0062 %. Since the Mg^{2+} can substitute Ti^{4+}-sites in the BT lattice (Wang et al., 2014a) it leads to the Ba-sites replacement by Y^{3+} until the saturation

in these sites is reached. Then the subsequent Y^{3+} added will enter into the Ti^{4+}-sites. The free Ti^{4+} in the system will increase the possibility of secondary phases rich in Ti^{4+} formation.

The BT-A and BT-B 20 wt% Y_2O_3-doped ceramics present different secondary phases. In BT-A_20 XRD patterns $Y_2Ti_2O_7$ and Y_2TiO_5 are observed (Fig. 4.16.g), while in the ones from BT-B_20 ceramics the $Ba_6Ti_{17}O_{40}$ and Y_2O_3 secondary phases were detected (Fig. 4.20.f). However, is seen that the higher the Y^{3+} dopant level, the higher is the possibility of Ti-rich phases formation.

The raw powder composition must be taken into account at the time of discuss these differences. Since chemical composition of the powders is different, the interactions of the Y_2O_3 dopant are not the same with both BT matrixes. As aforesaid, the BT-B additives play a role on the final structural and microstructural ceramics properties.

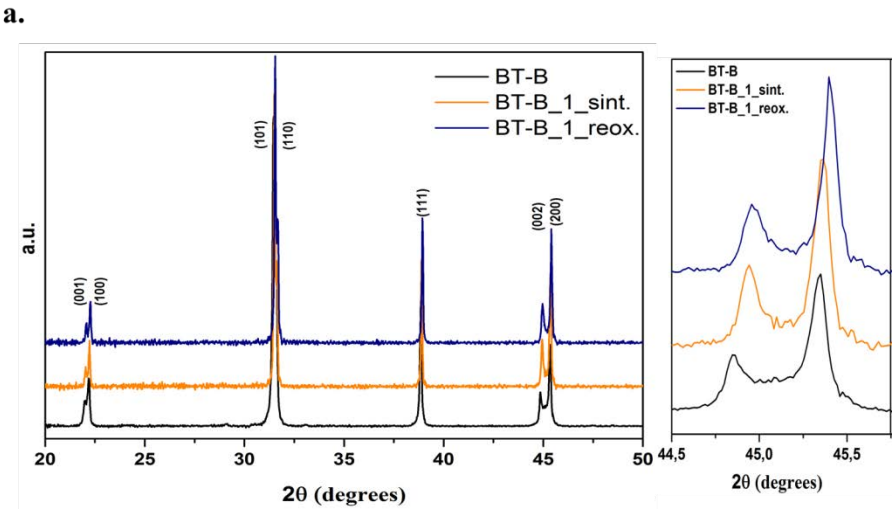

b.

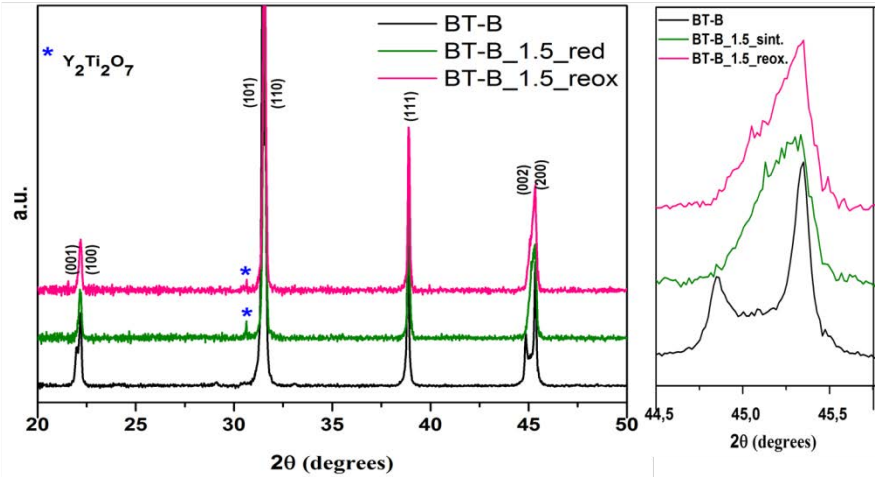
* $Y_2Ti_2O_7$
BT-B
BT-B_1.5_red
BT-B_1.5_reox
(001)
(100)
(101)
(110)
(111)
(002)
(200)
a.u.
2θ (degrees)
BT-B
BT-B_1.5_sint.
BT-B_1.5_reox.

c.

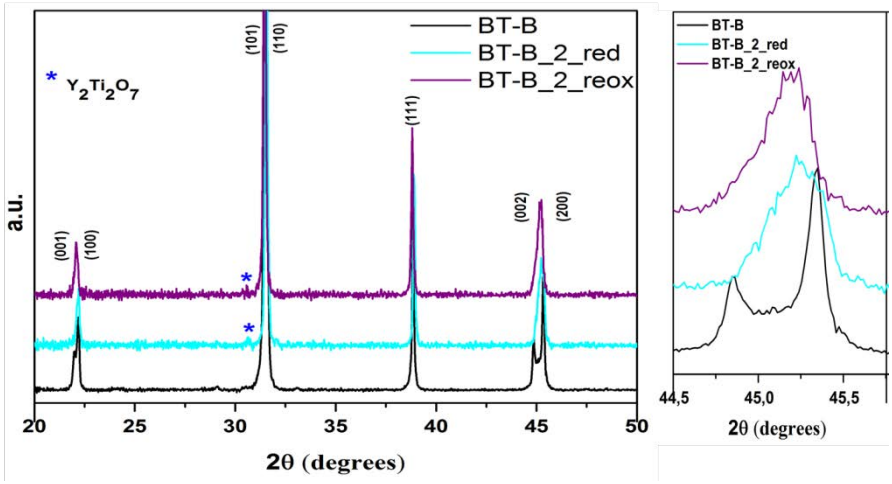
* $Y_2Ti_2O_7$
BT-B
BT-B_2_red
BT-B_2_reox
(001)
(100)
(101)
(110)
(111)
(002)
(200)
a.u.
2θ (degrees)
BT-B
BT-B_2_red
BT-B_2_reox

d.

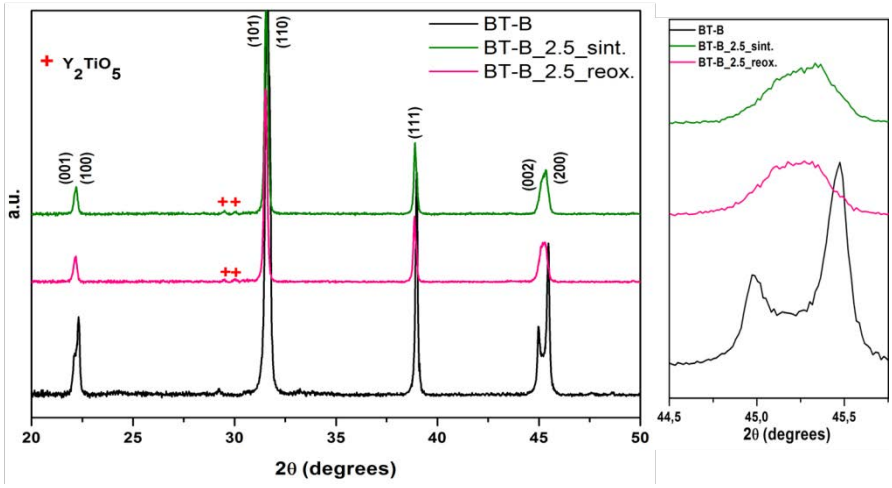
+ Y_2TiO_5
BT-B
BT-B_2.5_sint.
BT-B_2.5_reox.
(001)
(100)
(101)
(110)
(111)
(002)
(200)
a.u.
2θ (degrees)
BT-B
BT-B_2.5_sint.
BT-B_2.5_reox.

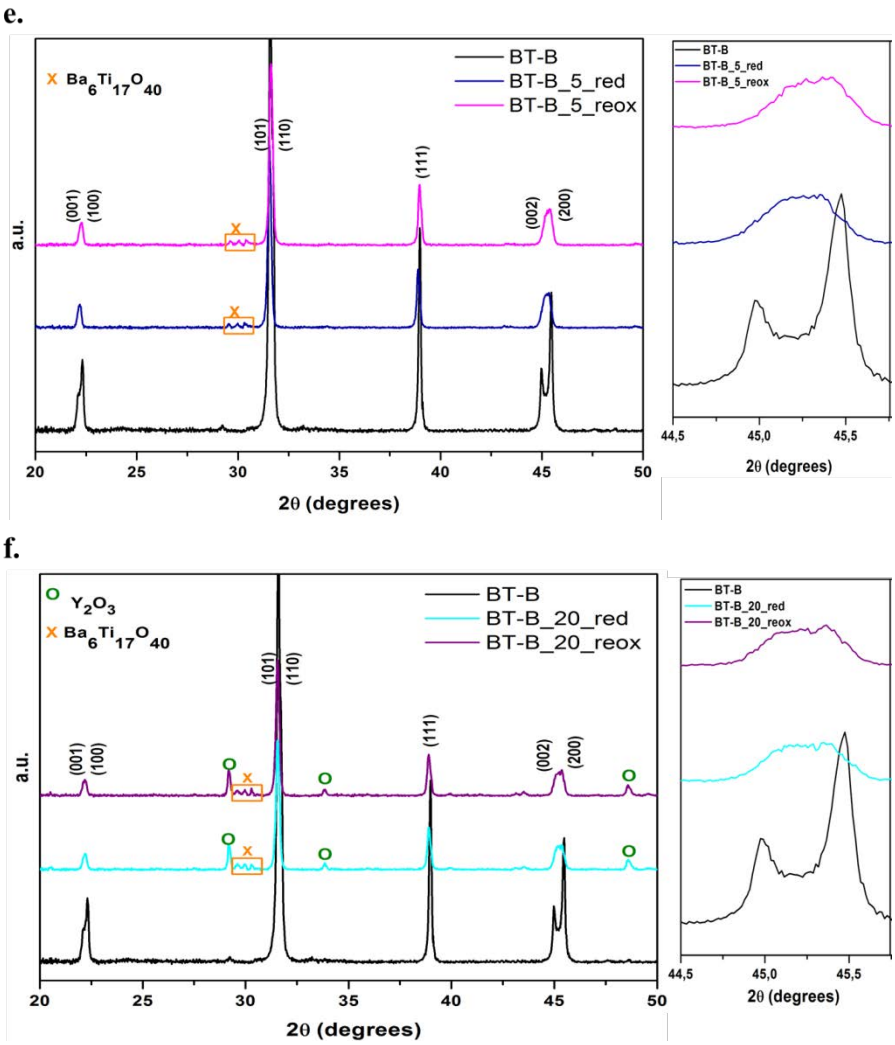

Figure 4.21. *XRD patterns of BT-B powder and ceramics sintered in reducing atmosphere and re-oxidized. Lateral enlargements of zone around 45° are presented.*

A summary of the principal observations from the XRD analyses performed on BT-B ceramics sintered in reducing conditions is presented in Table 4.9.

Table 4.9. *Secondary phases detected in BT-B ceramics sintered in reducing atmosphere at 1310 °C.*

$BaTiO_3$ raw material	**Y_2O_3 wt%**	**Sample ID**	**Secondary phase**
BT-B (commercially formulated)	1	BT-B_1	x
	1.5	BT-B_1.5	$Y_2Ti_2O_7$
	2	BT-B_2	$Y_2Ti_2O_7$
	2.5	BT-B_2.5	Y_2TiO_5
	5	BT-B_5	$Ba_6Ti_{17}O_{40}$
	20	BT-B_20	Y_2O_3; $Ba_6Ti_{17}O_{40}$

x: no secondary phases were detected.

4.3.2.3. $BaTiO_3$ ceramics issued from BT-C powders with Y_2O_3 content: 1 to 2 wt%.

- **Density**

These ceramics discussed in this section are formed from another formulated powder. The composition of BT-C is different from the BT-B (Table 4.1). The main differences attending to the interests of next discussions are on the amount of Ca, Si, and Mg present in these powders, which are higher in the BT-B. A reminder of the concentration of these components in the formulated powders is presented in Table 4.10.

Table 4.10. *Chemical composition of $BaTiO_3$ formulated powders.*

	Ba	**Ti**	**Y**	**Ca**	**Si**	**Mg**
BT_B	54.67	19.17	1.05	1.34	0.30	0.29
BT_C	53.86	18.85	1.05	0.57	0.17	0.006

Values are given in wt%.

The density values of BT-C ceramics are presented in the Table 4.11 and Fig. 4.22. The densification for these ceramics is above 90%. Although the marginally difference in the density, it was equal for BT-C_1.5 and BT-C_2, and lower for BT-C_1.

Comparing the density values of the BT-C and BT-B ceramics with the same Y_2O_3 concentration (BT-B_1, BT-B_1.5, and BT-B_2), is possible to see that they are quite similar, being the ones of BT-B ceramics just about 1 % lower. This means that despite the difference in the SiO_2 content (being the double for the BT-B powder) the densification was not improved or diminished by it. This leads to consider that is not just the SiO_2 which exerts an effect over the densification of BT-doped ceramics, but also the rest of additives present in the BT-formulated powders composition.

Table 4.11. *Density of BT-C ceramics sintered in reducing atmosphere at 1310 °C.*

$BaTiO_3$ raw material	**$[Y_2O_3]$ (wt%)**	**Sample ID**	**Density (g/cm^3)**
BT-C (commercially formulated)	1	BT-C_1	5.48 ± 0.05
	1.5	BT-C_1.5	5.60 ± 0.05
	2	BT-C_2	5.60 ± 0.04

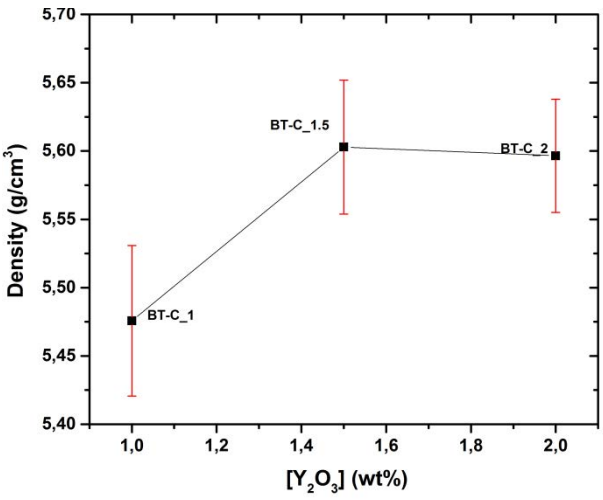

Figure 4.22. *Density of BT-C ceramics sintered in a reducing atmosphere as a function of Y_2O_3 content.*

- **Grain morphology and grain size**

SEM images of the ceramics formed with BT-C powder doped with 1.5 and 2 wt% Y_2O_3 are shown in Fig. 4.23.a and 4.23.b, respectively. The size distribution of these samples is shown in Fig. 4.23. Their mean grain sizes are 0.46 and 0.48 µm. The yttrium oxide content does not seem to affect the morphology or the grain size. Merged grains with angular borders are observed and no porosity is visible. Ceramics prepared from BT-C are definitively more densified than the ones with the same Y^{3+} content issued from BT-B powders.

With respect to the mean size of BT-C_1.5_sint and BT-C_2_sint (Fig. 4.24) compared with the BT-B_1-5_sint and BT-B_2_sint (Fig. 4.19), the difference among them is hardly noticeable regarding the obtained values and the respective incertitude.

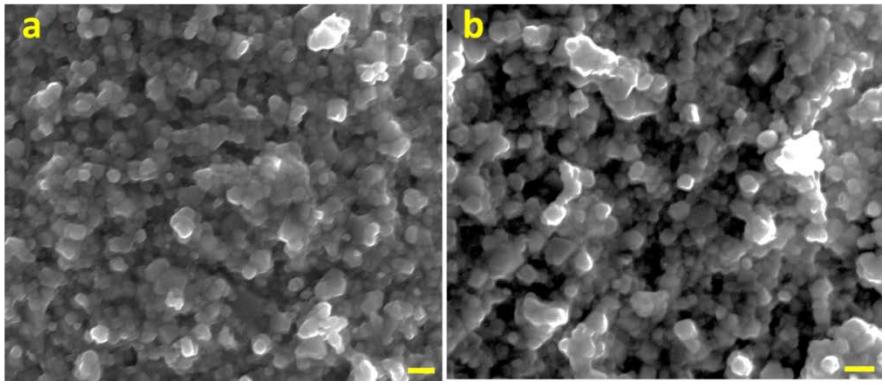

Figure 4.23. *SEM images from BT-C ceramics sintered in reducing atmosphere. (**a**) BT-C_1.5_sint, (**b**) BT-B_2_sint. Scale bar: 1 µm.*

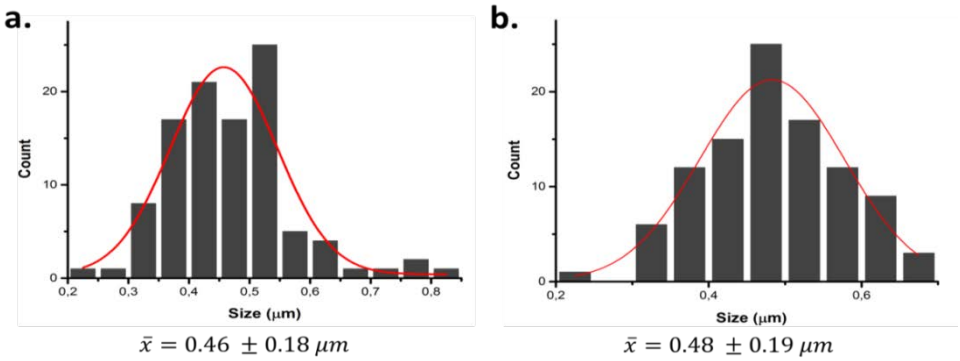

Figure 4.24. *Size distribution of BT-C ceramics sintered in reducing atmosphere. (**a**) BT-C_1.5_sint., and (**b**) BT-C_2_sint.*

- **Structure and phase composition**

In the BT-C case, the doping concentrations are 1, 1.5 and 2 wt% Y_2O_3. The BT-C_1 ceramics (Fig. 4.25.a) crystallize in the tetragonal phase. No secondary phase or phase transitions are observed. The structure does not vary with the post-sintering conditions. In the case of BT-C_1.5 (Fig. 4.25.b) and BT-C_2 (Fig. 4.25.c) ceramics, the XRD analyses evidence the decrease of the tetragonality. The enlargements of peaks around 45° show how the (002) peak becomes less intense and seem to be joined with the (200).

The pyrochlore $Y_2Ti_2O_7$ is detected in BT-C_1.5 and BT-B_2 ceramics. This secondary phase is also observed in the X-ray diffraction patterns of the ceramics issued from BT-B powders with same dopant concentrations. Also, it is worth to mention that apparently the presence of the $Y_2Ti_2O_7$ phase improves the densification (Fig. 4.17 and Fig. 4.22) probably because it has a lower melting point (1580 °C) than $BaTiO_3$ (1625 °C).

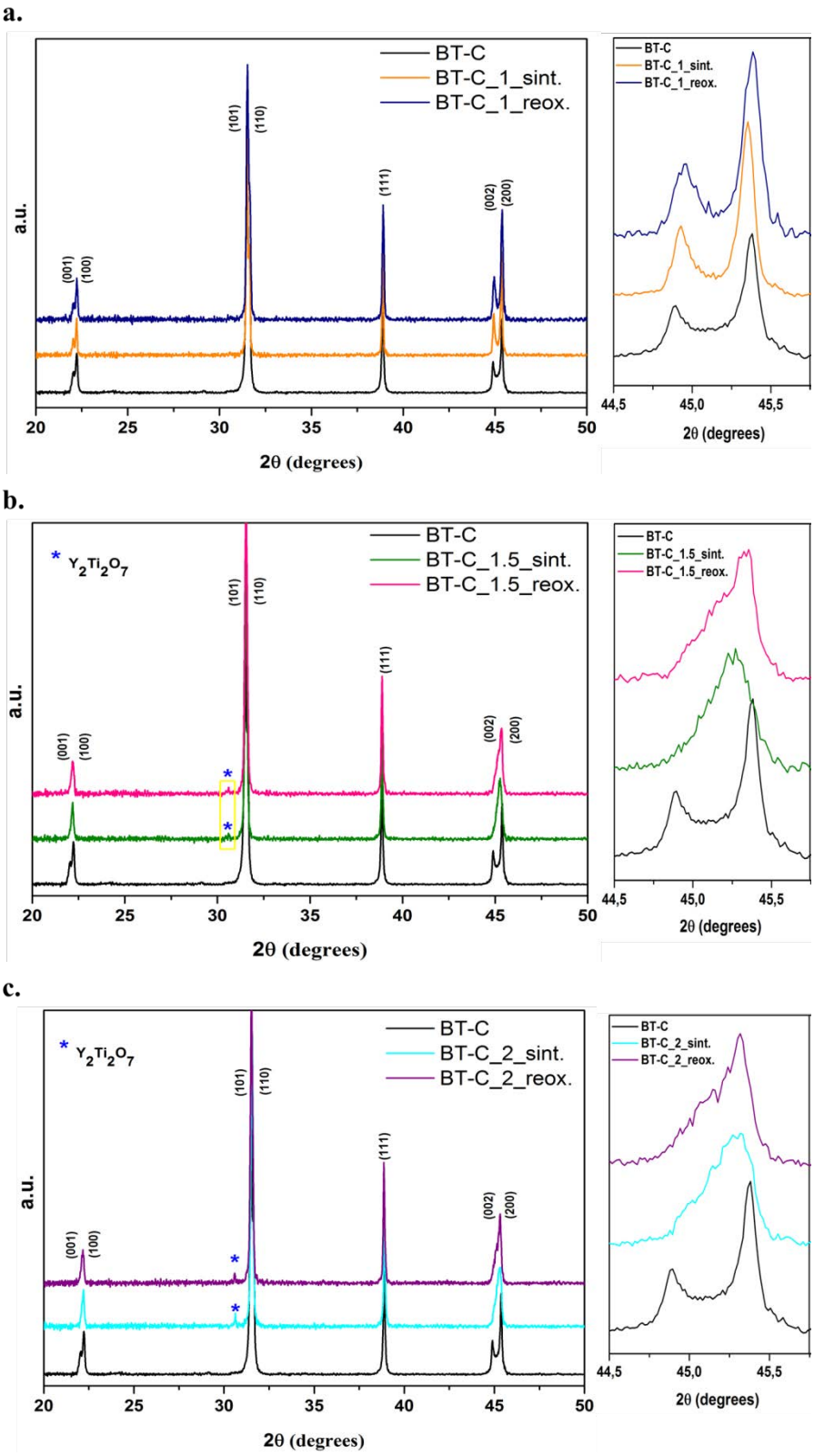

Figure 4.25. *XRD patterns of BT-C powder and ceramics sintered in reducing atmosphere and re-oxidized. Lateral enlargements of zone around 45° are presented.*

Finally, a comparison of the characteristics of the different ceramics issued from BT-A, BT-B and BT-C powders and sintered in reducing atmosphere is presented. The density value of each group of ceramics is reported in Fig. 4.25 according to the dopant level. The BT-A_0 ceramic exhibited the highest density being close to the value for BT-B and BT-C ceramics with dopant level from 1 to 2 wt%. In fact, the density of this group of doped ceramics is roughly different, as can be observed in this figure. Regarding the ceramics issued from BT-A with the same dopant level, the density of them compared to the one of the BT-B and BT-C ceramics is considerably different, being 20 and 30 % respectively lower. Additionally, the density of BT-B ceramics with dopant level between 2.5 and 20 wt% is again higher than the one for the BT-A ceramics with the same Y_2O_3 concentration. However, there is a divergence in the behavior of the density as a function of the [Y_2O_3] between BT-A and BT-B ceramics. First, the density of BT-A_1.5 and BT-A_2 is quite equal. Beyond this dopant concentration, it slightly increases and is practically the same for BT-A_2.5, BT-A_5, and BT-A_20. Otherwise, even when the BT-B_1.5 and BT-B_2 have fairly the same density, as in the BT-A case, the behavior of it beyond this dopant level is opposite to the observed in the BT-A ceramics. For these ceramics (BT-B_2.5, BT-B_5, and BT-B_20) the density values decrease when the concentration of Y_2O_3 increases (although the density is rather the same for the three). Not with standing, it was determined that the densification was below 95% in all cases.

Moreover, the density of ceramics issued from the same powders but sintered under different atmosphere is also different. The ceramics sintered under reducing atmosphere present higher values than the ones fired in air. The atmosphere plays a role in densification mechanism. In fact, when samples are sintered in air, more oxygen vacancies are created which derive in larger volumes and therefore lower densities.

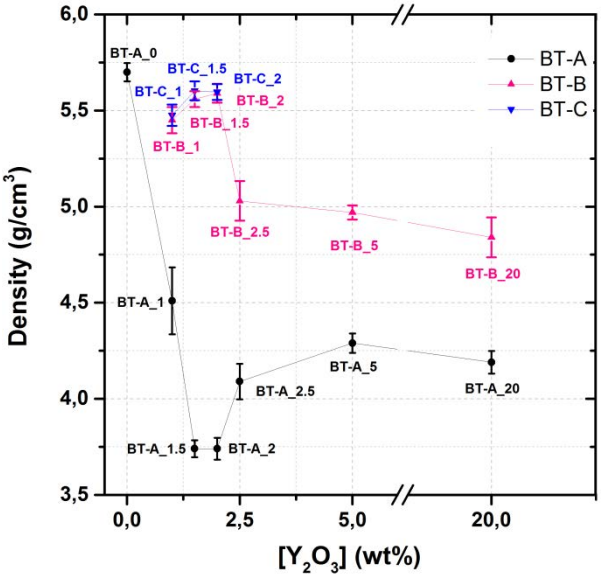

Figure 4.26. *Density values of ceramics sintered in reducing atmosphere at 1310 °C as a function of Y_2O_3 in the starting powder.*

The crystalline structure for all the ceramics obtained in this work is tetragonal. Nonetheless, the tetragonality of the BT is certainly decreased by the incorporation of Y^{3+} ions. As a matter of fact, the increment of its concentration causes stronger modifications on the lattice parameters. In the same way, the introduction of the Y^{3+} in the BT lattice promoted the formation of secondary phases. Indeed, the high levels of doping used in this work were set with the intention to drive the system to it. Y^{3+} replaces Ba^{2+} and Ti^{4+} sites and when the solubility limit in both sites is surpassed, secondary phases can be produced. Of course, the incorporation of Y^{3+} is also markedly affected by the processing conditions and the composition of the raw BT. As seen in this work, the sintering atmosphere played a role in the formation of secondary phases. While in the ceramics fired in air, only the Y_2O_3 is detected besides the $BaTiO_3$ phase. In the ceramics sintered under reducing conditions various phases besides those were identified. A recall of the phase composition for reduced ceramics is given in Table 4.12. The differences in the degree of secondary phases formation regarding the firing atmosphere are related with the higher degree of substitution of the

RE ions when a reducing atmosphere is used. These conditions promote the formation of oxygen vacancies increasing the diffusion of the ions into the system, and leaving as well Ba^{2+} and Ti^{4+} ions free to react among them and with the excess of dopant, forming Ti-rich phases as the ones detected in this work. Therefore, even when no liquid phase was present during the sintering process, the surface diffusion of the ions contributed highly with the precipitation of additional phases. Also, we consider that the interaction of the additives with the BT-matrix and the sintering conditions favored the surface diffusion for above the volume diffusion because not significantly changes in the grain size of the samples were observed.

Regarding the composition of the raw BT powders, the interaction of the rest of the additives and dopants can influence the results too. The A- and B-sites can be replaced not only by the amphoteric Y^{3+} ion but also by ions such as Ca^{2+} and Mg^{2+}, and their interactions will also affect the preference of a site by a specific atom. Their incorporation will also drive to an excess of ions such as the Ti^{4+} in the system, so the formation of secondary phases will be promoted also by the presence of the metal elements. In fact, the compositional design of the formulated powders used in this work included Mg^{2+} and Ca^{2+}. The Mg^{2+} has been reported to inhibit the grain growth because it tends to segregate at the grain boundaries, improving the coalescence during sintering. Also, when it acts together with RE ions contributes to the formation of the "core-shell" structure which is highly desired to accomplish the MLCC specifications (Huang et al., 2015; Wang et al., 2014b). This will also require a careful control of the MgO/R_2O_3 ratio and the firing parameters (Kishi et al., 2003). In the same way, the Ca^{2+} is used to improve the MLCC reliability by limiting the concentration of oxygen vacancies (Yoon et al., 2010).

Table 4.12. *Summary of secondary phases detected in ceramics sintered in reducing atmosphere and 1310 °C.*

$BaTiO_3$ raw material	**Y_2O_3 wt%**	**Sample ID**	**Secondary phases**
BT-A (reagent-grade)	0	BT-A_0	x
	1	BT-A_1	x
	1.5	BT-A_1.5	x
	2	BT-A_2	$Y_2Ti_2O_7$
	2.5	BT-A_2.5	Y_2TiO_5
	5	BT-A_5	Y_2O_3; $Y_2Ti_2O_7$
	20	BT-A_20	sint. ceramic: $Y_2Ti_2O_7$; Y_2TiO_5. reox. ceramic: Y_2O_3; Y_2TiO_5.
BT-B (commercially formulated)	1	BT-B_1	x[a]
	1.5	BT-B_1.5	$Y_2Ti_2O_7$
	2	BT-B_2	$Y_2Ti_2O_7$
	2.5	BT-B_2.5	Y_2TiO_5
	5	BT-B_5	$Ba_6Ti_{17}O_{40}$
	20	BT-B_20	Y_2O_3; $Ba_6Ti_{17}O_{40}$
BT-C (commercially formulated)	1	BT-C_1	x
	1.5	BT-C_1.5	$Y_2Ti_2O_7$
	2	BT-C_2	$Y_2Ti_2O_7$

x: no secondary phases were discerned to the extent of the XRD detection limit.

References

Ashburn, T., & Skamser, D. (2008, January). Highly accelerated testing of capacitors for medical applications. In *Proceedings of the 5th SMTA Medical Electronics Symposium*.

Belous, A., V'yunov, O., Kovalenko, L., & Makovec, D. (2005). Redox processes in highly yttrium-doped barium titanate. *Journal of Solid State Chemistry, 178*(5), 1367-1375.

Belous, A., V'yunov, O., Glinchuk, M., Laguta, V., & Makovez, D. (2008). Redox processes at grain boundaries in barium titanate-based polycrystalline ferroelectrics semiconductors. *Journal of materials science, 43*(9), 3320-3326.

Huang, X., Liu, H., Hao, H., Zhang, S., Sun, Y., Zhang, W., & Cao, M. (2015). Microstructure effect on dielectric Properties of MgO-doped $BaTiO_3$–$BiYO_3$ ceramics. *Ceramics International, 41*(6), 7489-7495.

Kim, C. H., Park, K. J., Yoon, Y. J., Hong, M. H., Hong, J. O., & Hur, K. H. (2008). Role of yttrium and magnesium in the formation of core-shell structure of $BaTiO_3$ grains in MLCC. *Journal of the European Ceramic Society, 28*(6), 1213-1219.

Kishi, H., Mizuno, Y., & Chazono, H. (2003). Base-metal electrode-multilayer ceramic capacitors: past, present and future perspectives. *Japanese Journal of Applied Physics, 42*(1R), 1.

Koschek, G., & Kubalek, E. (1987). On the Electronic Structure and the Local Distribution of the Second Phase $Ba_6Ti_{17}O_{40}$ in $BaTiO_3$ Ceramics. *Physica status solidi (a), 102*(1), 417-424.

Liu, G., & Roseman, R. D. (1999). Effect of BaO and SiO_2 addition on PTCR $BaTiO_3$ ceramics. *Journal of Materials science, 34*(18), 4439-4445.

Lu, H. Y., Bow, J. S., & Deng, W. H. (1990). Core-Shell Structures in ZrO_2-Modified $BaTiO_3$ Ceramic. *Journal of the American Ceramic Society*, 73(12), 3562-3568.

Makovec, D., Samardžija, Z., & Drofenik, M. (2004). Solid solubility of holmium, yttrium, and dysprosium in $BaTiO_3$. *Journal of the American Ceramic Society, 87*(7), 1324-1329.

Öksüz, K. M., Torman, M., Şen, S., Şen U. (2016). Effect of sintering temperature on dielectric properties of SiO_2 doped $BaTiO_3$ ceramics. *Materials, Methods & Technologies, 10*, 361-366.

Paredes-Olguín, M., Lira-Hernández, I. A., Gomez-Yañez, C., & Espino-Cortes, F. P. (2013). Compensation mechanisms at high temperature in Y-doped $BaTiO_3$. *Physica B: Condensed Matter*, *410*, 157-161.

Tsur, Y., Dunbar, T. D., & Randall, C. A. (2001). Crystal and defect chemistry of rare earth cations in $BaTiO_3$. *Journal of electroceramics*, *7*(1), 25-34.

V'yunov, O. I., Kovalenko, L. L., Belous, A. G., & Belyakov, V. N. (2005). Oxidation of reduced Y-doped semiconducting barium titanate ceramics. *Inorganic Materials*, *41*(1), 87–93. Translated from *Neorganicheskie Materialy*, *41*(1), 93–100.

Wang, M. J., Yang, H., Zhang, Q. L., Hu, L., Yu, D., Lin, Z. S., & Zhang, Z. S. (2014a). Doping behaviors of yttrium, zinc and gallium in $BaTiO_3$ ceramics for AC capacitor application. *Journal of Materials Science: Materials in Electronics*, *25*(7), 2905-2912.

Wang, M. J., Yang, H., Zhang, Q. L., Lin, Z. S., Zhang, Z. S., Yu, D., & Hu, L. (2014b). Microstructure and dielectric properties of $BaTiO_3$ ceramic doped with yttrium, magnesium, gallium and silicon for AC capacitor application. *Materials Research Bulletin*, *60*, 485-491.

Wu, Y. C., Wang, S. F., McCauley, D. E., Chu, M. S., & Lu, H. Y. (2007). Dielectric Behavior and Second Phases in X7R-Formulated $BaTiO_3$ Sintered in Low-Oxygen Partial Pressures. *Journal of the American Ceramic Society*, *90*(9), 2926-2934.

Yoon, S. H., Park, Y. S., Hong, J. O., & Sinn, D. S. (2007). Effect of the pyrochlore ($Y_2Ti_2O_7$) phase on the resistance degradation in yttrium-doped $BaTiO_3$ ceramic capacitors. *Journal of Materials Research*, *22*(9), 2539-2543.

Yoon, S. H., Kang, S. H., Kwon, S. H., & Hur, K. H. (2010). Resistance degradation behavior of Ca-doped $BaTiO_3$. *Journal of Materials Research*, *25*(11), 2135-2142.

Yuan, Y., Zhang, S., & Li, C. (2004). The effect of doping process on microstructure and dielectric properties of $BaTiO_3$-based X7R materials. *Journal of Materials Science: Materials in Electronics*, *15*(9), 601-606.

Zhang, J., Hou, Y., Zheng, M., Jia, W., Zhu, M., & Yan, H. (2016). The occupation behavior of Y_2O_3 and its effect on the microstructure and electric properties in X7R dielectrics. *Journal of the American Ceramic Society*, *99*(4), 1375-1382.

Zhi, J., Chen, A., Zhi, Y., Vilarinho, P. M., & Baptista, J. L. (1999). Incorporation of yttrium in barium titanate ceramics. *Journal of the American Ceramic Society*, *82*(5), 1345-1348.

General Conclusion and Perspectives

The objective of this thesis work was to analyze the behavior of $BaTiO_3$ doped with Y_2O_3. This issue was addressed by two distinct yet related perspectives. The barium titanate (BT) powders that are used in formulations for dielectric materials of multilayer ceramic capacitors (MLCCs) contain different additives and dopants to enhance it electrical properties. However, sometimes the dopants can lead to the formation of secondary phases that are believed responsible for the detriment in the insulation resistance of the MLCCs. One of the most common and suitable dopants is the Y_2O_3, which is related to secondary phases of the pyrochlore type, $Y_2Ti_2O_7$.

In this way, a first approach was made by the electrical characterization of MLCCs of the X7R type, which composition is based on $BaTiO_3$ doped with 1.05 % of Y_2O_3. The characterization of three different groups (A, B and C) of MLCCs was performed by means of high life accelerated tests (HALT) that allowed gathering the data related to its mean time to failure (MTTF). Statistical analyses were performed using the Weibull distribution and then associating the found parameters with the Arrhenius model to determine the activation energy related to the failures produced under controlled conditions. The discrimination of the three groups of samples according to its behavior under the stress tests was achieved. It was evidenced by the time-to-failure (TTF) of the samples under combined stress tests that the Group A appears to be the more reliable followed by the Group B and at least the Group C, which was found to be the most affected by the high stress conditions. Combined tests at different levels of thermal and electrical stress were performed with the aim to determine if the failure of the samples changed at higher levels. It was evidenced that at higher temperatures the expected life of the capacitors is decreased, and a higher value of voltage produces this effect as well. For the Groups A and B, the failures seem to have the same mechanism(s) in a

temperatures range of 100 - 200 °C when tested at 400 and 600 V. Meanwhile, the Group C present this behavior but in a much lower range of 20 – 90 °C. This was reflected thorough the analyses of the time-to-failure (TTF) data using the Weibull distribution, since the plots obtained for these conditions presented a similar behavior. Then, it was possible to determine the activation energy (E_a) value for each set of testing conditions and it was found that at 400 V the Group A has the lower value of E_a (1.06 ± 0.08 eV) which indicates and confirms that the applied stress has lower effect over this Group compared with the Group B (E_a = 1.25 ± 0.05 eV) and the Group C (E_a = 1.45 ± 0.06 eV). Hence, when the electrical stress is 400 V, the Group C is expected to have the life time that will change more rapidly as the temperature changes. On the other hand, when a higher voltage was applied (600 V) even though the TTF observed were lower compared to the ones obtained at 400 V, the activation energy determined was not significantly different for the three groups. However, the values were found to be lower than for the testing conditions at 400 V in the cases of the Group B (E_a = 1.09 ± 0.02 eV) and the Group C (E_a = 1.08 ± 0.02 eV). The Group A a similar activation energy despite the higher electrical stress (E_a = 1.01 ± 0.09 eV), which once again can be an indication of its higher stability compared to the other two groups. Even though the failure mechanisms were not determined, with the determined values for the activation energy related to them is possible to say that since they are above the same for the three groups of samples, this could imply that despite their compositional differences and the way they are affected by the high values of stress, they fail under the same mechanism(s).

In general, the electrical characterization of MLCCs samples was possible, associating an E_a value to the breakdowns and observing the influence of high stress values over the reliability of the samples. This part of the work also allowed us to set-up an in-house device that was completely developed at the LAPLACE laboratory and can be used for the performance of high accelerated life tests over MLCCs in an accurate way to obtain information about its expected life time to use it and relate it with the failure modes and the reliability of the samples. Also, bearing in mind that the

principal differences among these groups of capacitors are given by the composition of its dielectric material i.e., the amount of additives and dopants, these results provided information to confirm that the samples will have different properties (i.e., insulation resistance) according the composition of the dielectric ceramic formulation. For that reason experiments aimed to identify the impact of differences in the chemical composition of Y-doped $BaTiO_3$ on the lifetime of MLCCs under accelerated conditions, were conducted. Despite the apparent small differences in the chemical composition, the lifetime of the MLCCs can change from tens of hours (36 h) to less than a second at 400 V and 140 °C. The change in the Ca content induces a great drop in the lifetime from equivalent sintering and processing conditions. Despite this, only when thermally evaluated, the activation energies of the failure remain within the same range of 1–1.45 eV, which could be related to the activation energies of oxygen vacancies in $BaTiO_3$. Although the thermally activated processes are well-described by the Arrhenius expression, the effect of the electric field is not as simple as the empirical equation claims. It can be suggested from the results that the presence of cations, which was Ca in this case, reduces the activation energy, which thermally reduces the life expectation, but increases the reliability of the MLCC in terms of sensitivity to the electric field. This is reflected not only in the activation energy (E_a) and the voltage sensitivity exponent (n), but also through the pre-exponential factor (A) of the Arrhenius relationship. To further understand the failure mechanism of the MLCCs, the relationship between the microstructure and structural evolution during aging must be established, by observing the compositional evolution and how it is related to the Ca content in the $BaTiO_3$, in addition to its role in the formation the secondary phases.

The following step of the study was to evaluate the possibility of the secondary phases' formation due to the presence of Y_2O_3 as dopant. Since it is not the only dopant found in the MLCCs dielectric formulation, the role of the Y_2O_3 as dopant was evaluated in a reagent grade BT powders and two industrially formulated BT powders with the aim to see the interactions that can be given in a BT-Y_2O_3 system and a BT-Y_2O_3-additives/dopants system. The formulated starting powders used for

this part, were the same that have been applied in the manufacturing of MLCCs pieces corresponding to the Groups B and C characterized in the first part. Thus, powders and ceramics with different Y_2O_3 concentrations were prepared and subsequently thermally treated or sintered, respectively. Heat treatment of powders was conducted on air, while sintering of ceramics was carried out both, in air and reducing atmosphere. It was evidenced that the crystalline structure of $BaTiO_3$ can be affected by the Y^{3+} presence either in powders or ceramics, being more noticeable when Y^{3+} doping level increases. Also, under some conditions, the formation of secondary phases was promoted, being identified the $Ba_6Ti_{17}O_{40}$, Y_2TiO_5 and $Y_2Ti_2O_7$. These results provide an insight about the behavior of Y^{3+} when it is used as $BaTiO_3$ dopant in high levels. Plus, it the results provide clear evidence that the interactions among additives used in a commercial formulation are quite important and play a role in the final properties and the formation of secondary phases as well.

This work evidences that the BT-based formulations for dielectric applications are very sensitive to the most slightly changes in its compositions and this can lead to important changes of the final properties of the material and the reliability of the same. Other perspectives may be considered in order to have a more accurate study to describe the real role of other additives and dopants and especially the interactions they may have in real systems under the conditions used in their different applications. Performing an electrical characterization of the MLCCs samples used in this work aiming to determine its failure mechanism(s) could give interesting information about the properties of the dielectric material.

RESUME

Introduction générale

De nos jours, les appareils électroniques font partie de la vie courante : ordinateurs, téléphones, appareils électriques en sont quelques exemples. Actuellement, la présence de composants électroniques augmente de plus en plus dans les industries telles que l'automobile et l'aéronautique. L'un des principaux composants de ces dispositifs est le condensateur, dont la fonction principale est le stockage d'énergie. Il existe plusieurs types de condensateurs, l'un des plus utilisés étant les condensateurs céramiques multicouches (MLCC). Les MLCC offrent des avantages essentiels en raison de leur faible coût, l'une des raisons de sa prédominance sur le marché de l'électronique. Différents types de MLCC existent, en fonction de l'application visée. Les caractéristiques des MLCC vont être déterminées par des paramètres extrinsèques et intrinsèques; c'est-à-dire la nature, les caractéristiques, la synthèse et le traitement du matériau diélectrique et le processus de production des condensateurs. Ces facteurs peuvent influencer la fiabilité finale des condensateurs et donc des dispositifs. Pour cette raison, il est très important de développer des matériaux céramiques adaptés aux différents marchés. L'une des principales stratégies pour obtenir des condensateurs fiables consiste à adapter les caractéristiques du matériau diélectrique en modifiant sa composition.

Le titanate de baryum ($BaTiO_3$) est le matériau diélectrique de base des MLCC en raison de ses propriétés, essentiellement sa permittivité élevée. Pour améliorer ses propriétés électriques, il faut le modifier en incluant plusieurs additifs et dopants dans la formulation de base du diélectrique. La structure pérovskite du BaTiO3 a la capacité d'accueillir des dopants qui, selon les différentes conditions, occuperont les sites A ou B du réseau. L'occupation des dopants à l'intérieur de la structure détermine les propriétés électriques initiales, et on suppose également la fiabilité (durée de vie) du produit final. La formulation de poudres de titanate de baryum comprend comme des dopants des terres rares (REE). Parmi ceux-ci, Y_2O_3 est le plus commun pour la fabrication de condensateurs céramiques multicouches avec des électrodes en métal (BME-MLCC) car il a un coût inférieur à celui de Ho_2O_3, Er_2O_3 et Dy_2O_3 et offre des propriétés similaires. En outre, des cations tels que Mn^{2+}, Mg^{2+} et Ca^{2+} peuvent contribuer à la distribution globale des défauts électroniques générés lorsque les ions dopants sont introduits dans le réseau et au cours du processus de fabrication des condensateurs. En plus de ces dopants, des additifs sont ajoutés pour modifier les conditions de production, tel que l'oxyde SiO_2, utilisé pour diminuer les températures de frittage. Les propriétés finales résulteront des interactions du titanate de baryum avec les dopants et les additifs, dans des conditions de frittage spécifiques. La complexité du système augmente lorsque, dans certaines conditions, des phases secondaires sont formées. Dans les travaux précédents, ces phases secondaires, en particulier celles liées au dopage à Y_2O_3, seraient responsables des mécanismes de défaillance à long terme lors de l'utilisation des MLCC.

Ce travail de thèse a pour objectif d'analyser le rôle du dopant Y_2O_3 et sa contribution possible à la formation de phases secondaires dans la matrice $BaTiO_3$. La réalisation de cet objectif implique deux blocs expérimentaux. Premièrement, la caractérisation électrique des MLCC avec $BaTiO_3$ dopé à Y_2O_3 en tant que diélectrique par la réalisation d'essais à vie accélérée élevée (HALT) qui conduisent à obtenir des indicateurs de durée de vie. Deuxièmement, le développement d'une étude de dopage comprenant la préparation de

poudres et de céramiques dans différentes conditions de frittage en utilisant Y_2O_3 comme dopant pour deux types de poudres : une pure et deux formulées pour des applications industrielles.
Ce manuscrit de thèse est divisé en quatre chapitres.
Le premier chapitre est une introduction bibliographique. Il présente les propriétés générales de $BaTiO_3$, et comment elles peuvent être améliorées par l'utilisation de dopants tels que Y_2O_3 dans les formulations du matériau diélectrique utilisé dans les condensateurs céramiques multicouches.
Le chapitre 2 décrit les différentes méthodes expérimentales ainsi que les techniques de caractérisation utilisées dans ce travail.
Dans le chapitre 3 nous présentons la caractérisation électrique des condensateurs céramiques multicouches (MLCC) à l'aide d'essais de durée de vie accélérée (HALT) pour déterminer le temps moyen avant défaillance (MTTF) de chaque groupe d'échantillons et effectuer des analyses statistiques de Weibull. Le modèle d'Arrhenius a permis d'obtenir la valeur de l'énergie d'activation (Ea) liée à la défaillance des condensateurs dans des conditions déterminées.
Enfin le dopage par Y_2O_3 de deux types de poudres $BaTiO_3$ est présenté dans le chapitre 4.

CHAPITRE 1 : Introduction bibliographique

Le titanate de baryum ($BaTiO_3$ ou BT) est un matériau ferroélectrique remarquable car il a une activité ferroélectrique élevée, une constante diélectrique et une polarisation spontanée (Li, Xu, Chu, Fu et Hao, 2009) et présente une résistivité élevée (1010-1012 Ω cm) (Belous, V '). yunov, Glinchuk, Laguta et Makovez, 2008). En en raison de sa constante diélectrique élevée, de ses faibles pertes diélectriques et de ses performances supérieures à haute fréquence, l'une de ses applications les plus courantes est le matériau diélectrique pour les condensateurs céramiques (Wang, Chen, Gui et Li, 2016). Parmi ces condensateurs céramiques, les condensateurs céramiques multicouches (MLCC) sont largement utilisés dans les applications militaires, automobiles et de télécommunication dans lesquelles les dispositifs sont soumis à des changements significatifs de température, de tension et de fréquence (Wang et al, 2001). Néanmoins, lorsque $BaTiO_3$ est pur, il se produit une grande variation de la constante diélectrique à proximité de la température de Curie (Tc), ce qui rend le matériau céramique inadapté aux applications de condensateur. Pour cette raison, les formulations à base de condensateur BT doivent être modifiées chimiquement pour répondre aux caractéristiques de température-capacité requises (X.H. Wang et coll., 2001; J. Wang et coll., 2016; T. Wang, 2009).

1.1. Le titanate de baryum

La structure cristalline de cet oxyde appartient au type pérovskite Cette structure lui permet de présenter une constante diélectrique élevée. Le BT pur présente une grande variation de la constante diélectrique près de la température de Curie (Tc) à 120 ° C (X. H. Wang et al, 2001). De nombreux efforts ont été déployés pour améliorer les propriétés électriques du titanate de baryum pour différentes applications. L'une des méthodes les plus courantes et les plus efficaces a consisté à modifier la formulation en insérant plusieurs additifs et dopants. La différence entre les additifs et les dopants n'est pas définie avec exactitude pour

ce domaine d'étude. Cependant, on considère habituellement que les additifs contribuent à l'amélioration du processus de production alors que les dopants sont supposés avoir un impact direct sur les propriétés finales du matériau, c'est-à-dire les propriétés diélectriques. Dans ce travail, c'est cette définition que nous avons pris en compte.

1.2. Rôle de Y_2O_3

La formulation de $BaTiO_3$ (BT) utilisée dans la fabrication des MLCC, doit être adaptée aux propriétés électriques, en particulier à haute température et sous champ électrique élevé (Ashburn & Skamser, 2008; Yoon, Park, Hong & Sinn, 2007). À cette fin, plusieurs additifs et dopants sont ajoutés à $BaTiO_3$. L'un des dopants les plus utilisés est Y_2O_3, qui est ajouté dans le but de générer des mécanismes de compensation contribuant à améliorer la fiabilité des condensateurs.

Y_2O_3 a un rayon ionique de 0,107 nm, il est intermédiaire entre celui de l'ion Ba^{2+} (0,161 nm) et l'ion Ti_{4+} (0,06 nm). Par conséquent, Y^{3+} peut occuper le site cationique de Ba^{2+} ou Ti^{4+} dans le réseau BT (Wang et al., 2014; Tsur et al., 2001a). Cela permet à Y^{3+} de se comporter comme accepteur ou donneur en fonction de la position dans le réseau. L'inclusion de l'ion $^{Y3+}$ dans la structure BT dépend de facteurs cinétiques et thermodynamiques (Makovec et al., 2004). La pression partielle d'oxygène et la température de frittage induiront également la formation de lacunes Ba^{2+} ou Ti^{4+}, conduisant Y^{3+} à occuper l'un ou l'autre des sites (Belous et al., 2005; Paredes-Olguín et al., 2013). Ceci sera également influencé par le rapport Ba / Ti, la concentration en dopant et sa solubilité. Les cations yttrium ont une solubilité différente dans les sites Ba et Ti. Zhi et al., (1999) ont indiqué une solubilité de Y^{3+} au site Ba d'environ 1,5 at% lorsqu'ils étaient frittés sous air à 1440 - 1470 ° C, alors qu'ils atteignaient 4% en cas de frittage dans des conditions réductrices (V'yunov, Kovalenko, Belous et Belyakov, 2005). Pour les sites Ti, la solubilité est plus élevée, environ 12,2% à 1515 ° C lors du frittage dans l'air. Wang et al. (2014) ont rapporté que l'introduction de Y^{3+} dans le réseau BT peut entraîner des changements de structure, tels que la transformation de phase quadratique - cubique.

Belous et al. (2008) ont étudié BT dopée à l'yttrium, identifiant les processus dans lesquels le dopant est utilisé. On sait que les matières premières peuvent contenir des impuretés. Dans ce cas, les impuretés paramagnétiques ont été identifiées comme pouvant occuper les sites Ti. Ainsi, une partie des cations Y^{3+} peut participer à un échange. L'yttrium influence également les mécanismes de compensation de charge. Et comme effet collatéral, il a été trouvé qu'il peut participer à la formation de précipités tels que $Ba_6Ti_{17}O_{40}$ et $Y_2Ti_2O_7$. Ces phases secondaires ont généralement été trouvées lorsque la solubilité solide du dopant dans le BT est dépassée.

Avec la quantité appropriée de dopants, les propriétés structurales, optiques et électriques d'un système dopé au BT peuvent être améliorées (Hernández Lara et al., 2017). D'autre part, il existe de nombreux travaux où la formation de phases secondaires a été observée lors du dopage de BT avec des terres rares (REE) (Belous et al., 2008; Yoon et al., 2007; Zhang et al., 2016).). La formation de ces précipités dépend de différents facteurs, à savoir les conditions de frittage et la concentration en dopant (M.T. Buscaglia, Viviani, M. Buscaglia, Bottino et Nanni, 2002). Ces phases secondaires sont généralement formées lorsque la quantité de dopant est supérieure à sa limite de solubilité dans le réseau BT. Cet excès de dopant peut entraîner son interaction avec d'autres ions libres présents dans le système, comme Ti^{4+}. Ensuite, si les conditions sont appropriées, un précipité se forme. Certaines des phases secondaires observées sont $Ba_2TiSi_2O_8$ (Wu, Wang, McCauley, Chu et Lu, 2007),

$Ba_6Ti_{17}O_{40}$ (Belous et al., 2008), Y_2TiO_5 (Yoon et al., 2007) et l'un des Le plus courant lorsque le dopage avec des oxydes de terres rares (Dy_2O_3, Er_2O_3, Y_2O_3 et Ho_2O_3) est la phase de type pyrochlore, $R_2Ti_2O_7$ (Jeong et al., 2005). Parmi les pyrochlores, Er2Ti2O7 (Buscaglia et al., 2002), $Gd_2Ti_2O_7$ (Hernández Lara et al., 2017), $Ho_2Ti_2O_7$ (Makovec et al., 2004) et $Y_2Ti_2O_7$ (Yoon et al., 2007; Zhang et al., 2016)) a été reporté. $Y_2Ti_2O_7$ est suspecté de nuire à la fiabilité des MLCC basées sur BT (Yoon et al., 2007; Zhang et al., 2016).
L'effet de la présence de ces phases secondaires sur les propriétés structurales et diélectriques de $BaTiO_3$ présente un grand intérêt pour les applications industrielles. Plusieurs auteurs ont rapporté un effet néfaste de $Y_2Ti_2O_7$ sur les performances diélectriques de BT (Wu et al., 2007; Yoon et al., 2007; Zhang et al., 2016). Le pyrochlore à base d'yttrium ($Y_2Ti_2O_7$) est de nature hautement conductrice et est suspecté d'être lié à la dégradation de résistance du matériau par l'accélération de l'électromigration des lacunes d'oxygène (Zhang et al., 2016). L'étude des paramètres de formation et des effets possibles de cette phase présente un grand intérêt dans le domaine académique et industriel, Y_2O_3 étant l'un des dopants les plus fréquemment utilisés dans la production des MLCC.

1.3. Influence de l'atmosphère de frittage sur la répartition des dopants dans les céramiques dopées au BT

L'un des paramètres les plus importants pour obtenir un matériau BT ayant les propriétés appropriées pour son application en tant que diélectrique est la pression partielle d'oxygène (PO_2) pendant le traitement de frittage. PO_2 affecte l'incorporation de dopants dans le réseau BT (Buscaglia et al., 2002; Tsur et al., 2001b). L'occupation de site des dopants dans le réseau BT est limitée par la valence de l'ion, sa taille, le rapport A / B (c'est-à-dire l'activité de Ti dans le système) et par la concentration en lacunes d'oxygène. Il a été observé que PO_2 influence les mécanismes de compensation de charge (ioniquement ou électroniquement), imposant une modification du rapport A / B dans le réseau pérovskite, ce qui peut entraîner la formation de précipités. De plus, les changements induits par le PO_2 affectent significativement le comportement électrique (Fu et al., 2008).

1.4. Condensateurs céramiques multicouches (MLCC)

Au cours des dernières décennies, la conception des appareils électroniques a été axée sur la miniaturisation et la réduction de la consommation d'énergie. Cette tendance nécessite une grande fiabilité pour les composants électroniques (Shimada, Utsumi, Yonezawa et Takamizawa, 1981). Les condensateurs céramiques multicouches (MLCC) figurent parmi les éléments électroniques les plus importants (Fig. 1). Ils présentent un rendement volumétrique économique pour la capacité et une grande fiabilité. Les MLCC sont caractérisées par une constante diélectrique élevée (K) et des couches diélectriques plus fines (Jain, Fung, Hsiao et Chan, 2010). Selon l'application, les MLCC peuvent être divisés en deux types: pour la compensation de température et pour la constante diélectrique élevée. Les MLCC pour une constante diélectrique élevée utilisent le titanate de baryum comme composant diélectrique. Parmi ce type de condensateurs, le X7R est le plus stable, couvrant un large spectre d'applications.

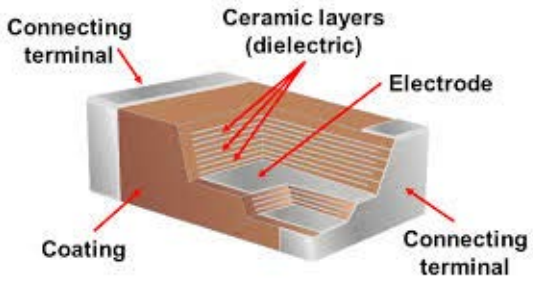

Figure 1. Structure de base d'un condensateur céramique multicouche.

Chaque étape du procédé de fabrication doit être contrôlé, en prenant en compte certains facteurs clés qui influenceront de manière critique la durée de vie et la dégradation de la résistance des condensateurs. Certaines des considérations à prendre en compte, comme on l'a expliqué, sont les caractéristiques de la poudre de BT de départ et les caractéristiques de la formulation finale à appliquer, à savoir l'optimisation des additifs et des dopants. Il existe également certains aspects liés en particulier au procédé, tels que le revêtement du matériau diélectrique et le contrôle des conditions atmosphériques pendant le traitement thermique.

Néanmoins, même si les recherches menées au cours des dernières décennies ont permis aux industries d'optimiser le processus de production et d'améliorer considérablement la technologie dans le domaine de l'électronique, certaines défaillances sont encore observées dans certains cas.

Deux modes de défaillance ont été identifiés dans les condensateurs céramiques multicouches (MLCC) à base de métal-électrode (BMC): la dégradation catastrophique et lente. Les défaillances catastrophiques sont principalement dues aux défauts de traitement actuels (défauts extrinsèques), tels que les vides, les fissures et les délaminations. Celles-ci se caractérisent par une augmentation accélérée du courant de fuite. D'autre part, les défaillances de dégradation lente sont liées à l'électromigration des lacunes d'oxygène, qui sont considérées comme des défauts intrinsèques, et se caractérisent par une augmentation quasi linéaire du courant de fuite par rapport au temps de stress (Liu, 2015).

Ces modes de défaillance peuvent être distingués à l'aide d'un tracé de Weibull à 2 paramètres. Les défaillances précoces (catastrophiques) peuvent être distinguées par un paramètre de pente de $\beta > 1$. Cette valeur de β indique qu'il ne s'agit pas de mortalités infantiles (Liu et Sampson, 2012).

Les défaillances précoces ont été liées à la diminution de l'épaisseur du diélectrique, provoquée par une contrainte électrique externe. Cela a représenté un problème pour contrôler une haute fiabilité avec la miniaturisation des MLCC. Le courant de fuite en cas de panne qui caractérise une défaillance précoce est de type avalanche (Liu et Sampson, 2012). Comme mentionné précédemment, ces défaillances sont liées à des défauts extrinsèques, à savoir des défauts de construction mineurs introduits pendant la fabrication des condensateurs, le contrôle de la production et les exigences de qualité sont un facteur crucial pour obtenir un produit final fiable.

Il a été rapporté que la dégradation de la résistance d'isolement des BME-MLCC à base de BT pourrait être liée à trois aspects probables: la couche diélectrique, les joints de grains BT et les interfaces d'électrodes internes entre Ni-$BaTiO_3$ (Liu, 2015).

CHAPITRE 2 : Méthodes expérimentales

Dans ce chapitre, nous présentons les différentes techniques analytiques utilisées pour la caractérisation des échantillons ainsi que le montage expérimental effectué tout au long de ce travail. D'abord, la caractérisation des condensateurs céramiques multicouches sera présentée, puis la préparation et la caractérisation des poudres et céramiques $BaTiO_3$ dopées Y_2O_3.

2.1. Protocole HALT (High Accelerated Life Test) pour les mesures individuelles I-V

Pour mettre en place les conditions adéquates pour effectuer correctement un HALT en interne, il était nécessaire de connaître le comportement des trois groupes de condensateurs. De cette manière, des mesures de dégradation de la résistance au cours du temps, sous une valeur de tension élevée fixe et différentes températures pour couvrir une large gamme pouvant fournir les informations requises, ont été effectuées.
Les mesures électriques ont été effectuées sur un échantillon à la fois dans une station de sonde Signatone S-1160 à l'aide d'un système de mandrin à chaud de haute précision (modèle Signatone S-1060R QuieTemp DC) (résolution de 1 ° C et pouvant fonctionner jusqu'à 300 ° C) et une source / moniteur CC d'unité de mesure de source (SMU) 2410 Keithley (tension source de 5 µV à 1100 V; mesure de la tension de 1 µV à 1100 V). Cette configuration expérimentale est illustrée sur la Fig. 2.1.
Pour commencer, une HALT a été réalisée dans des conditions industrielles standard: 400 V et 140 ° C pendant 24 h. Dans ce travail, le test a été arrêté lorsque 24 h se sont écoulés sans défaillance ou au moment où l'échantillon a subi une panne. De plus, les HALT ont été conduits sous la même valeur de tension mais en utilisant des températures différentes pour observer le comportement à des valeurs supérieures et inférieures à 140 ° C.

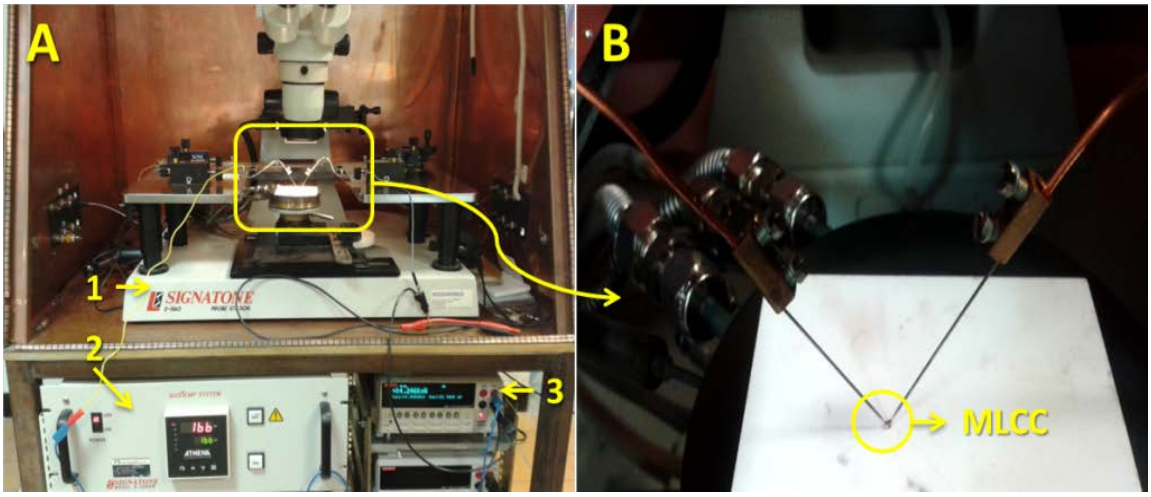

Figure 2.1. (A) Installation expérimentale: (1) station de sonde S-1160, (2) modèle Signatone S-1060R QuieTemp, (3) SMU Keithley 2410. (B) Vue agrandie de la MLCC testée.

2.2. Elaboration, caractérisations des poudres et des céramiques

Des poudres de BT dopées à l' Y_2O_3 ont été préparées (selon la formule Ba1-xYxTi1-x / 4O3) par une réaction à l'état solide traditionnelle. Deux types de BT ont été utilisés, «BT-A» avec pureté commerciale de qualité réactif (Ferro Electronic Materials Inc.) et «BT-B» avec composition formulée pour application dans les MLCC contenant des additifs, principalement: Y_2O_3: 1,05 % SiO_2: 0,30%, CaO: 1,34%. Chaque poudre de BT a été mélangée avec la quantité nécessaire de Y_2O_3 pour obtenir des échantillons dopés à 2,5, 5 et 20%

massique, puis elles ont été broyées dans un flacon de polyuréthane avec des billes d'oxyde de zirconium .
Dans le but d'observer toute modification structurale induite par le dopage, les poudres (x = 2,5 à 20% massique) ont été traitées thermiquement à 1310 ° C sous air pendant 3 heures. Des céramiques ont été préparées avec les poudres contenant 2,5 et 5% massique de Y_2O_3. Ensuite, la poudre de poudre a été séchée et 1% massique de polyvinylbutyral (PVB) a été ajouté aux poudres qui ont été mélangées, broyées et tamisées. Enfin, ils ont été compactés par pressage uniaxial, produisant des disques de 8 mm de diamètre. Les céramiques crues ont été frittées à l'air en utilisant un four tubulaire, selon un protocole de frittage en deux étapes qui a atteint 1350 ° C et est ensuite resté à 1150 ° C pendant 15 h.
La phase cristalline des poudres et des échantillons frittés a été caractérisée par diffraction des rayons X (XRD, modèle D4 Endeavour, Bruker AXS) dans l'intervalle 2θ 10-80 °. La densité apparente de la céramique a été déterminée à partir de la masse et de la géométrie des échantillons. La morphologie des poudres a été analysée par microscopie électronique à balayage (MEB, JSM-6510LV, JEOL). La taille des particules a été déterminée à partir des micrographies à l'aide du logiciel Image J.

CHAPITRE 3: Caractérisation électrique des MLCC

3.1. Introduction

Les condensateurs doivent conserver leurs propriétés dans une certaine tolérance dans une large gamme de températures au cours de leur vie. Le dopage reste la stratégie adéquate pour adapter les propriétés diélectriques de la couche diélectrique à l'application cible, en particulier pour une utilisation en température élevée dans des champs électriques élevés. (Ashburn et Skamser, 2008; Paunović, Živković, Vračar, Mitić et Miljković, 2004).
Étant donné que la fiabilité est un paramètre essentiel dans la conception de l'électronique, les fabricants de composants en tiennent compte à travers différents paramètres. L'évaluation de la fiabilité peut être très précise à travers l'analyse périodique des produits en service et en tenant compte des produits défaillants, mais elle n'est pas prédictive et prend beaucoup de temps. Par conséquent, d'autres méthodes doivent être utilisées pour réduire le temps d'évaluation afin d'avoir une indication de la fiabilité avant la commercialisation des composants. Des conditions d'essai accélérées doivent être conçues pour obtenir la prévision la plus précise possible de la durée de vie des condensateurs dans les conditions de service. Les tests de fiabilité les plus courants des MLCC sont la résistance d'isolement et les mesures de contraintes combinées, également appelées tests de durée de vie hautement accélérée (HALT). (Paulsen et Reed, 2001; Vassilious et Mettas, 2001).
Les systèmes électriques tels que les condensateurs peuvent être testés en utilisant deux types de tests; soit un test de stress constant ou un test de stress progressif peut être effectué. Dans le premier type, un certain nombre d'échantillons sont amenés à leur dégradation dans des conditions de contraintes définies, puis les temps d'échec sont mesurés; dans le second type, les tensions de claquage peuvent être mesurées. Au moment d'effectuer le test électrique, quel que soit le type, pour les conditions données, chaque échantillon testé produira un résultat différent, de sorte que le total des données obtenues peut être analysé par une distribution statistique. (Chauvet et Laurent, juin 1992).

Différents modèles de distribution statistique pourraient être appliqués à l'analyse des données à partir de ces tests, y compris Weibull, Gumbel et Lognormal. La distribution de Weibull est largement utilisée dans ce domaine et est celle utilisée dans ce travail.
En adaptant les propriétés des MLCC, outre les paramètres électriques initiaux, il est très intéressant d'analyser et de rechercher les corrélations entre la formulation structurale et chimique de base et la fiabilité (délai de défaillance) des condensateurs. Très peu d'études dans la littérature abordent cette question, car la production de MLCC pour les tests de fiabilité nécessite au minimum des installations de taille pilote pour produire de nombreux échantillons avec un processus reproductible afin de minimiser l'influence d'autres paramètres que celui testé.
En outre, l'objectif du test concerne un type de condensateur fixe, car le diélectrique est formulé de manière optimale. Par conséquent, les conclusions concernant l'effet du dopage sur la fiabilité de la MLCC sont plutôt spéculatives.
Compte tenu des interactions nombreuses et complexes entre les additifs et les dopants pendant et après le processus de frittage, une approche plus simple doit être entreprise. Dans ce travail, nous déterminons le délai de défaillance de BT.

3.2. Résultats et discussion

La capacité à température ambiante (Fig. 3.1) pour trois compositions est très similaire, autour de 0,1 µF en dessous de 104 Hz avec des pertes diélectriques similaires. La classification X7R spécifie que les valeurs de capacité doivent se situer dans une plage de 15% lorsque le condensateur est exposé à une variation de température entre -55 ° C et +125 ° C. La figure 3.2 montre l'impact de la température dans les valeurs de capacité à 1 kHz.

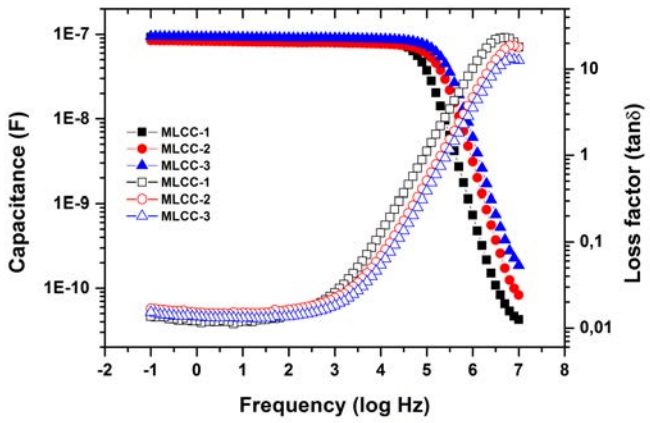

Figure 3.1. Variation de la capacité et des pertes diélectriques des trois types de MLCC en fonction de la fréquence

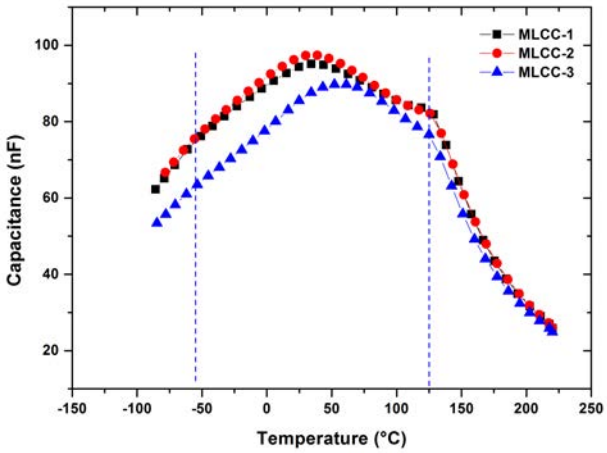

Figure 3.2. Variation de la capacité des trois types de MLCC en fonction de la température (f=1 kHz).

Résultats du test HALT initial

Nous avons d'abord mesuré la durée de rupture dans les conditions HALT de 140 ° C et de 400 V pour les trois compositions (tableau 3.1). L'observation principale est que pour la composition MLCC-2, le temps d'échec était extrêmement court, nous permettant à peine d'appliquer une tension après le chauffage des échantillons. L'augmentation de courant est également décrite comme la résistance d'isolement du condensateur MLCC et est souvent utilisée comme critère complémentaire pour tester les échantillons [19].

Tableau 3.1. Durée de rupture diélectrique pour les MLCC aux conditions initiales du test HALT.

Sample type	Time to breakdown at 140°C and 400V
MLCC-1	37 hours
MLCC-2	< 1 second
MLCC-3	3.5 hours

Nous avons modifié les conditions d'essai de température pour les mesures individuelles de la résistance d'isolement des échantillons MLCC-2, en abaissant la température. En abaissant la température à 60 ° C, nous avons pu observer la diminution de la résistance avant la défaillance des condensateurs. La variation de la valeur de résistance pour MLCC-2 testée individuellement à des températures inférieures à 80 ° C est illustrée sur la Fig. 3.3.

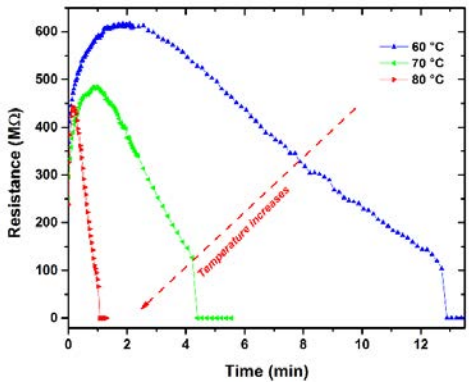

Figure 3.3. Variation de la résistance d'une MLCC-2 à des températures inférieures à 80 ° C et à 400 V.

Le temps de défaillance entre MLCC-1 et MLCC-2 étant extrêmement différent, nous avons effectué des tests complémentaires à différentes températures pour évaluer les énergies d'activation des processus de défaillance. A titre d'exemple, les résultats du condensateur MLCC1 sont présentés sur la Fig. 3.4. Comme le temps de défaillance suit un comportement statistique, nous avons tracé les résultats dans un graphique de type Weillbul.

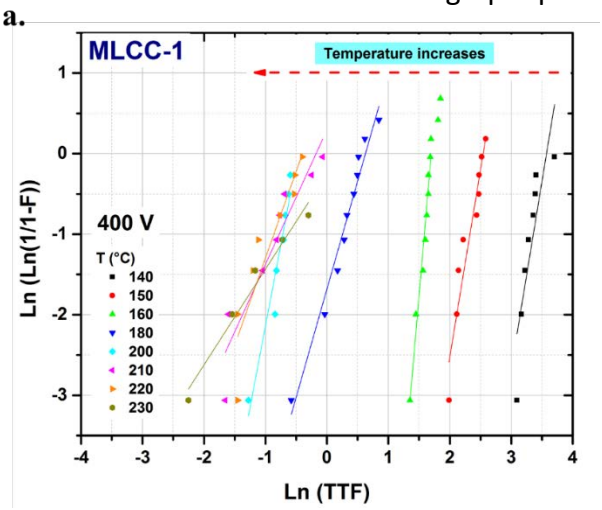

Figure 3.4. Exemple d'un tracé de Weibull pour les MLCC1 testés dans une large gamme de températures et de différentes contraintes électriques: (a) : 400 V

Énergies d'Activation

Les énergies d'activation peuvent être estimées si l'on considère uniquement les données inférieures à 200 ° C pour les types d'échantillons MLCC-1 et MLCC-3 et inférieures à 70 ° C pour MLCC-2. Un exemple est donné sur la figure 3.5. Les énergies d'activation liées aux défaillances des trois types de MLCC ont été déterminées par le modèle d'Arrhenius appliqué à la durée de vie des condensateurs, représentée par l'équation 1.

$$\ln(MTTF) = -\frac{E_a}{kT} + \ln(A) \qquad \text{[eq.1]}$$

MTTF = temps moyen avant échec
Ea = énergie d'activation
k = constante de Boltzmann T = température d'essai absolue
A = facteur pré-exponentiel

La valeur de Ea est une indication de l'effet de l'imposition sur la durée de vie du condensateur. Une grande valeur d'énergie d'activation entraînera un effet important sur le stress imposé à la durée de vie de la puce.

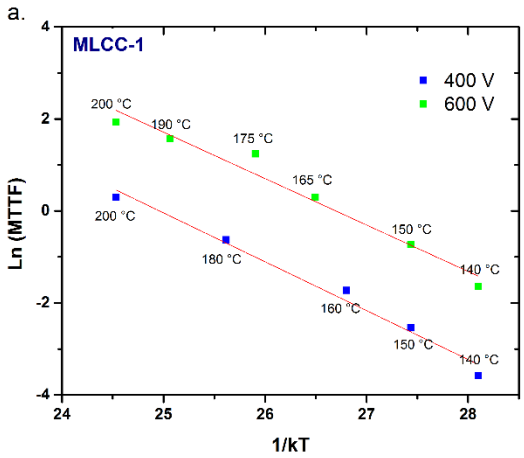

Figure 3.5. Durée de vie caractéristique selon le modèle d'Arrhenius pour (a) MLCC-1 en fonction du stress électrique et thermique.

Discussion sur les énergies d'activation

Les valeurs des énergies d'activation sont données dans le tableau ci-dessous.

Tableau 3.2. Valeurs d'énergie d'activation obtenues à partir du modèle Arrhenius pour MLCC testées sous deux tensions différentes et dans une plage de températures.

MLCCs	E_a **(eV) at 400 V**	E_a **(eV) at 600 V**	***Temperature range***
MLCC-1	1.06 ±0.07	1.01 ±0.09	
MLCC-2	1.45 ±0.05	1.08 ±0.02	
MLCC-3	1.25 ±0.06	1.09 ±0.02	

Les valeurs numériques des énergies d'activation doivent être liées au mécanisme de défaillance de la rupture diélectrique dans les conditions de contrainte. Néanmoins, il existe peu d'informations dans la littérature disponible pour établir cette corrélation. Des valeurs d'énergie d'activation de 1,9 eV ont été associées à un mode de claquage par avalanche (Liu, 2012); pour une défaillance activée par la chaleur, elle peut être comprise entre 1,25 et 1,42 eV (Nomura, 1995) (Rowal, 1984). D'autres auteurs proposent qu'une dégradation thermique dans l'Ea de la MLCC soit comprise entre 1 et 2 eV. En outre, des valeurs comprises entre 1,3 et 1,5 eV ont été décrites comme étant liées à l'usure diélectrique de la capacité diélectrique à base de $BaTiO_3$ (Yoon, 2009).

Chazono et al. (2001) indiquent que les lacunes en oxygène migrent sous l'influence du champ électrique élevé appliqué lors des essais HALT. Yoon et al. (2009) ont suggéré que lorsque les lacunes étaient accumulées à l'interface de l'électrode, un mécanisme de conduction de Frowler Nordhem (tunneling) pourrait être induit et favoriser la dégradation de la couche diélectrique en raison de l'augmentation locale de la conductivité. Les énergies d'activation dans la gamme de 1-2 eV se situent raisonnablement dans l'intervalle de Ea requis pour les mobilités de lacunes d'oxygène (Chan, 1981) (Han, 1987). Dans cette étude, un dopage plus élevé avec du calcium a eu un impact significatif sur le délai d'échec des échantillons MLCC-2, à tel point qu'il n'était plus possible de réaliser le test à des tensions

élevées. Le calcium a été signalé comme élément dopant accepteur dans $BaTiO_3$. Bien que cela puisse d'une part augmenter la résistivité globale de la céramique (Han, 1987), elle peut également modifier l'équilibre des lacunes en oxygène et les interactions complexes avec d'autres éléments dopants lors du frittage et du recuit.
Il est intéressant de noter que malgré les temps d'échec beaucoup plus faibles de la composition de MLCC-2, les énergies d'activation, estimées à une température inférieure, bien qu'elles soient plus grandes, se situent dans la même plage que les deux autres compositions.

3.3. Conclusions

Dans cette partie, nous avons déterminé l'impact des différences de composition chimique de $BaTiO_3$ dopé à l'Y_2O_3 sur la durée de vie des MLCC dans des conditions accélérées. Malgré les petites différences apparentes, la durée de vie de la MLCC peut varier considérablement, se situant aux dixièmes d'heures (36 heures) à moins d'une seconde aux conditions de test de 400 V et de 140 ° C. La variation de la teneur en Ca induit une forte diminution de la durée de vie aux conditions de frittage et de traitement équivalentes. Malgré cela, les énergies d'activation de la défaillance restent dans la même plage de 1,05 à 1,45 eV, ce qui pourrait être lié aux énergies d'activation des lacunes d'oxygène dans BaTiO3. La relation complexe entre la chimie des défauts et les conditions d'élaboration doit donc être étudiée plus avant pour comprendre comment les différentes phases peuvent influencer le délai de défaillance de ces matériaux.

CHAPITRE 4: Dopage de $BaTiO_3$ avec Y_2O_3

Dans optimiser les caractéristiques de $BaTiO_3$ en tant que matériau diélectrique de base pour la fabrication des MLCC, il est important de définir les relations entre la structure, la microstructure et les propriétés électriques. La présence de phases secondaires, dues à la présence d'autres éléments, tels que les dopants, modifie les propriétés électriques du matériau. Parmi les phases signalées, on peut citer les pyrochlores, $Y_2Ti_2O_7$, qui sont supposés être à l'origine des mécanismes de défaillance à long terme des opérations de la MLCC sous fonctionnement nominal (Zhang et al., 2016).
Ce chapitre vise à trouver les phases secondaires dans ce matériau et à évaluer la fiabilité des MLCC utilisant un matériau à base de $BaTiO_3$ pouvant contenir ces phases. Toutes les conditions auxquelles la céramique est exposée lors de sa préparation, de la matière première au dernier traitement thermique, doivent être bien connues. Pour cette raison, il est nécessaire d'effectuer des caractérisations de poudres et de céramiques par des techniques telles que la spectroscopie à plasma à couplage induit (ICP), la diffraction des rayons X et le MEB, pour connaître la composition chimique, la structure et la composition des phases, la porosité et la taille des grains. .

4.1. Poudres de $BaTiO_3$

La composition chimique des poudres $BaTiO_3$ utilisées comme matières premières a été déterminée par les analyses ICP et est présentée dans le tableau 4.1. Comme mentionné précédemment, les poudres formulées pour une application industrielle contiennent des dopants et des additifs.

Traitement thermique et caractérisation des poudres de $BaTiO_3$

Dans le but d'observer tout changement structurel induit par un fort niveau de dopage, les poudres BT-A_2.5, BT-A_5, BT-A_20, BT-B_2.5, BT-B_5 et BT-B_20 ont été traitées thermiquement (TT) à 1310 ° C sous air pendant 3 h. Ce traitement thermique reproduit les conditions de température de frittage dans lesquelles des condensateurs céramiques multicouches sont produits au niveau industriel. Dans ce cas, les poudres sont dénommées BT-X_YTT, où "X" indique la poudre $BaTiO_3$ brute, "Y" Y_2O_3% massique et "TT" traité thermiquement.

Tableau 4.1. Rapport Ba / Ti et composition chimique des poudres de $BaTiO_3$.

	Ba	**Ti**	**Y**	**Ca**	**Sr**	**Si**	**Mn**	**Mg**	**Co**
BT_A* **Ba/Ti = 2.88**	57.55	19.96	<0.01	0.006	0.04	<0.01	<0.001	0.001	<0.01
BT_B** **Ba/Ti = 2.85**	54.67	19.17	1.05	1.34	0.09	0.30	0.05	0.29	115
BT_C** **Ba/Ti = 2.86**	53.86	18.85	1.05	0.57	0.09	0.17	0.05	0.006	0.017

Values are given in wt%. *: BT reagent grade (pure). **: BT commercially formulated.

Morphologie et taille des particules

Les images MEB des poudres BaTiO3 non dopées, BT-A_0 et BT-B_1, sont représentées sur les figures 4.1.a et 4.1.c respectivement. Les deux poudres présentent des particules présentant une morphologie à facettes grossières. Deux tailles de particules sont observées, une plage de 0,48 µm et 1,25 µm pour BT-A_0, et de 0,46 µm et 0,81 µm pour BT-B_1. La valeur de taille moyenne des particules de BT-B_1 est sensiblement inférieure à celle des particules BT-A_0. Cette légère différence est probablement liée au traitement donné à la poudre formulée pour remplir la taille de particule requise pour son utilisation dans le processus de production des MLCC.
Après traitement thermique à haute température, les images MEB des poudres dopées à l'Y_2O_3 BT-A_5TT et BT-B_5TT (Fig. 4.1.b et Fig. 4.1.d) montrent des particules plus arrondies

et définies, comparées aux particules non traitées thermiquement, poudres non dopées (Fig. 4.1.a et Fig. 4.1.c, respectivement). La taille moyenne des grains est similaire pour les deux poudres, respectivement 0,58 µm et 0,53 µm. Certains agrégats sont observés, probablement en raison d'un début de frittage.

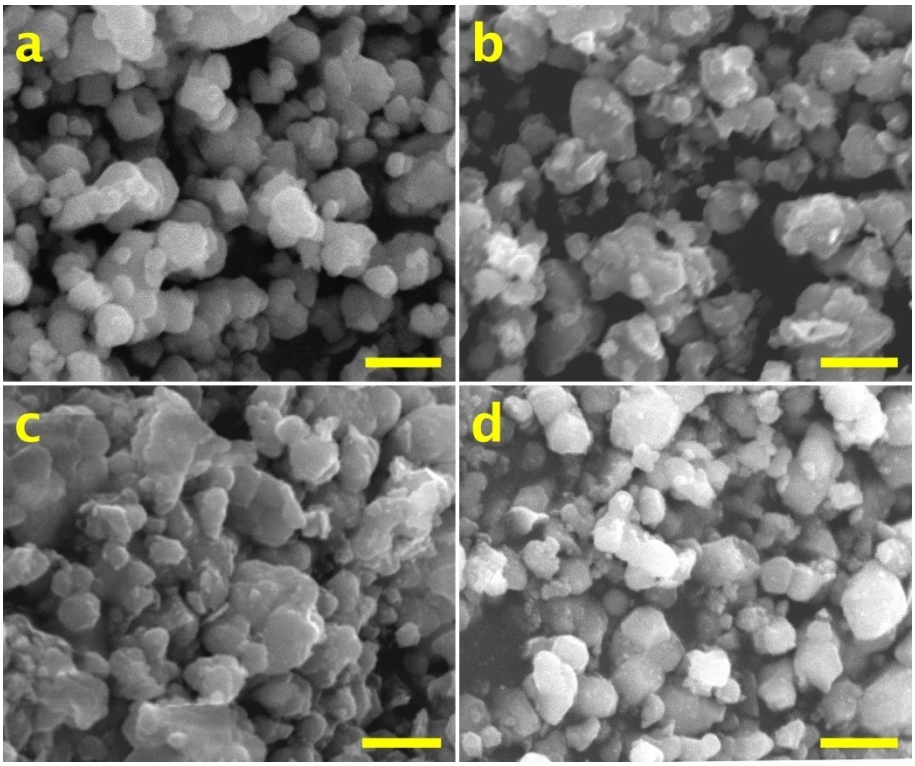

Figure 4.1. Images MEB de poudres brutes de $BaTiO_3$ et des poudres dopées à 5% massique de Y_2O_3 et traitées thermiquement. (a) BT-A_0, (b) BT-A_5TT, (c) BT-B_1 (d) BT-B_5TT. Barre d'échelle: 1 µm

Composition de la structure et de la phase

La manière dont la structure $BaTiO_3$ peut être affectée par un dopant ajouté peut être reflétée dans le rapport c / a, qui change de structure cubique (c / a = 1) à des valeurs plus élevées lorsque le réseau cristallin est modifié pour des raisons telles que la présence d'autres ions. Cette modification du rapport c / a se reflète directement dans le diagramme de diffraction. Pour BaTiO3 avec une phase cristalline cubique, on observe des pics nets d'une valeur de 2θ autour de 31,6 ° et de 45,3 ° correspondant respectivement aux plans (110) et (200). Lorsque la symétrie du système n'est plus cubique, certains plans peuvent apparaître sur le diagramme de diffraction. Dans le cas d'une phase quadratique, les plans (101) et (110) seront visibles, ainsi que les (002) et (200) autour des mêmes valeurs 2θ mentionnées précédemment. Nous avons calculé une variation théorique de la valeur 2-thêta pour le plan (002) en fonction du rapport c / a possible. Une modification du rapport c / a est plus notoire pour les plans (002) et (200) puisque la distance entre leurs pics est supérieure à celle de (101) (110) pics. En fait, tant que la valeur de c / a augmente, la distance entre leurs pics est intensifiée; c'est-à-dire à des valeurs plus élevées de c / a, la phase quadratique est plus évidente à repérer. En outre, le rapport d'intensité entre (002) et (200) pics, lorsque $BaTiO_3$ est dans une phase quadratique, est de 1: 2. Cependant, s'il existe un gradient dans la composition de la matrice, il est possible d'avoir la présence de divers

rapports c / a, ce qui conduit à un aspect différent des pics. Ils peuvent paraître moins intenses, plus larges et même s'ils s'y joignent.
Pour ces raisons, nous discuterons de la manière dont la structure de BaTiO3 est affectée par la présence de Y_2O_3 ajouté, principalement en raison des changements observables dans les pics autour de 45 °.

4.2. Caractérisation des céramiques de $BaTiO_3$ frittées

Le frittage des céramiques (poudre compactée à 300 MPa) a été réalisé à la fois dans l'air et dans l'atmosphère réductrice après deux cycles thermiques différents:
1) Dans l'air, deux étapes de température: 1310 ° C puis 1150 ° C pendant 15 h. Les céramiques frittées avec ce programme sont BT-A (A_0, A_2.5, A_5) et BT-B (B_1, B_2.5, B_5).
2) En atmosphère réductrice (pO2 ≈ 10-8 - 10-11 atm, N_2, H_2O, H_2): 1310 ° C pendant 3 h (ce procédé de frittage a été réalisé en conditions industrielles (KEMET de México), simulant les conditions de production des MLCC). Les céramiques frittées avec ce programme sont BT-A (A_0, … A_20), BT-B (B_1, ... B_20), et BT-C (C_1, C_1.5, C_2).

4.2.1. $BaTiO_3$ frittées sous air

Les valeurs de densité des céramiques BT-A et BT-B obtenues dans ces conditions de frittage sont données sur la figure 4.2. Il est possible de voir que le niveau élevé de Y_2O_3 a affecté la densification en la diminuant par rapport aux échantillons non dopés. Néanmoins, la masse volumique pour la céramique non dopée BT-A est supérieure à celle de la céramique dopée avec 2,5 et 5% massique de Y_2O_3. Pour les céramiques BT-B, les valeurs de densité sont différentes parmi celles-ci, étant aussi inférieures lorsque le contenu de Y_2O_3 augmente. Même lorsque la densification dans les deux cas (BT-A et BT-B) est inférieure en fonction de la teneur en Y_2O_3, les céramiques formées à partir de la poudre BT-B présentent des valeurs de densité plus élevées. Cette différence peut être due aux additifs présents dans la formulation de poudre BT-B, car l'un des objectifs de leur présence est d'améliorer la densification du matériau céramique.

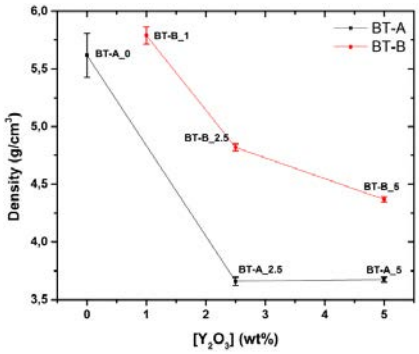

Figure 4.2. Densité des céramiques frittées sous air en fonction de la concentration en Y_2O_3.

Morphologie des grains et taille des grains
Les tailles de grains moyennes de cette céramique sont respectivement de 0,42 µm et de 0,45 µm. Les grains sont de morphologie arrondie. Bien que certains d'entre eux montrent

des signes de frittage, ils ne sont pas vraiment liés comme dans une céramique dense. En effet, la densification de la céramique n'a pas été achevée, comme en témoignent les valeurs de densité qui pourraient être causées par la grande quantité de Y_2O_3. Malgré cela, les grains présentent un aspect homogène. A propos de la taille des grains, la différence entre les deux céramiques est minimale, donc le niveau de dopage ne l'affecte pas.

Composition de la structure et de la phase

Un résumé des compositions de phase pour les poudres traitées thermiquement et les céramiques frittées dans l'air est présenté dans le tableau 4.2.

Les céramiques BT-A cristallisent dans la phase quadratique. Les céramiques BT-A_2.5 et BT-A_5 présentent toutefois une diminution du rapport c/a.

Les diagrammes de diffraction des céramiques formées à partir de poudre BT-B (non présentés ici) montrent une seule phase pérovskite $BaTiO_3$, sans phases secondaires. Cependant, certains pics correspondant aux plans (002) et (200) ont changé en fonction du niveau de dopant. Cela peut être le reflet d'une composition chimiquement inhomogène de la céramique. Cela se traduit par la présence de divers rapports c / a, qui à leur tour affectent l'intensité et la forme des pics ainsi que leur division.

En comparant les diagrammes XRD des céramiques dopées (BT-A_2.5, BT-A_5, BT-B_2.5 et BT-B_5), il est possible de voir que l'influence de la structure Y^{3+} sur la structure de $BaTiO_3$ est plus grande dans le cas de la céramique BT-B. Si l'on compare le pic à 45 ° - ce qui met en évidence une phase quadratique - des deux groupes de céramiques, il est possible de voir que les céramiques dopées BT-B semblent plus jointes. On peut considérer que l'effet dopant sur ces réseaux d'échantillons est plus fort. Ce comportement souligne la forte interaction entre les additifs et les dopants présents dans le BT-B, ce qui se reflète également dans les valeurs de densité ainsi que dans la microstructure de ces céramiques.

Tableau 4.2. Phases secondaires détectées dans les différentes poudres et céramiques traitées thermiquement et frittées à l'air, deux étapes de température: 1310 ° C puis 1150 ° C 15 h.

$BaTiO_3$ raw material	**Y_2O_3 wt%**	**Sample ID**	**Secondary phase**	
			Powder (TT)	**Ceramic**
BT-A (reagent-grade)	0	BT-A_0	x	x
	2.5	BT-A_2.5	x	x
	5	BT-A_5	Y_2O_3	Y_2O_3
	20	BT-A_20	Y_2O_3	x
BT-B (commercially formulated)	1	BT-B_1	x	x
	2.5	BT-B_2.5	x	x
	5	BT-B_5	x	x
	20	BT-B_20	$Ba_6Ti_{17}O_{40}$ and Y_2O_3	x

x: no secondary phases were detected. BT-A_20 and BT-B_20 ceramics were not sintered under these conditions.

4.2.1.$BaTiO_3$ frittée sous atmosphère réductrice

Dans le souci d'être concis, nous présentons dans le tableau 4.3 l'ensemble des principales observations issues des analyses XRD effectuées sur les céramiques BT-B frittées dans des conditions réductrices

Tableau 4.3. Phases secondaires détectées dans les céramiques BT-B frittées sous atmosphère réductrice à 1310 ° C.

$BaTiO_3$ raw material	**Y_2O_3 wt%**	**Sample ID**	**Secondary phase**
BT-B (commercially formulated)	1	BT-B_1	x
	1.5	BT-B_1.5	$Y_2Ti_2O_7$
	2	BT-B_2	$Y_2Ti_2O_7$
	2.5	BT-B_2.5	Y_2TiO_5
	5	BT-B_5	$Ba_6Ti_{17}O_{40}$
	20	BT-B_20	Y_2O_3; $Ba_6Ti_{17}O_{40}$

x: no secondary phases were detected.

Enfin, une comparaison des caractéristiques des différentes céramiques issues des poudres BT-A, BT-B et BT-C et frittées en atmosphère réductrice est présentée (figure 4.3). La céramique BT-A_0 présente la densité la plus élevée, proche de la valeur pour les céramiques BT-B et BT-C avec un niveau de dopant de 1 à 2% massique. En effet, la densité de ce groupe de céramiques dopées est sensiblement différente. En ce qui concerne les céramiques issues de BT-A avec le même niveau de dopant, leur densité par rapport à celle des céramiques BT-B et BT-C est nettement différente, étant respectivement inférieure de 20 et 30%. De plus, la densité des céramiques BT-B avec un niveau de dopant compris entre 2,5 et 20% massique est de supérieure à celle des céramiques BT-A ayant la même concentration en Y_2O_3. Cependant, il existe une divergence dans le comportement de la densité en fonction de la teneur en Y_2O_3 entre les céramiques BT-A et BT-B. Tout d'abord, la densité de BT-A_1.5 est égale à celle de BT-A_2. Au-delà de cette concentration en dopants, elle augmente légèrement et est pratiquement la même pour BT-A_2.5, BT-A_5 et BT-A_20. Dans le cas contraire, même lorsque le BT-B_1.5 et le BT-B_2 ont une densité similaire, comme dans le cas du BT-A, son comportement au-delà de ce niveau de dopant est opposé à celui observé dans les céramiques BT-A. Pour ces céramiques (BT-B_2.5, BT-B_5 et BT-B_20), les valeurs de densité diminuent lorsque la concentration de Y_2O_3 augmente (bien que la densité soit plutôt la même pour les trois).
De plus, la densité des céramiques issues des mêmes poudres mais frittées sous différentes atmosphères est également différente. Les céramiques frittées sous atmosphère réductrice présentent des valeurs plus élevées que celles cuites dans l'air. L'atmosphère joue un rôle dans le mécanisme de densification. En effet, lorsque les échantillons sont frittés dans l'air, il se crée davantage de lacunes en oxygène qui se traduisent par des volumes plus importants et donc des densités plus faibles.

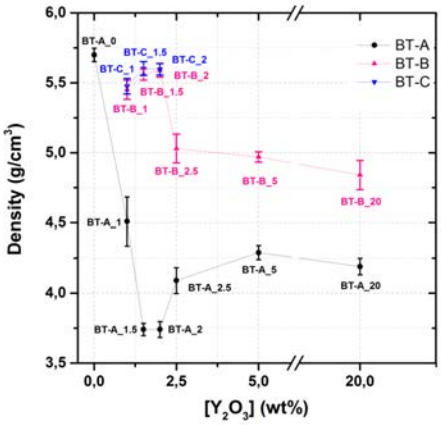

Figure 4.3. Valeurs de densité des céramiques frittées sous atmosphère réductrice à 1310 ° C en fonction de la teneur en Y_2O_3 dans la poudre de départ.

La structure cristalline de toutes les céramiques obtenues dans ce travail est quadratique. Néanmoins, le rapport c/a de BT est certainement diminué par l'incorporation d'ions Y^{3+}. En fait, l'augmentation de sa concentration entraîne des modifications plus importantes sur les paramètres du réseau. De même, l'introduction de Y^{3+} dans le réseau BT a favorisé la formation de phases secondaires. En effet, des niveaux élevés de dopage utilisés dans ce travail ont été fixés. Y^{3+} remplace les sites Ba^{2+} et Ti^{4+} et lorsque la limite de solubilité dans les deux sites est dépassée, des phases secondaires peuvent être produites. Bien entendu, l'incorporation de Y^{3+} est également fortement influencée par les conditions de traitement et la composition de BT brut. Comme nous l'avons vu dans ce travail, l'atmosphère de frittage a joué un rôle dans la formation des phases secondaires. Dans la céramique frittée sous air, seul Y_2O_3 est détecté en plus de la phase $BaTiO_3$. Dans les céramiques frittées dans des conditions réductrices, différentes phases ont été identifiées. Les différences dans le degré de formation des phases secondaires en ce qui concerne l'atmosphère de cuisson sont liées au degré plus élevé de substitution des ions de terres rares lorsqu'une atmosphère réductrice est utilisée. Ces conditions favorisent la formation de lacunes d'oxygène augmentant la diffusion des ions dans le système et favorisant l'interaction des ions Ba^{2+} et Ti^{4+}, formant des phases riches en Ti. Par conséquent, même en l'absence de phase liquide au cours du processus de frittage, la diffusion de surface des ions a fortement contribué à la précipitation de phases supplémentaires. En outre, nous considérons que l'interaction des additifs avec la matrice BT et les conditions de frittage ont favorisé la diffusion en surface au-dessus de la diffusion en volume car des changements significatifs dans la taille des grains des échantillons n'ont pas été observés.

Conclusion générale et perspectives

L'objectif de ce travail de thèse était d'analyser le comportement de $BaTiO_3$ dopé avec Y_2O_3. Cette question a été abordée par deux perspectives distinctes mais liées. Les poudres de titanate de baryum (BT) utilisées dans les formulations des matériaux diélectriques des condensateurs céramiques multicouches (MLCC) contiennent différents additifs et dopants pour améliorer ses propriétés électriques. Cependant, les dopants peuvent parfois conduire à la formation de phases secondaires qui sont responsables de la dégradation de la

résistance d'isolement des MLCC. L'un des dopants les plus courants et les plus appropriés est Y_2O_3, qui est lié aux phases secondaires du type pyrochlore, $Y_2Ti_2O_7$.
De cette manière, une première approche a été faite par la caractérisation électrique des MLCC de type X7R, cette composition étant à base de $BaTiO_3$ dopé avec 1,05% de Y_2O_3. La caractérisation de trois groupes différents (A, B et C) de MLCC a été réalisée au moyen de tests accélérés à haute durée de vie (HALT) qui ont permis de rassembler les données relatives au temps moyen avant défaillance (MTTF). Des analyses statistiques ont été effectuées en utilisant la distribution de Weibull puis en associant les paramètres trouvés au modèle d'Arrhenius pour déterminer l'énergie d'activation liée aux défaillances produites dans des conditions contrôlées. Il a été démontré par le temps de défaillance (TTF) des échantillons soumis à des tests de stress combinés que le groupe A semble être le plus fiable suivi par le groupe B et au moins le groupe C, qui s'est avéré le plus affecté. Des tests combinés à différents niveaux de contraintes thermiques et électriques ont été effectués dans le but de déterminer si la défaillance des échantillons évolue à des niveaux plus élevés. Il a été démontré qu'à des températures plus élevées, la durée de vie attendue des condensateurs est diminuée et qu'une valeur de tension plus élevée produit également cet effet. Pour les groupes A et B, les défaillances semblent liées au même mécanisme dans une plage de températures de 100 à 200 ° C lorsqu'elles sont testées à 400 et 600 V. Le groupe C présente ce comportement mais dans une fourchette beaucoup plus basse de 20 à 90 ° C. La valeur de l'énergie d'activation (Ea)a été déterminée pour chaque condition d'essai. A 400 V, le groupe A a la valeur la plus faible de Ea (1,06 ± 0,08 eV). le stress a un effet plus faible sur ce groupe que le groupe B (Ea = 1,25 ± 0,05 eV) et le groupe C (Ea = 1,45 ± 0,06 eV). Par conséquent, lorsque la contrainte électrique est de 400 V, le groupe C devrait avoir la durée de vie qui changera plus rapidement si la température évolue. En revanche, lorsqu'une tension plus élevée a été appliquée (600 V), même si les TTF observés étaient inférieurs à ceux obtenus à 400 V, l'énergie d'activation déterminée n'était pas significativement différente pour les trois groupes. Cependant, les valeurs étaient inférieures à celles des tests à 400 V dans le groupe B (Ea = 1,09 ± 0,02 eV) et dans le groupe C (Ea = 1,08 ± 0,02 eV). Le groupe A possède une énergie d'activation similaire malgré le stress électrique plus élevé (Ea = 1,01 ± 0,09 eV), ce qui peut encore une fois être une indication de sa plus grande stabilité par rapport aux deux autres groupes. Même si les mécanismes de défaillance n'ont pas été déterminés, avec les valeurs déterminées pour l'énergie d'activation qui leur est associée, il est possible de dire qu'étant au-dessus des trois groupes d'échantillons, cela pourrait impliquer que malgré leurs différences de composition et leur sont affectés par les valeurs élevées de stress, c'est le même mécanisme qui conduit à leur dégradation.
Cette partie du travail a pu être réalisée grâce à un dispositif entièrement développé par le laboratoire LAPLACE et pouvant être utilisé pour effectuer des tests de vie accélérés sur des MLCC de manière précise afin d'obtenir des informations sur sa durée de vie prévue. De plus, sachant que les principales différences entre ces groupes de condensateurs sont la composition du matériau diélectrique, à savoir la quantité d'additifs et de dopants, ces résultats ont fourni des informations confirmant que les échantillons auront des propriétés différentes en fonction de la composition de la formulation de céramique diélectrique.
L'étape suivante de l'étude a consisté à évaluer la possibilité de formation de phases secondaires due à la présence de Y_2O_3 en tant que dopant. Comme ce n'est pas le seul dopant trouvé dans la formulation diélectrique MLCC, le rôle de Y_2O_3 en tant que dopant a été évalué dans des poudres BT pure et deux poudres BT formulées industriellement dans le but d'étudier les interactions possibles entre les différents dopants. Des poudres et des

céramiques ayant différentes concentrations de Y_2O_3 ont été préparées et ont ensuite été traitées thermiquement ou frittéesLe traitement thermique des poudres a été effectué sous air, tandis que le frittage des céramiques a été effectué à la fois sous air et sous atmosphère réductrice. Il a été démontré que la structure de $BaTiO_3$ peut être affectée par la présence de Y^{3+} dans les poudres ou les céramiques, étant plus visible lorsque le niveau de dopage Y^{3+} augmente. En outre, dans certaines conditions, la formation de phases secondaires a été favorisée : $Ba_6Ti_{17}O_{40}$, Y_2TiO_5 et $Y_2Ti_2O_7$. Ces résultats illustrent l'influence de Y^{3+} en tant que dopant dans $BaTiO_3$. De plus, les résultats montrent clairement que les interactions entre les additifs utilisés dans une formulation commerciale sont très importantes et jouent également un rôle dans les propriétés finales et la formation des phases secondaires.
Ce travail démontre que les formulations à base de BT pour les applications diélectriques sont très sensibles à des modifications, même infimes, de leurs compositions, ce qui peut entraîner des modifications importantes des propriétés finales du matériau et leur fiabilité. D'autres perspectives peuvent être envisagées pour étudier plus précisément le rôle réel des autres additifs et dopants et, en particulier, les interactions qu'ils peuvent avoir dans des systèmes réels dans les conditions de leurs différentes applications.

Références

Acosta, M., Zang, J., Jo, W., & Rödel, J. (2012). *Journal of the European Ceramic Society, 32*(16), 4327-4334.
Albertsen, K., Hennings, D., & Steigelmann, O. (1998). *Journal of electroceramics, 2*(3), 193-198.
Ashburn, T., & Skamser, D. (2008, January). In *Proceedings of the 5th SMTA Medical Electronics Symposium*. California, USA.
Armstrong, T. R., & Buchanan, R. C. (1990). *Journal of the American Ceramic Society, 73*(5), 1268-1273.
Barsoum, M., & Barsoum, M. W. (2002). Fundamentals of ceramics. CRC press.
Belous, A., V'yunov, O., Kovalenko, L., & Makovec, D. (2005). *Journal of Solid State Chemistry*, 178(5), 1367-1375.
Belous, A., V'yunov, O., Glinchuk, M., Laguta, V., & Makovez, D. (2008). *Journal of materials science, 43*(9), 3320-3326.
Buscaglia, M. T., Viviani, M., Buscaglia, V., Bottino, C., & Nanni, P. (2002). *Journal of the American Ceramic Society*, 85(6), 1569-1575.
N. H. Chan, R. K. Sharma, and D. M. Smyth *J. Am. Ceram. Soc.*, vol. 64, no. 9, pp. 556–562, Sep. 1981.
H. Chazono and H. Kishi, *Jpn. J. Appl. Phys.*, vol. 40, no. 9, pp. 5624–5629, Sep. 2001.
Cheng, H. F. (1989).. *Journal of Applied Physics*, 66(3), 1382-1387.
Fang, T. T., & Shuei, J. T. (1999). *Journal of materials research, 14*(5), 1910-1915.
Fantozzi, G., Niepce, J. C., & Bonnefont, G. (2013). *Les céramiques industrielles: Propriétés, mise en forme et applications*. Dunod.
Felgner, K. H., Müller, T., Langhammer, H. T., & Abicht, H. P. (2001). *Journal of the European Ceramic Society, 21*(10), 1657-1660.
Fu, Q. X., Mi, S. B., Wessel, E., & Tietz, F. (2008).. *Journal of the European Ceramic Society, 28*(4), 811-820.
Grogger, W., Hofer, F., Warbichler, P., Feltz, A., & Ottlinger, M. (1998).. *Physica status solidi (a), 166*(1), 315-325.
Gong, H., Wang, X., Zhang, S., & Li, L. (2016). *Materials Research Bulletin, 73*, 233-239.
Guha, J. P. and Kolar, D.,. In *5th Conference on Ceramics for Electronics*, Liblice, 1974, pp. 1–9.
Hagenbeck, R., & Waser, R. (1998). *Journal of applied physics, 83*(4), 2083-2092.
Han, Y. H., Appleby, J. B., & Smyth, D. M. (1987). *Journal of the American Ceramic Society, 70*(2), 96-100.
He, F., Ren, W., Liang, G., Shi, P., Wu, X., & Chen, X. (2013).. *Ceramics International, 39*, S481-S485.
Hennings, D., & Rosenstein, G. (1984). *Journal of the American Ceramic Society, 67*(4), 249-254.
Hernández Lara, J. P., Pérez Labra, M., Barrientos Hernández, F. R., Romero Serrano, J. A., Ávila Dávila, E. O., Thangarasu, P., & Hernández Ramirez, A. (2017).. *Materials Research, 20*(2), 538-542.
Huang, X., Liu, H., Hao, H., Zhang, S., Sun, Y., Zhang, W. & Cao, M. (2015). *Ceramics International 41*(6), 7489-7495.

Jain, T. A., Fung, K. Z., Hsiao, S., & Chan, J. (2010). *Journal of the European Ceramic Society*, 30(6), 1469-1476.
Jeong, J., Lee, E. J., & Han, Y. H. (2005).. *Japanese journal of applied physics*, 44(6R), 4047.
Kahn, M. (1981). Multilayer Ceramic Capacitors-Materials and Manufacture. *AVX Technical Information Series*.
Kim, C. H., Park, K. J., Yoon, Y. J., Hong, M. H., Hong, J. O., & Hur, K. H. (2008). *Journal of the European Ceramic Society, 28*(6), 1213-1219.
Kishi, H., Mizuno, Y., & Chazono, H. (2003).. *Japanese Journal of Applied Physics, 42*(1R), 1.
Kuo, D. H., Wang, C. H., & Tsai, W. P. (2006). *Ceramics international, 32*(1), 1-5.
Lee, W. H., Tseng, T. Y., & Hennings, D. (2001). *Journal of Materials Science: Materials in Electronics, 12*(2), 123-130.
Li, B., Zhang, S., Zhou, X., Chen, Z., & Wang, S. (2007). *Journal of materials science,* 42(13), 5223-5228.
Li, W., Xu, Z., Chu, R., Fu, P., & Hao, J. (2009). *Journal of Alloys and Compounds, 482*(1), 137-140.
Liu, G., & Roseman, R. D. (1999). *Journal of Materials science, 34*(18), 4439-4445.
Liu, D. D., & Sampson, M. J. (2012). Liu, D. D. (2015). IEEE Transactions on Components, *Packaging and Manufacturing Technology*, 5(1), 40-48.
Luo, Y., Pu, Y., Zhang, P., Zhao, J., Wu, Y., & Liu, Y. (2016).. *Ferroelectrics, 492*(1), 10-16.
Makovec, D., Samardžija, Z., & Drofenik, M. (2004). *Journal of the American Ceramic Society, 87*(7), 1324-1329.
Futureelectronics.com. (n.d.). Multilayer ceramic capacitor, high voltage ceramic capacitors - Future Electronics. [online] Retrieved from: http://www.futureelectronics.com/en/capacitors/multilayer-ceramic-capacitor.aspx [Accessed 8 Nov. 2017].
N. Nikulin, Fundamentals of electrical materials, Mir Publishers, Moscow, (1988).
Nicker, D. A. (1974). *Active and Passive Electronic Components, 1*(2), 113-120.
T. Nomura, N. Kawano et al. Japanese Journal of Applied Physics Part 1-Regular Papers Brief Communications & Review Papers, 1995, vol. 34, pp. 5389–5395.
Okino, Y., Shizuno, H., Kusumi, S., & Kishi, H. (1994). *Japanese journal of applied physics, 33*(9S), 5393.
Ösküz, K. E., Torman, M., Sen, S., & Sen, U. (2016). *Materials, Methods & Technologies, 10*, 361-366.
Pan, M. J., & Randall, C. A. (2010). *IEEE electrical insulation magazine, 26*(3).
Paredes-Olguín, M., Lira-Hernández, I. A., Gomez-Yañez, C., & Espino-Cortes, F. P. (2013). *Physica B: Condensed Matter,* 410, 157-161.
Park, K. J., Kim, C. H., Yoon, Y. J., Song, S. M., Kim, Y. T., & Hur, K. H. (2009). *Journal of the European Ceramic Society, 29*(9), 1735-1741.
Paunovic, V., Mitic, V., Marjanovic, M., & Kocic, L. (2016). *Facta Universitatis, Series: Electronics and Energetics, 29*(2), 285-296.
Petrović, M. V., Bobić, J. D., Ramoška, T., Banys, J., & Stojanović, B. D. (2011). *Materials characterization, 62*(10), 1000-1006.
B. S. Rawal and N. H. CHAN, "Conduction and failure mechanisms in barium titanate based ceramics under highly accelerated conditions," pp. 184–188, 1984.
Richerson, D. W. (2005). Modern ceramic engineering: properties, processing, and use in design. CRC press.
Shimada, Y., Utsumi, K., Yonezawa, M. & Takamizawa, H. (1981). *Japanese Journal of Applied Physics*, 20(S4), 143.
Standard, E.I.A. (2002). Ceramic dielectric capacitors classes I, II, III and IV–part I: characteristics and requirements. EIA-198-1-F, November.
Tien, T. Y., & Carlson, W. G. (1963). *Journal of the American Ceramic Society, 46*(6), 297-298.
Tsur, Y., Hitomi, A., Scrymgeour, I. & Randall, C. A. (2001a). *Japanese Journal of Applied Physics, 40*(1R), 255.
Tsur, Y., Dunbar, T. D., & Randall, C. A. (2001b). *Journal of Electroceramics, 7*(1), 25-34.
Urek, S., Drofenik, M., & Makovec, D. (2000). *Journal of materials science, 35*(4), 895-901.
Valdez-Nava, Z., Tenailleau, C., Guillemet-Fritsch, S., El Horr, N., Lebey, T., Dufour, P. & Chane-Ching, J. Y. (2011). *Journal of Physics and Chemistry of solids, 72*(1), 17-23.
Völtzke, D., Abicht, H. P., Pippel, E. & Woltersdorf, J. *Journal of the European Ceramic Society, 20*(11), 1663-1669.
V'yunov, O. I., Kovalenko, L. L., Belous, A. G., & Belyakov, V. N. (2005). *Inorganic materials*, 41(1), 87-93.
Wang, J., Rong, G., Hao, L., Gao, L., Cheng, H., Li, J., & Duan, R. (2016). *Modern Physics Letters B, 30*(29), 1650363.
Wang, M. J., Yang, H., Zhang, Q. L., Hu, L., Yu, D., Lin, Z. S., & Zhang, Z. S. (2014). *Journal of Materials Science: Materials in Electronics, 25*(7), 2905-2912.
Wang, T., Wang, X. H., Wen, H., & Li, L. T. (2009). *International Journal of Minerals, Metallurgy and Materials, 16*(3), 345-348.
Wang, X. H., Chen, R., Gui, Z., & Li, L. (2001). *Ferroelectrics, 262*(1), 251-256.

Wu, Y. C., Wang, S. F., McCauley, D. E., Chu, M. S., & Lu, H. Y. (2007). *Journal of the American Ceramic Society, 90*(9), 2926-2934.
Yan, Y., Liu, L., Ning, C., Yang, Y., Xia, C., Zou, Y., ... & Liu, G. (2016). *Materials Letters, 165*, 135-138.
Yoon, S. H., Park, Y. S., Hong, J. O., & Sinn, D. S. (2007). *Journal of Materials Research*, *22*(9), 2539-2543.
Yoon, S. H., Kang, S. H., Kwon, S. H., & Hur, K. H. (2010). *Journal of Materials Research*, *25*(11), 2135-2142.
J.-R. Yoon, K.-M. Lee, and S.-W. Lee, *Transactions on Electrical and Electronic Materials*, vol. 10101, no. 5, pp. 1229–7607, Feb. 2009.
Zhang, J., Hou, Y., Zheng, M., Jia, W., Zhu, M., & Yan, H. (2016). *Journal of the American Ceramic Society*, 99(4), 1375-1382.
Zhi, J., Chen, A., Zhi, Y., Vilarinho, P. M., & Baptista, J. L. (1999). *Journal of the American Ceramic Society*, 82(5), 1345-1348.
Zhu, X. N., Zhang, W., & Chen, X. M. (2013). *Aip Advances, 3*(8), 082125.